

**DEVELOPMENT AND OPTIMIZATION OF A WIDE BASE FEA TRUCK TIRE
MODEL FOR PREDICTION OF TIRE-ROAD INTERACTIONS**

by

Adam Cameron Reid

A Thesis Submitted in Partial Fulfillment
Of the Requirements for the Degree of

Master of Applied Science

In

The Faculty of Engineering and Applied Science

University of Ontario Institute of Technology

April 2015

© 2015 Adam C. Reid

ABSTRACT

The most important aspect of any land-type vehicle is the efficiency in which it can translate energy from an engine, motor, or external source to the ground in an effort to move. Currently, the most efficient way to do so is through the use of pneumatic tires, which are the only link between the chassis and the ground interface. With recent advancements in the computational efficiency of modern computers, there has been a dynamic movement towards virtual modeling and experimentation of pneumatic tires. This thesis provides a detailed analysis of the selection, construction, validation, and possible applications for a Finite Element Analysis (FEA) based tire model. Through the use of an Adaptive Response Surface Method (ARSM) optimization algorithm, the newly constructed wide base FEA truck tire model underwent a parameter-tuning procedure of its materials until the behaviour of the virtual model closely matched the behaviour of the physical tire. The optimized tire model achieved a minimum of 1.78% error in the amount of rolling resistance force measured during steady-state driving conditions between the physical and simulated experiments. In addition, the static vertical deflection of the virtual tire model was able to be minimized to only 0.42% error in comparison to the physical tire. After the optimization process was completed, the FEA wide base truck tire model was used in virtual isolation experiments to populate an analytical in-plane and out-of-plane rigid ring model for use on rigid surfaces. This process has been completed in an effort to aid in the study, understanding and experimentation related to pneumatic tire dynamics.

TABLE OF CONTENTS

ABSTRACT	II
TABLE OF CONTENTS	III
LIST OF FIGURES	VI
LIST OF TABLES	IX
NOMENCLATURE	XI
ACKNOWLEDGEMENTS	XIII
CHAPTER 1: INTRODUCTION AND LITERATURE REVIEW	1
1.1 MOTIVATION.....	1
1.2 OBJECTIVES AND SCOPE.....	2
1.3 OUTLINE OF THESIS.....	5
1.4 LITERATURE REVIEW.....	6
1.4.1 <i>The Pneumatic Tire</i>	6
1.4.2 <i>Tire Dynamics</i>	10
1.4.3 <i>Longitudinal Force Generation</i>	13
1.4.4 <i>Cornering Force Generation</i>	14
1.4.5 <i>Analytical Tire Modeling</i>	15
1.4.6 <i>FEA Tire Modeling</i>	21
1.4.7 <i>Advanced Optimization Techniques</i>	25
1.4.8 <i>Evolutionary Algorithms (EA)</i>	26
1.4.9 <i>Monte Carlo Methods</i>	26
1.4.10 <i>Adaptive Response Surface Methodology (ARSM) Algorithms</i>	27

1.4.11	Parameter-Tuning.....	27
CHAPTER 2:	FEA TIRE CONSTRUCTION.....	29
2.1	MODELING PROGRAMS.....	29
2.2	DIFFICULTIES AND LIMITATIONS	30
2.3	AVAILABLE DATA FOR CONSTRUCTION.....	31
2.4	PROGRESSION TO CONSTRUCTED FEA MODEL	32
CHAPTER 3:	COLLECTION OF EXPERIMENTAL DATA.....	38
3.1	EXPERIMENT GOALS	38
3.2	EXPERIMENTAL SETUP	39
3.3	DATA ACQUISITION	40
3.4	TEST TRACK RESULTS.....	44
3.5	SAND BOX RESULTS.....	47
3.6	CONCLUSION FROM EXPERIMENTS.....	50
CHAPTER 4:	TIRE VALIDATION AND PARAMETER-TUNING	
	OPTIMIZATION METHODOLOGY.....	51
4.1	AVAILABLE DATA FOR PARAMETER-TUNING.....	51
4.2	SELECTION OF OPTIMIZATION ALGORITHM.....	52
4.3	COMBINED EXPERIMENTS PARAMETER-TUNING PROCEDURE.....	56
4.4	RESULTS OF PARAMETER-TUNING OPTIMIZATION	60
CHAPTER 5:	POPULATION OF THE IN-PLANE RIGID RING TIRE	
	MODEL PARAMETERS	63
5.1	DESIRED IN-PLANE RIGID RING PARAMETERS	63
5.2	STATIC FOOTPRINT LENGTH AND WIDTH (A, W)	64

5.3	TOTAL STATIC VERTICAL STIFFNESS (K_{SV}).....	67
5.4	TOTAL DYNAMIC VERTICAL STIFFNESS (K_{DV})	69
5.5	TOTAL VERTICAL DAMPING CONSTANT (C_{TOT})	74
5.6	ROTATIONAL STIFFNESS AND DAMPING CONSTANT OF THE SIDEWALL ($K_{B\theta}$, $C_{B\theta}$).....	77
5.7	LONGITUDINAL TREAD AND TIRE STIFFNESS (K_{CX} , K_K).....	81
CHAPTER 6: POPULATION OF THE OUT-OF-PLANE RIGID		
RING MODEL PARAMETERS.....84		
6.1	DESIRED OUT-OF-PLANE RIGID RING PARAMETERS	84
6.2	TRANSLATIONAL STIFFNESS AND DAMPING CONSTANT OF THE SIDEWALL (K_{BY} , C_{BY}).....	85
6.3	ROTATIONAL STIFFNESS AND DAMPING CONSTANT OF THE SIDEWALL (K_{BY} , C_{BY}).....	88
6.4	LATERAL TIRE STIFFNESS AND DAMPING CONSTANT (K_L , C_L)	92
6.5	CORNERING STIFFNESS (K_F).....	95
6.6	RELAXATION LENGTH (Σ).....	98
6.7	SELF-ALIGNING TORQUE STIFFNESS (K_M).....	99
CHAPTER 7: CONCLUSIONS AND FUTURE WORK.....101		
7.1	GENERAL CONCLUSIONS	101
7.2	CONSIDERATIONS FOR FUTURE WORK	103
REFERENCES.....106		

LIST OF FIGURES

Figure 1-1 A FEA Dual Tire Model (Left) and a FEA Wide Base Tire Model (Right) [3]	3
Figure 1-2 Anatomy of a Radial Bridgestone Aircraft Pneumatic Tire [35]	7
Figure 1-3 Comparison of Bias-Ply (Left) and Radial-Ply Pneumatic Tires (Right) [4]....	9
Figure 1-4 SAE Tire Axis, Forces and Moments [4].....	11
Figure 1-5 General Relationship of Tractive Force and Longitudinal Slip Percentage [4]	13
Figure 1-6 Behavior of a Tire Subjected to a Cornering Maneuver (Top View Shown Left and Front View Shown Right) [4].....	14
Figure 1-7 General Relationship of Cornering Force and Slip Angle [4].....	15
Figure 1-8 The Single Point Contact Model [11]	17
Figure 1-9 The Flexible Ring Tire Model [12]	18
Figure 1-10 The In-Plane Rigid Ring Tire Model [14].....	19
Figure 1-11 The Out-of-Plane Rigid Ring Model [9].....	20
Figure 1-12 The Two Dimensional FEA Tire Model [13].....	23
Figure 1-13 The Three-Dimensional Membrane Tire Model [15]	24
Figure 1-14 The Three-Dimension Full FEA Tire Model [16].....	25
Figure 1-15 A Black Box Optimization Scenario for an Objective Function.....	28
Figure 2-1 Footprint Negative for the Michelin XONE XDA.....	32
Figure 2-2 Initial Planning of the Tire Tread FEA Framework.....	33
Figure 2-3 2D Construction (Left) and 3D Construction (Right) of the Tire Tread.....	34
Figure 2-4 Schematic of a Three-Layered Membrane Element [34]	35
Figure 2-5 Completed XONE XDA Section-Cut Model	36

Figure 2-6 Visual Comparison of the Physical Michelin XONE XDA to the FEA UOIT XONE XDA.....	37
Figure 3-1 Wheel Force Transducer (Right) [20] Mounted Onto the Volvo Truck Tractor (Left)	39
Figure 3-2 Instrumented Truck Tractor Driving Through Soft Soil Ditch	41
Figure 3-3 Volvo Tractor Trailer During Rolling Resistance Experiment	41
Figure 3-4 Volvo Truck Tractor (Without Trailer) Experiencing Vertical Excitation	44
Figure 3-5 Rolling Resistance Results (RRC_1) for Left and Right Tires.....	46
Figure 3-6 Rolling Resistance Results (RRC_2) for Left and Right Tires.....	47
Figure 3-7 Rolling Resistance Results from Sandbox Experiments for Front and Pusher Axle.....	50
Figure 4-1 Visual From the Pressure-Sinkage Simulation	53
Figure 4-2 Progression of Competing Algorithms.....	56
Figure 4-3 Visual of the Total Static Vertical Stiffness and Lateral Stiffness Simulations	58
Figure 4-4 Visual for the Determination of Rolling Resistance Force of the Tire Model	59
Figure 4-5 ARSM Parameter-Tuning Procedure	60
Figure 4-6 Results from Combined Parameter-Tuning Algorithm	61
Figure 5-1 Typical Footprint Shapes of Various Types of Pneumatic Tires [9].....	64
Figure 5-2 Footprint Dimensions Recorded at a Vertical Load of 4625 kg and Inflation Pressure of 120 PSI.....	66
Figure 5-3 Visual from the Total Vertical Stiffness Simulation, Shown Fully Depressed from a Load of 60 kN.....	67
Figure 5-4 Results from the Total Vertical Stiffness (k_{sv}) Simulation	68

Figure 5-5 Visual from the Total Dynamic Vertical Stiffness (k_{dv}) Simulation.....	70
Figure 5-6 Results from the Total Dynamic Vertical Stiffness (k_{dv}) Simulation.....	71
Figure 5-7 Visual of the Total Vertical Damping Constant (C_{tot}) Simulation	74
Figure 5-8 Results from the Total Vertical Damping Constant (C_{tot}) Simulation	75
Figure 5-9 Visual of the Rotational Stiffness and Damping Constant of the Sidewall Simulation ($k_{b\theta}$, $C_{b\theta}$).....	77
Figure 5-10 Results from the Rotational Stiffness and Damping ($k_{b\theta}$, $C_{b\theta}$) Simulation...	78
Figure 5-11 Visual of the Longitudinal Tread and Tire Stiffness (k_{cx} , k_k) Simulation	81
Figure 5-12 Results from the Longitudinal Tire and Tread Stiffness (k_k , k_{cx}) Simulation	82
Figure 6-1 Visual for the Translational Stiffness and Damping Constant of the Sidewall (k_{by} , C_{by}).....	85
Figure 6-2 Results from the Translational Stiffness and Damping (k_{by} , C_{by}) Simulation .	86
Figure 6-3 Visual of the Rotational Stiffness and Damping Constant of the Sidewall (k_{by} , C_{by}) Simulation	89
Figure 6-4 Results from the Rotational Stiffness and Damping (k_{by} , C_{by}) Simulation	90
Figure 6-5 Visual of the Lateral Tire Stiffness and Damping (k_l , C_l) Simulation.....	92
Figure 6-6 Results from the Lateral Tire Stiffness and Damping Constant (k_l , C_l) Simulation.....	93
Figure 6-7 Visual of a Cornering Stiffness (k_f) Simulation, Shown at an Induced Slip Angle of 10 Degrees	96
Figure 6-8 Results from the Cornering Stiffness (k_f) Simulation	97
Figure 6-9 Results from the Self-Aligning Torque Stiffness (k_m) Calculations	100

LIST OF TABLES

Table 2-1 Available Data for Michelin XONE XDA Construction.....	31
Table 3-1 Available Channel Data from Instrumentation.....	42
Table 3-2 Configuration 1: Bobtail (1160.95 lbs, 120 PSI).....	45
Table 3-3 Configuration 2: Trailer 1 (2819.09 lbs, 120 PSI).....	45
Table 3-4 Configuration 3: Trailer 2 (8734.51 lbs, 120 PSI).....	45
Table 3-5 Configuration 4: Trailer 3 (9342.23 lbs, 120 PSI).....	45
Table 3-6 Configuration 5: Trailer 2 (8734.51 lbs, 80 PSI).....	46
Table 3-7 Configuration 1: Bobtail (1160.95 lbs, 120 PSI).....	48
Table 3-8 Configuration 2: Trailer 1 (2819.09 lbs, 120 PSI).....	48
Table 3-9 Configuration 3: Trailer 2 (8734.51 lbs, 120 PSI).....	48
Table 3-10 Configuration 4: Trailer 3 (9342.23 lbs, 120 PSI).....	49
Table 3-11 Configuration 5: Trailer 2 (8734.51 lbs, 80 PSI).....	49
Table 4-1 Available Data for Parameter-Tuning Optimization	52
Table 4-2 Bekker Equation Parameters	54
Table 4-3 Results from the Pressure-Sinkage Algorithm Competition	55
Table 4-4 Optimum Results from ARSM Algorithm	62
Table 5-1 Required In-Plane Rigid Ring Parameters	64
Table 5-2 Measurements of the Michelin XONE XDA Under Rated Load and Inflation Pressure	65
Table 5-3 Results from Static Footprint Simulations	66
Table 5-4 Calculated Parameters for the Total Static Vertical Stiffness (k_{sv})	69
Table 5-5 Calculated Parameters for the Total Dynamic Vertical Stiffness.....	73

Table 5-6	Calculated Parameters for the Total Vertical Damping Constant (C_{tot})	76
Table 5-7	Calculated Parameters for the Rotational Stiffness and Damping Constant ($k_{b\theta}$, $C_{b\theta}$)	80
Table 5-8	Calculated Parameters for the Longitudinal Tire and Tread Stiffness (k_k , k_{cx})	83
Table 6-1	Required Out-of-Plane Rigid Ring Parameters	84
Table 6-2	Calculated Parameters of the Translational Stiffness and Damping Constant of the Sidewall (k_{by} , C_{by})	88
Table 6-3	Calculated Parameters for the Rotational Stiffness and Damping Constant of the Sidewall (k_{by} , C_{by})	91
Table 6-4	Calculated Parameters for the Lateral Tire Stiffness and Damping Constant (k_l , C_l)	95
Table 6-5	Calculated Parameters for Cornering Stiffness (k_f)	98
Table 6-6	Calculated Parameters for the Relaxation Length (σ)	99
Table 6-7	Calculated Parameters for the Self-Aligning Torque Stiffness (k_m)	100

NOMENCLATURE

Symbol	Parameter	Units
In-Plane Parameters		
k_{sv}	Total static vertical stiffness	kN/m
k_{dv}	Vertical stiffness	kN/m
k_{vr}	Residual vertical stiffness	kN/m
C_{bz}	Vertical damping constant	kN-s/m
C_{tot}	Total damping constant	kN-s/m
C_{vr}	Residual damping constant	kN-s/m
$k_{b\theta}$	Rotational stiffness	kN-m/rad
$C_{b\theta}$	Rotational damping constant	kN-m-s/rad
k_k	Longitudinal tire stiffness	kN/slip
k_{cx}	Longitudinal tread stiffness	kN/m
Out-of-Plane Parameters		
k_{by}	Translational stiffness	kN/m
C_{by}	Translational damping constant	kN-s/m
$k_{b\gamma}$	Rotational stiffness	kN-m
$C_{b\gamma}$	Rotational damping constant	m-s/rad
k_l	Lateral tire stiffness	kN/m
C_l	Lateral damping constant	s/m
k_f	Cornering stiffness	kN/rad
σ	Relaxation length	m
Additional Variables		
ω	Natural frequency of vibration	rad/s
ω_n	Undamped rotational natural frequency	rad/s
ω_d	Damped rotational natural frequency	rad/s
m_b	Mass of the tire belt	kg
m_{wheel}	Mass of the tire and rim	
m_{tot}	Total mass of the tire model	kg
f	First mode frequency of in-plane vibration	Hz
α	Nodal damping coefficient	-

ξ	Critical damping ratio from simulation	-
ξ_{tot}	Total damping ratio	-
δ	Logarithmic decrement	-
y_{ss}	Steady state translational displacement	mm
y_1	First peak translational displacement	mm
y_2	Second peak translational displacement	mm
θ_{ss}	Steady state in-plane angular displacement	rad
θ_1	First peak in-plane angular displacement	rad
θ_2	Second peak in-plane angular displacement	rad
τ_d	Damped period of vibration	s
t_1	Time of first peak	s
t_2	Time of second peak	s
C_c	Critical damping constant	kN-m-s/rad
γ_{ss}	Steady state out-of-plane angular displacement	rad
γ_1	First peak out-of-plane angular displacement	rad
γ_2	Second peak out-of-plane angular displacement	rad
I_{bx}	Moment of inertia of the tire belt	kg-m ²

ACKNOWLEDGEMENTS

The author would like to express his gratitude to the various individuals from Volvo 3P and Volvo Group Trucks Technology for their financial and technical support during the course of this thesis research. In addition, the author would like to express his appreciation to the Vehicle Dynamics and Crash Simulation Laboratory at the University of Ontario Institute of Technology (UOIT) and its supervisor, Dr. Moustafa El-Gindy for the opportunity to be a contributor to a long-standing and prestigious research project.

As a personal side, the author would also like to thank all of his friends and family that have provided support, whether financial or emotional, during the course of this educational journey. From the various challenges that have appeared, it would not have been possible without all of their encouragement and inspiration.

CHAPTER 1: INTRODUCTION AND LITERATURE

REVIEW

This chapter is included in order to introduce the work in this thesis. The thesis research motivation, objectives, general outline and literature review are all contained in this chapter. The information provided within this section is important to the understanding of the methodology and future concepts presented in this thesis.

1.1 MOTIVATION

The lean and competitive nature of the automotive industry has made it imperative that a company constantly improves and innovates in order to stay relevant. Due to the nature of the industry, there will always exist the need for tire manufacturers to improve the design and construction of pneumatic tires for better transmission of energy into motion. If the physical product is unable to be improved, there still exists the ability to improve the process itself to become more efficient in its entirety. In the past, the majority of the research and development process for pneumatic tires has existed in the physical realm, in which the construction and testing had been completed by physical means. Using this primitive technique, the pneumatic tire was able to advance quite significantly from its patented introduction 1888 by Scottish veterinarian John Boyd Dunlop [1].

Recently, there has been a dramatic move towards virtual research and development. This is mainly due to the increased speed in which the various design stages can be completed because of the computational efficiency of modern computers. The overall time it takes for a tire to be constructed and tested has shortened in the virtual environment. The process is

also considerably less expensive, as the time and capital required to run and maintain most physical equipment is quite high. Virtual prototyping is also quite advantageous as it negates the amount of physical prototypes that are required to be constructed and then tested in one-off experiments. Small design iterations related to items such as material properties can be changed quickly in a virtual environment and explored without the hindrance of constructing a new physical tire. This would be an example of a parametric model, which allows for economic model optimization through parameter-tuning techniques [2].

There are multiple methods available for conducting research and experiments outside of the physical realm. Through the understanding of the physical tire, one could construct analytical, empirical, semi-empirical, or virtual tire models for the goal of the prediction of tire-ground interactions. In order to condense the complex nature of the pneumatic tire to another suitable format, there must be a complete understanding of the various tire dynamic principles. The average pneumatic tire is subjected to a multitude of forces. The tire must be constructed in a way such that it can support the vehicle mass and transfer energy from the engine to the road surface, all while experiencing extreme loads, maintaining control, and behaving in a predictable manner. It has been able to do so and meet ever-changing demands by evolving from simple rubber inner tubes to a carefully crafted recipe of synthetic and natural viscoelastic rubbers woven around steel belts in a harmonious and precise manner [3].

1.2 OBJECTIVES AND SCOPE

The underlying purpose of this thesis research was to incorporate new and innovative techniques to the virtual construction, testing, validation and study of a wide base heavy

vehicle pneumatic tire. The wide base tire is a relatively new design that originated to replace the standard dual tire seen on most heavy transportation vehicles. Due to the required spacing between dual tires, the overall design envelope for the standard configuration is much larger than that of a wide base tire. By essentially stretching the contact patch to match the overall area of dual tires, the wide base tire is able to develop the equivalent cornering and tractive properties while using much less design space. In addition, the reduction of sidewalls from four to two allows for a reduction in hysteresis of the pneumatic tire. A reduction in hysteresis consequently results in a reduction of energy lost during operation. A visual comparison of a FEA dual tire model and a wide base tire model can be seen in [Figure 1-1](#).



Figure 1-1 A FEA Dual Tire Model (Left) and a FEA Wide Base Tire Model (Right) [3]

An executive report from the North American Council for Freight Efficiency (NACFE) from December of 2010 stated a summary of the benefits from the implementation of wide

base tire models across a transportation fleet. From their research, the NACFE concluded that due to the lower rolling resistance of the tire, immediate fuel use improvements of 3% to 6% is gained [4]. In addition, there would be fewer tires and wheels to manage when converting from 18 to 10 wheel positions. When combined with single wide aluminum wheels, a weight reduction of 100 lbs. per wheel end can be realized. An increase in brake life can also be found, as more of the brake drum is exposed to open air which allows the drum and shoe to stay cooler and last longer. Lastly, the wide base tire has lower tire set up costs. Due to fewer wheels being purchased per vehicle, wide base tires offer an advantage in total purchase cost than specifying dual tires and wheels [4].

Due to the relatively short existence of these new tire models, automotive manufacturers are currently interested in the physical capabilities and characteristics of this new design configuration. A more thorough understanding of the tire-road interaction properties for wide base tires can be achieved by conducting a wide range of experiments. The planned contribution of this thesis research was to improve the FEA construction process of tire models as well as to better understand the physical parameters of a wide base tire.

For the majority of automotive manufacturers, conducting pure physical testing of a new tire is either impossible due to a lack of testing equipment or inefficient due to concurrent research projects. With considerable progression in the computational efficiency of modern computers, a hybrid approach to research and development is commonly used in which a combination of physical, virtual and analytical tire models are used. This hybrid approach was mimicked in this thesis research in order to conduct this research in the most efficient manner available.

With a general understanding as to the end product and procedure, the goals of this thesis research were loosely determined to be:

- Collect physical measurements from a selected wide base tire model
- Collect physical experimental data from the selected tire model in both static and dynamic experiments
- Recreate the physical tire in a FEA environment
- Recreate the physical experiments in a FEA environment for validation purposes
- Determine multiple methods for parameter-tuning validation
- Conduct rolling resistance prediction experiments
- Conduct steering prediction experiments
- Populate an analytical tire model for supplemental research ability to the FEA tire model

1.3 OUTLINE OF THESIS

The research goals allowed for a linear approach to each topic. For the development of this tire model, few items were required to be concurrently completed which allowed for a non-convoluted schedule. Chapter 2 of this thesis contains information related to the collection of experimental data for the construction of the tire model. The following chapter uses this experimental data to construct the FEA wide base tire model and covers all of the techniques and challenges of doing so. Chapter 4 includes the FEA tire model's validation process using an Adaptive Response Surface Methodology (ARSM) algorithm for black-box parameter-tuning. The subsequent chapters, Chapters 5 and 6, take the tire model and use it to populate an analytical rigid ring tire model. Both the in-plane and out-of-plane

rigid ring parameters are calculated in separate chapters. Chapter 7 discusses the conclusions of the thesis as well as proposals for continuation of this work topic.

1.4 LITERATURE REVIEW

The goal of the corresponding literature review was to gain an understanding as to the current state of tire modeling in academic research, whether analytical, empirical, semi-empirical or virtual based. It includes relevant information related to pneumatic tires, the modeling of tires, tire-road and tire-soil interaction properties. The information provided within this section is vital to the understanding of future concepts that are discussed in this thesis.

1.4.1 The Pneumatic Tire

Before one could attempt to recreate a highly non-linear physical tire as a virtual entity, there should be a thorough understanding of pneumatic tires first. Tire dynamics is a subcomponent of vehicle dynamics and is arguably one of the most important components of a land vehicle. The pneumatic tire has developed significantly since its patented introduction in 1888 by Scottish veterinarian John Boyd Dunlop [1]. The tire must not only support the vehicle mass and transfer energy from the engine to the road surface, but also do so while experiencing extreme loads, maintaining control, and behaving in a predictable manner. In order to achieve all of these tremendous tasks, the construction of these tires has evolved from simple rubber inner tubes to a carefully crafted recipe of synthetic and natural viscoelastic rubbers woven around steel belts in a harmonious and precise

orientation [3]. A cross-section of a radial aircraft tire from Bridgestone can be seen in Figure 1-2.

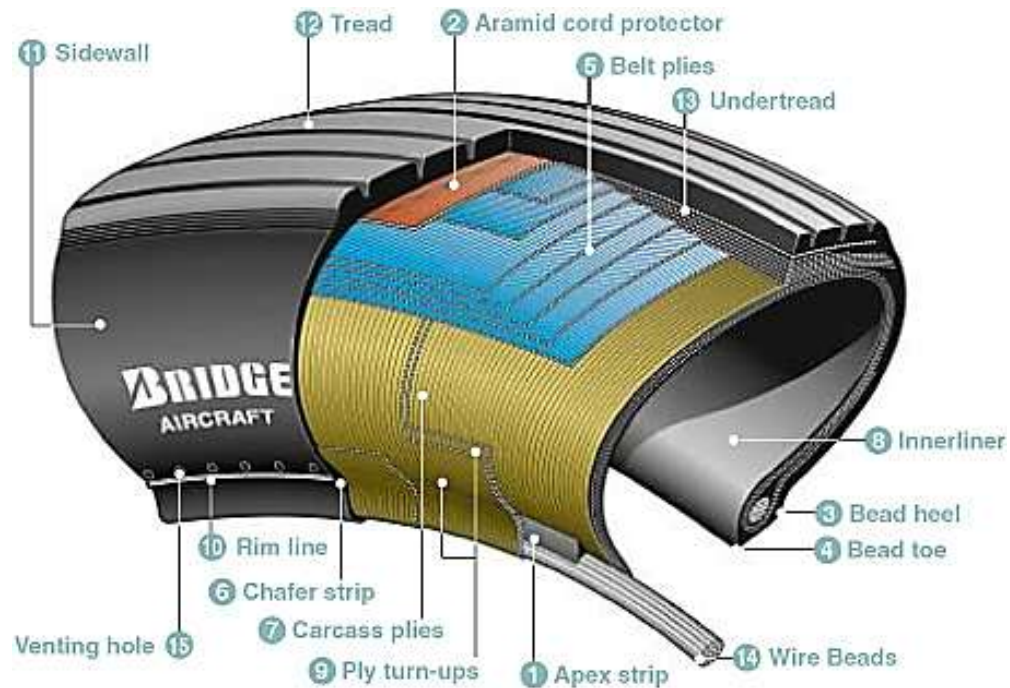


Figure 1-2 Anatomy of a Radial Bridgestone Aircraft Pneumatic Tire [35]

In general, a pneumatic tire can be defined as a flexible toroid with a rigid outer casing that is pressurized with air. The tire most commonly consists of the main carcass, belt plies, undertread, tread, sidewall, and beads. While all components of a pneumatic tire contribute to the performance, the tire carcass is one of the most important elements in the characteristics of that specific tire. A typical tire carcass includes a low-modulus rubber compound filled with high-modulus and flexible cords commonly made of natural, synthetic or metallic fabrics [5]. The carcass plies run from bead to bead and provide the majority of rigidity within the tire. The steel beads are multiple steel cords that run along the bottom of tire, where it contacts the rim. They are constructed from high strength steel cords to provide a seal between the rim and tire when properly inflated.

The carcass is coated on its exterior with a highly flexible and highly durable rubber compound known as the tire sidewall. This is an important protective component, as the coating allows for a protective layer for the carcass plies from cuts and scrapes during operation [6]. It will also add some slight rigidity to the overall tire as well as increase the vibration damping performance.

Moving to the top of the tire, the tread is constructed in a wide variety of designs depending on the specific application. The tread is the only component that truly contacts the road surface, and thus is designed for maximum road adhesion, low rolling resistance, displacing precipitation, or for travel through soft-soils. The geometry of the tread can have a tremendous effect on the performance of the tire. In general, the tread is constructed from a rubber compound designed to provide a high amount of tire-road traction while minimizing the amount of wear that occurs during operation [7].

The next component is the tire belt plies, which are multiple layers of steel cords that run on top of the tire carcass to provide more strength during operation in the transverse and lateral directions. The orientation of these cords plays a crucial role on various performance aspects of the tire. The angle between the tire centerline and the cords defines the tire's crown angle. When the crown angle is high (> 25 degrees), it is common that the tire will have good cornering characteristics but a harsh ride. If the cords are arranged at right angles to the tire centerline to form a 90 degree angle, the tire will generally have the opposite

characteristics and be comfortable but with worse handling performance [5]. A comparison of radial- and bias-ply tires are shown in Figure 1-3.

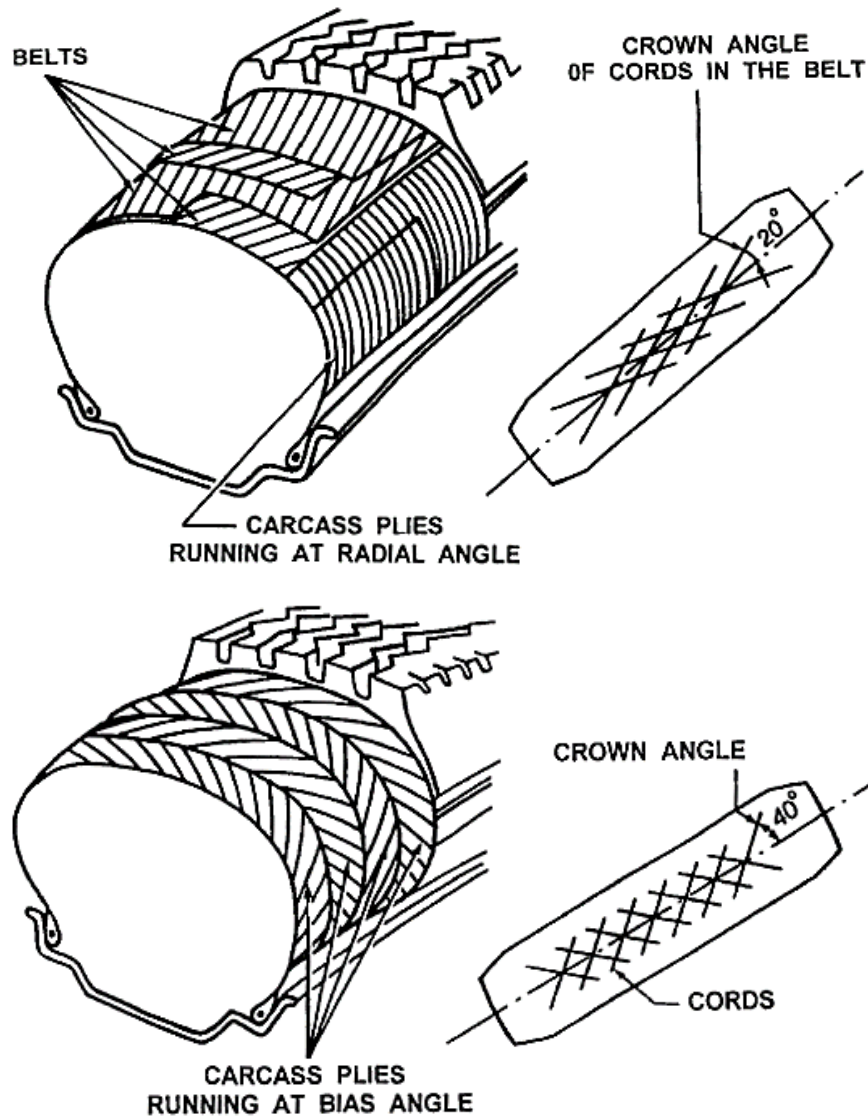


Figure 1-3 Comparison of Bias-Ply (Left) and Radial-Ply Pneumatic Tires (Right) [4]

Radial-ply tires are currently dominant for passenger cars and trucks due to their low rolling resistance and good ride quality. They are also featured more commonly on heavy-duty earth-moving machinery than in recent years, but bias-ply tires are still dominant in cycles, motorcycles, agricultural machinery and some military equipment [5].

The same principles and concepts are also applied to the construction of wide base tires. As seen previously in Figure 1-1, wide base truck tires are implemented to replace the use of dual tires on truck tractor pusher axles. The wide base tire is a relatively new product that was introduced commercially in 2000. By eliminating wasted space, maintaining contact area, and reducing areas for hysteresis, the wide base tire has many benefits when used. These include a reduction in fuel consumption, overall weight savings, improved stability, and reduced downtime from flats [8]. Some manufacturers claim to be able to reduce the overall rolling resistance in one tire by up to 30% when switching from a dual to a wide base tire. By making the switch to wide base tires across an entire fleet, some have experienced up to a 10 percent improvement in fuel efficiency and more than 740 lb. of weight savings per truck [9].

1.4.2 Tire Dynamics

The pneumatic tires, whether radial- or bias-ply, are subjected to multiple forces and moments during the regular operation of a wheeled land vehicle. In order to fully describe and understand these interactions between these forces and the tire, a universal axis was developed to serve as a reference for the definition of various parameters [10]. The Society of Automotive Engineers (SAE) developed such an axis system and it has been adopted by most as a universal template and is shown in Figure 1-4.

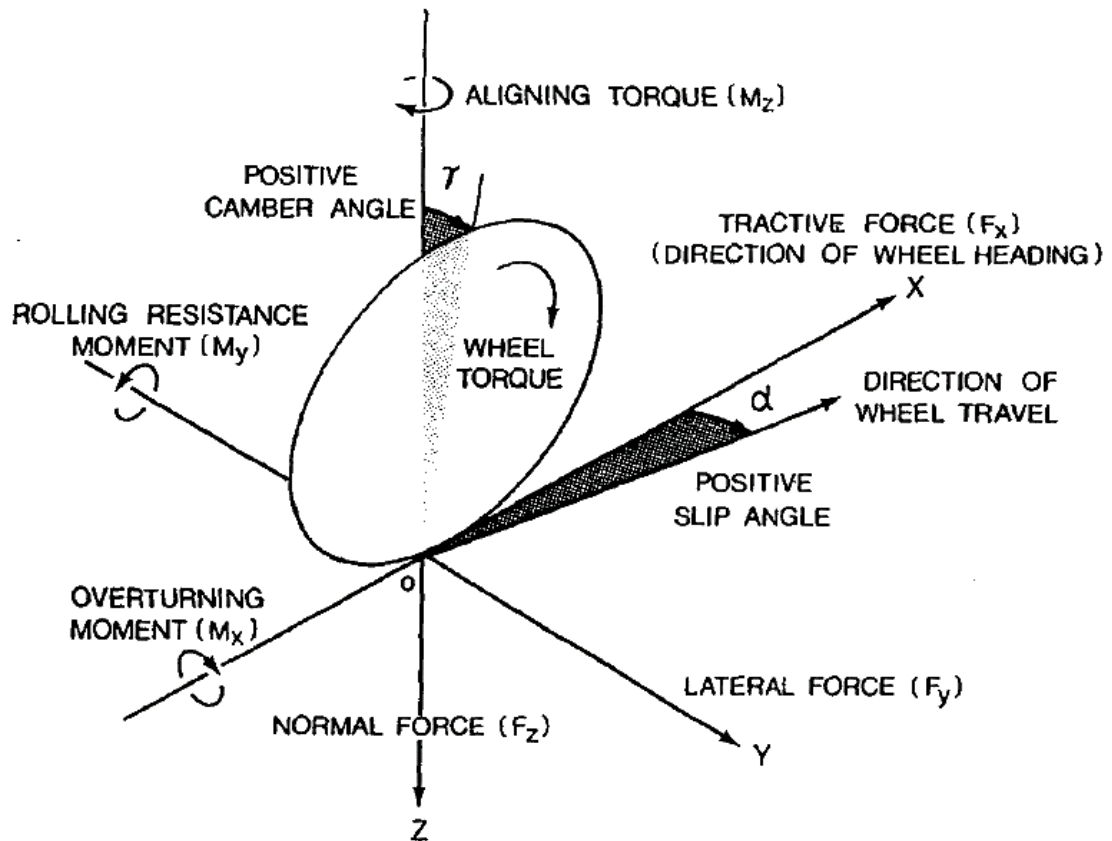


Figure 1-4 SAE Tire Axis, Forces and Moments [4]

With the axis system defined, it is necessary to define the various forces and moments described. Forces that align along the x-axis describe the longitudinal forces (F_x) that interact with the tire. These forces include the tractive force, rolling resistance force, longitudinal friction forces and any other external forces that act along that axis. These longitudinal forces are most commonly generated during braking and acceleration and act in the direction of travel of the vehicle [5].

Lateral forces (F_y) include the cornering forces resulting from steered input, crosswinds, or any external forces such as collision that act along the y-axis. The combination of lateral forces will dictate the amount of control one has over the vehicle during cornering maneuvers.

The normal force (F_z) acts on the tire in the purely vertical direction. This force is developed due to the corresponding vehicle mass and can change drastically from dynamic driving behaviour. Extreme maneuvers such as braking and acceleration can transfer the vehicle mass forward or rearward and effect the tire-road interaction properties of the tire.

The overturning moment (M_x) is the moment that acts about the x-axis due to the camber applied to the tire. With the center of gravity shifting outward, this force displacement causes the tire to try to overturn.

The rolling resistance moment (M_y) is a moment that acts about the y-axis and resists the rolling of the tire in both the positive and negative x-axis. Since the tire is not completely rigid, there is a slight compression of the tread, undertread and carcass at the contact patch. When rolling, the vertical contact pressure is distributed over the contact patch unevenly [10]. With a higher-pressure distribution on the leading edge of the tire, a moment is produced from the resultant forces and the offset of this pressure distribution.

The self-aligning moment (M_z) or self-aligning torque is another moment that is generated during steered conditions and acts opposite to the steering input. During cornering conditions, the cornering force acts slightly behind the wheel center. This distance from the center to the cornering force generation location is known as the pneumatic trail and gives way to this moment acting about the z-axis. If the steering position was released, the self-aligning moment (M_z) would attempt to reduce the steering angle back to a neutral position.

1.4.3 Longitudinal Force Generation

There are also many standard relationships between these forces and environment variables that help to form the foundation of many tire dynamics principles. The first of which incorporates the longitudinal force (F_x) that is developed either during acceleration or braking. During operation, the longitudinal forces that are developed at the contact patch are the only forces that oppose skidding. If the rubber did not slip over the ground, the forces of reaction to strain and of molecular bonding would not be tangential, but purely vertical. Only the onset of slippage can generate forces that oppose skidding [11]. The rate at which longitudinal force is developed is directly related to the slip percentage that is measured between the tire and the road surface. A typical trend of this relationship can be seen in [Figure 1-5](#).

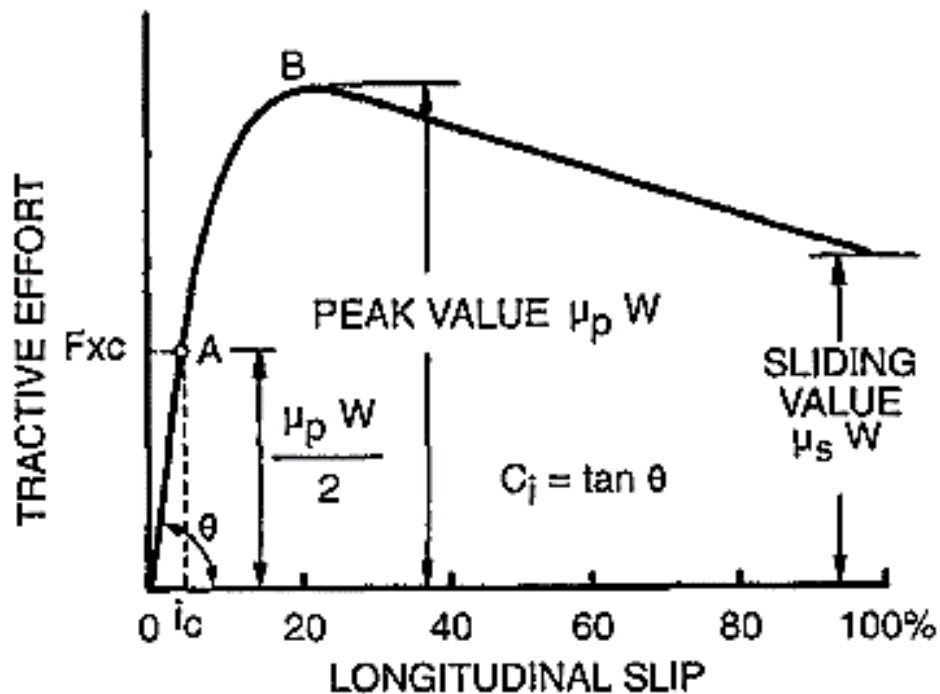


Figure 1-5 General Relationship of Tractive Force and Longitudinal Slip Percentage [4]

The longitudinal force that is generated increases rapidly when the slip percentage ranges between 0 and 20%. Around this location, the longitudinal force will equal the peak value,

which is equal to the peak friction coefficient (μ_p) multiplied by the vehicle load (W). At this point, the longitudinal force will taper off to a sliding value, also found by multiplying the sliding friction coefficient (μ_s) by the vehicle load (W). At this point, the tire is experiencing 100% slip at the tire-road interface and ceases to develop longitudinal force.

1.4.4 Cornering Force Generation

In the lateral plane, there is also a recognized relationship between the amount of cornering force that can be developed and the specified slip angle. During steered maneuvers, the contact patch of the tire model will deflect drastically from its neutral position. The tread will attempt to align with the steered orientation of the tire (A) and a cornering force will be developed slightly behind the wheel center. Due to the uneven pressure distribution within the tire during cornering procedures, the cornering force is developed at the position of the pneumatic trail (t_p). A schematic of a steered tire can be seen in [Figure 1-6](#).

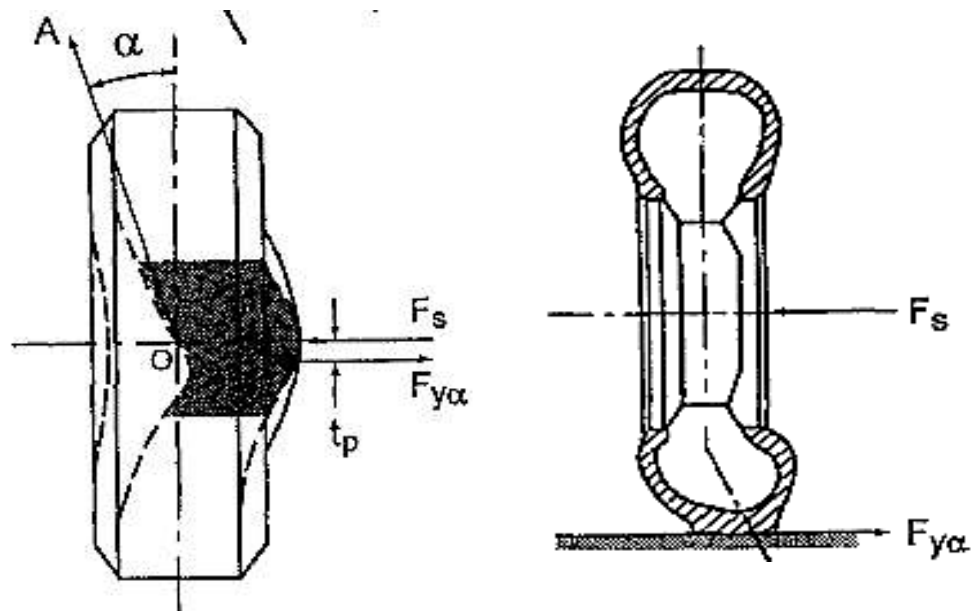


Figure 1-6 Behavior of a Tire Subjected to a Cornering Maneuver (Top View Shown Left and Front View Shown Right) [4]

The difference between the tire tread deflection angle and the tire's forward heading defines the tire's slip angle (α). The variation of the slip angle directly effects the amount of cornering force that can be developed at the contact patch. As the slip angle from induced steering is increased from 0-4 degrees, generally the cornering force increases in a linear rate. Beyond this induced slip angle, the cornering force will continue to increase but no longer in a linear fashion. It will typically taper off towards the road adhesion limit, where the tire begins to slide laterally. For passenger car tires, the maximum cornering force may be achieved at a slip angle around 18 degrees. For race car tires, this value may be achieved as early as a slip angle of 6 degrees [5]. Ideal results from a steered experiment can be seen in Figure 1-7.

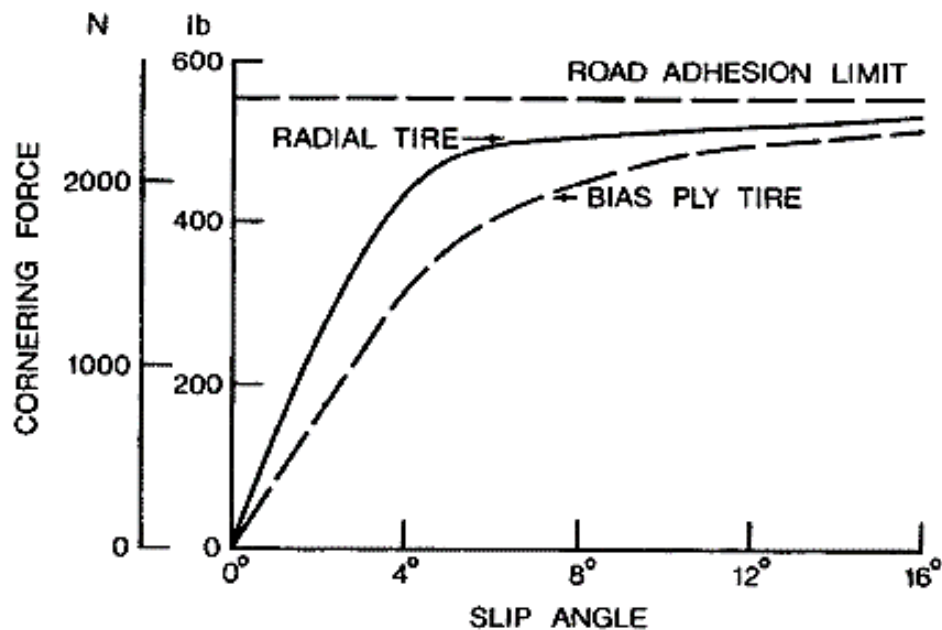


Figure 1-7 General Relationship of Cornering Force and Slip Angle [4]

1.4.5 Analytical Tire Modeling

With a general understanding of the tire dynamics, it would then be possible to represent the tire as a simple mechanical system. These simplified systems, often called analytical

tire models, condense the complex nature of a pneumatic tire to a spring-mass-damper mechanical system. Depending on the configuration of these components, the nature of a pneumatic tire may be able to be predicted by the analysis of its corresponding analytical tire model. The analytical tire model is defined by a set of equations of motion, often dependant on the degrees of freedom allowed within the model. This method of analysis was widely popular before computer aided systems were developed due to the ability to predict the possible performance of a tire model. Even with the improved computational power, many analytical models are still used within items such as real-time controllers for the speed and acceptable accuracy for specific situations.

One example of an analytical tire model is a single point contact mechanism, shown in Figure 1-8. This is arguably the most simplified tire model that can be used for evaluation and was examined by Captain *et al.* in 1979 [12]. The single point follower is a mechanism in which only the vertical behaviour of the tire is considered and all of the stiffness and damping values are ignored except for the values in the purely vertical direction. There are several assumptions that are made, including the contact point never loses contact with the road surface and that the contact point lies directly under the wheel center. This model was initially developed for the purpose of investigating the ride comfort and vertical responses transmitted to the vehicle from irregular road profile inputs. This model behaved remarkably well at low input frequencies (0.1-1 Hz), but tended to overestimate the transmitted tire forces at intermediate to high frequency bands (1-10 and 10-100 Hz).

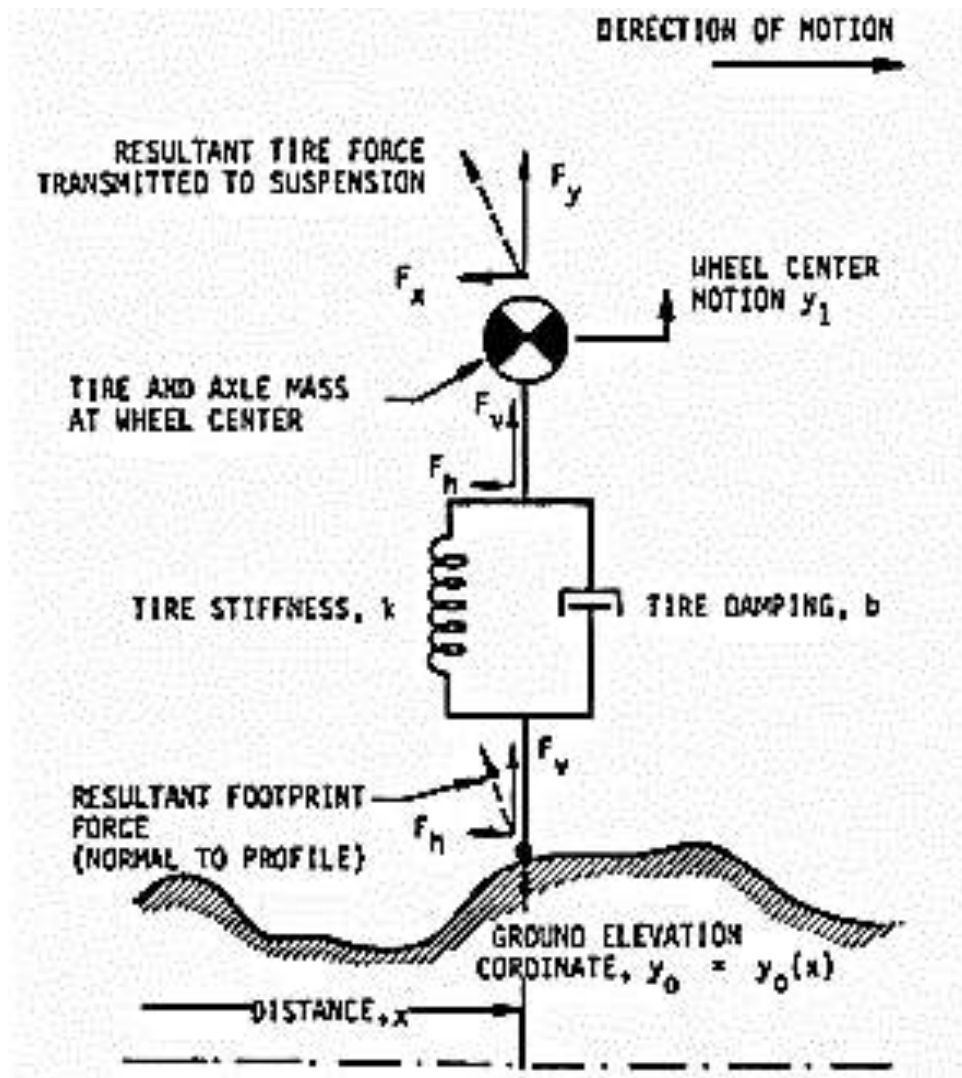


Figure 1-8 The Single Point Contact Model [11]

Due to the assumptions and simplifications that are made, not all analytical models work for all cases as one would expect. The single point contact model shown will be predominantly effective for some ride characteristics and purely vertical responses to road profile inputs, but the simplification of the tire-road contact point makes it not as effective for items such as rolling resistance prediction or analysis of forces in other directions. As the result requirements get more complicated, so too must the analytical model. In order to

accurately predict vertical load-deflection characteristics and rolling resistance, one could implement a flexible ring tire model developed by Loo in 1985 [13]. This analytical model features a flexible outer band as the contact method between the model and the road surface. This flexible band is then connected radially by springs and dampers to a rigid inner rim. There would in theory be an infinite number of these spring and damper units spaced closely together in order to represent the actual tire's behavior as closely as possible. A representation of Loo's flexible ring tire model can be seen in [Figure 1-9](#).

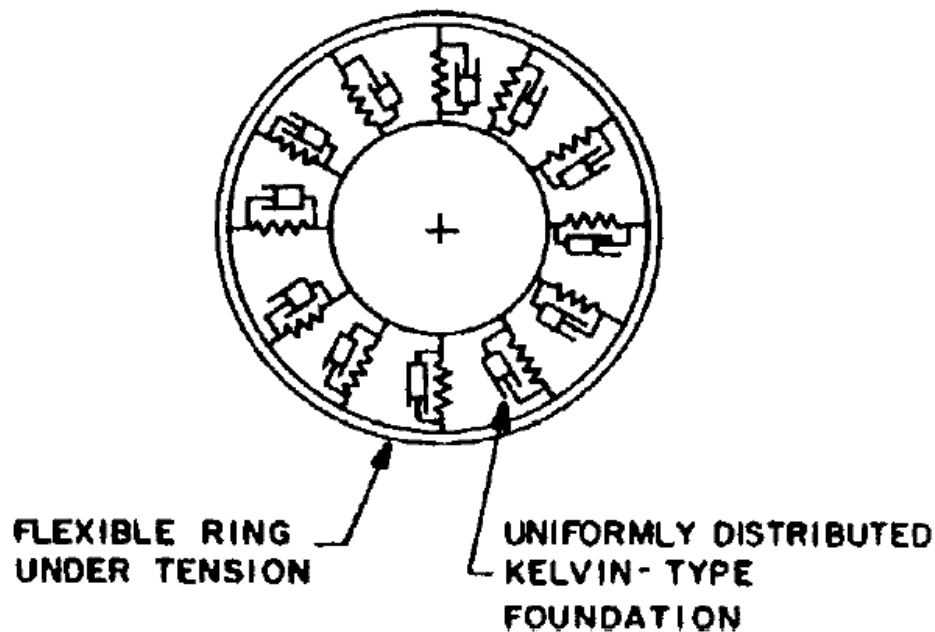


Figure 1-9 The Flexible Ring Tire Model [12]

The flexible tread band in this model is assumed to be massless, completely flexible and under tension from the spring and damper units. There are experiments required in order to gather all of the necessary parameters to populate this model. Specifically, there would need to be an understanding as to the vertical stiffness and damping properties of the desired tire model in order to tune this analytical model accordingly. The basis for the equations of motion of this flexible tire model are based on approximations made using the theory of a tensional string supported by an elastic foundation [14].

This model, due to its flexible tread band, would also be very suitable for envelopment research. Depending on the number of spring and damper units that have been implemented in a radial fashion, this model could predict the envelopment of the tire in a single plane rather effectively. While this model gains effectiveness compared to the single point contact model, it is still not effective when it comes to rotational dynamic behaviour and the way it describes the tire-road surface interactions. For these reasons, a more complex analytical model would be necessary to further describe the tire model's dynamic behaviour.

In 1997, Zegelaar and Pacejka proposed a rigid ring tire model in an effort to incorporate the rotational stiffness and damping qualities of a tire. In addition, they had aimed as well as describe the tire-road interface more effectively. The in-plane rigid ring model which they developed can be seen in [Figure 1-10](#).

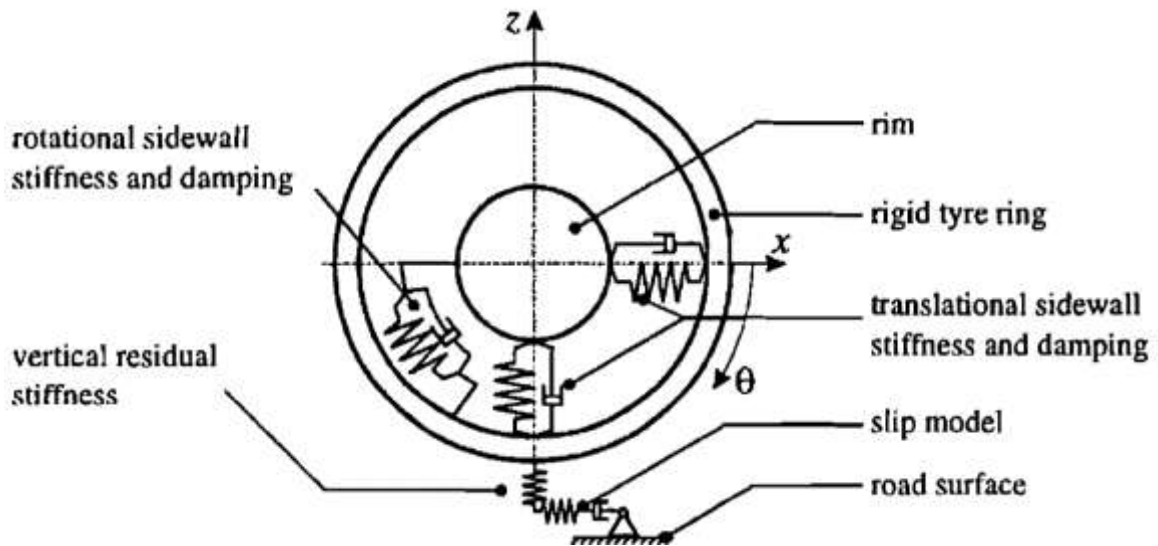


Figure 1-10 The In-Plane Rigid Ring Tire Model [14]

The goal of this rigid ring tire model was to more accurately predict the behaviour of a passenger car tire and study the tire responses to brake torque variations [15]. The model was also developed to be used within vehicle simulations, so it was built in a way to make it accurate and robust for a large range of inputs. There are three main components to this tire model: the rigid tire tread ring, the rigid rim, and the sidewall. The rigid ring incorporates three degrees of freedom as well, being the longitudinal displacement, vertical displacement and rotation about the lateral axis. This model was very effective in predicting dynamic behaviour through many in-plane parameters.

Chae et al. then improved this model to feature the out-of-plane parameters in 2006 in order to model the lateral behaviour of the tire model [10]. The out-of-plane rigid ring model can be seen in [Figure 1-11](#).

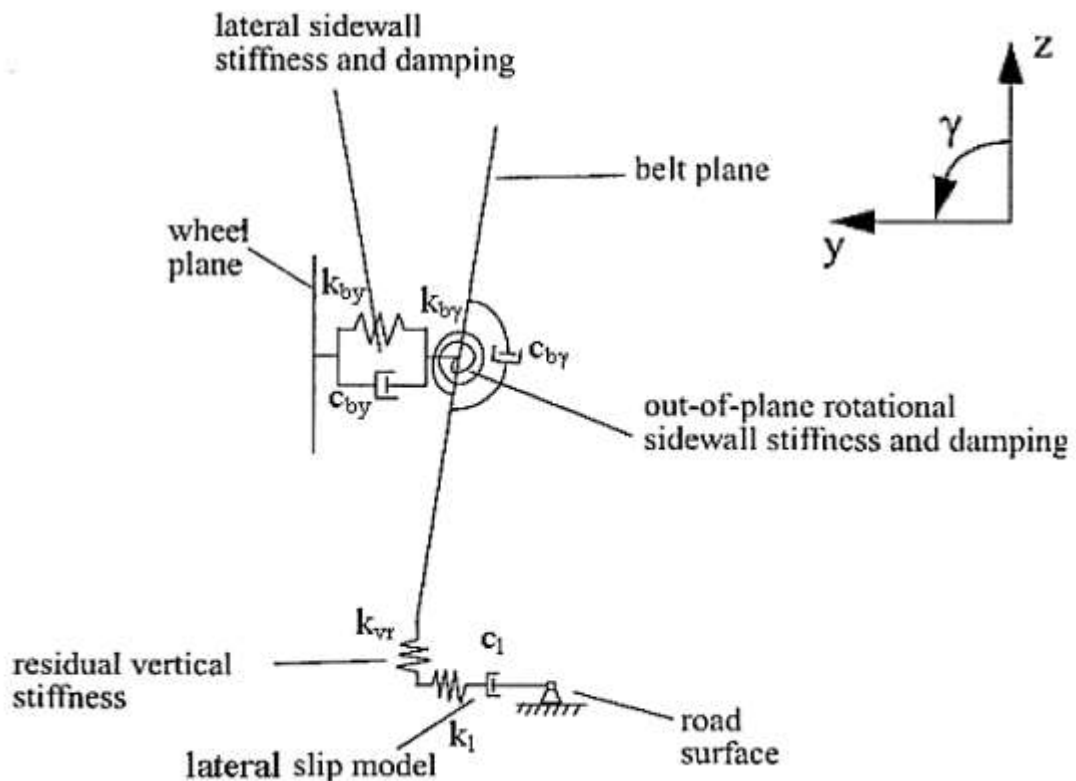


Figure 1-11 The Out-of-Plane Rigid Ring Model [9]

The out-of-plane model gives the possibility to also capture the behaviour of the sidewall, tread band and slip characteristics in a purely lateral association. Much like the in-plane rigid ring model, the various parameters are represented with spring and damper units to capture the stiffness and damping qualities in multiple directions. One major difference is the introduction of a radial spring and damper, which is necessary to describe the tire's out-of-plane rotational sidewall stiffness and damping (k_{by} and C_{by}).

In terms of analytical tire models, this is one of the most popular methods for parameterizing a physical tire for the purpose of quick and robust calculations. A vast amount of in-plane and out-of-plane parameters are calculated to populate this rigid ring model and thus is one of the most accurate models to run. However, the time and resources required to run all of the physical tire experiments are high due to the large amount of parameters that must be found beforehand.

1.4.6 FEA Tire Modeling

Since the 1970's, virtually generated tire models have widely grown in popularity as the computational requirements for such models have decreased. Finite Element Analysis (FEA) is an extremely useful representation for entities within virtual environments. This technique has been widely adopted in analyzing stress, strain and elastic/plastic deformation of very complicated structural models [10]. There are much more inputs available in FEA tire models in comparison to an analytical model, where one is usually only limited by the amount of information that is available. External factors such as temperature or aerodynamic resistances can be implemented and forces in all directions and planes can be analyzed simultaneously. Due to the significant increase in the amount of calculations and the amount of data for analysis, these FEA tire models drastically

increase the computational intensity of the solver networks. With an ever improving technology base, the physical time to run and solve these simulations has dramatically decreased in recent years.

Even with solver run times shortening, there is still a significant amount of preparation that must be done in order to properly represent these tire models in a FEA framework. Where analytical tire models are only concerned with the physical parameters for their spring-damper units, FEA tire models must not only know the physical dimensions, but also detailed material properties for all parts involved. When it comes to full tire models, there could be at least 25 different parts with as many individual materials needed for the proper construction.

Assuming there is access to all of the physical properties of a tire, the FEA construction method is required next. For this, there are many methods that one could implement in order to maximize the accuracy of the model with the available solving power. An early model developed by Padovan in 1977 was implemented as a two dimensional, curved, symmetric, thin shell element model for the examination of the power lost to rolling resistance and an analysis of the thermo-viscoelastic problem of steady-state rolling tires [14]. A representation of the two dimensional FEA tire model can be seen below in Figure 1-12.

The thin shell model developed by Padovan was initially successful in their effort to predict rolling resistance and thermal losses, however they fell under scrutiny for their neglect of any transverse shear deformation. These simple models would also neglect the anisotropic material behaviour and inflation pressures.

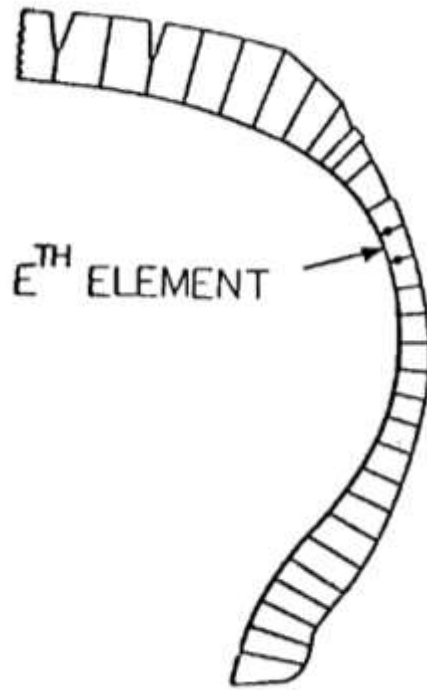


Figure 1-12 The Two Dimensional FEA Tire Model [13]

As computational power began to increase in the early 1990's, so too did the complexity of the FEA models. To overcome most of the restrictions of the simple two-dimensional FEA tire model, three-dimensional models began to be developed in an effort to further verify and quantify key predictions [14]. In 1994, Rhyne *et al.* [16] created a three-dimensional passenger car tire model in an effort to study how rim imperfections affected force variations and ride comfort. To comply with computational power at the time, their models were constructed of three-dimensional membranes and was completely rigid in the transverse direction. However, due to the membrane construction, it was still flexible in the rotational direction. Despite the transverse restrictions, it was found that the force variations were more sensitive to radial rim imperfections, but lateral rim imperfections are

much more common. The three-dimensional membrane tire model can be seen below in Figure 1-13.

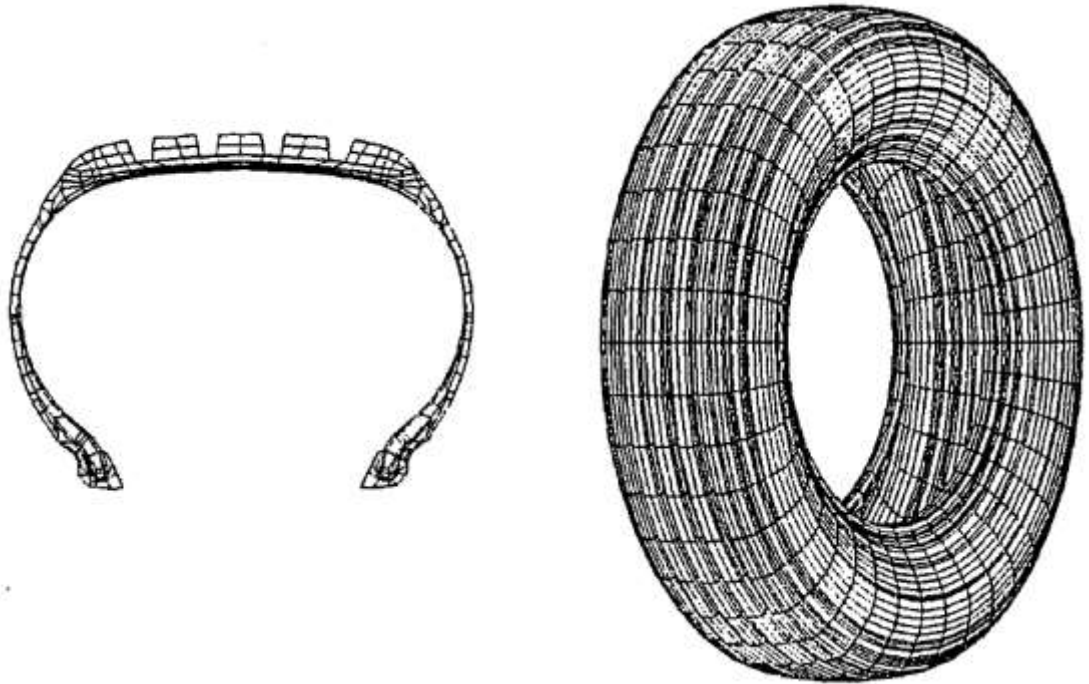


Figure 1-13 The Three-Dimensional Membrane Tire Model [15]

Full three-dimensional FEA models did not truly appear until a few years later, when in 1997 Kao *et al.* [17] constructed a fully element-based three-dimensional FEA tire model for the prediction and verification of tire transient dynamic responses from available tire design data [14]. This model incorporated the overall geometry, various material properties, fiber reinforcement, and Mooney-Rivlin coefficients for the proper rubber material characteristics. This full FEA model was attached to a rigid rim for proper assembly and used in a drum-cleat test to verify the transient responses in the tire sidewall and the standing wave that would be created post-cleat excitement. Figure 1-14 shows a zoomed section of the full FEA tire model and its dynamic cleat envelopment characteristics.

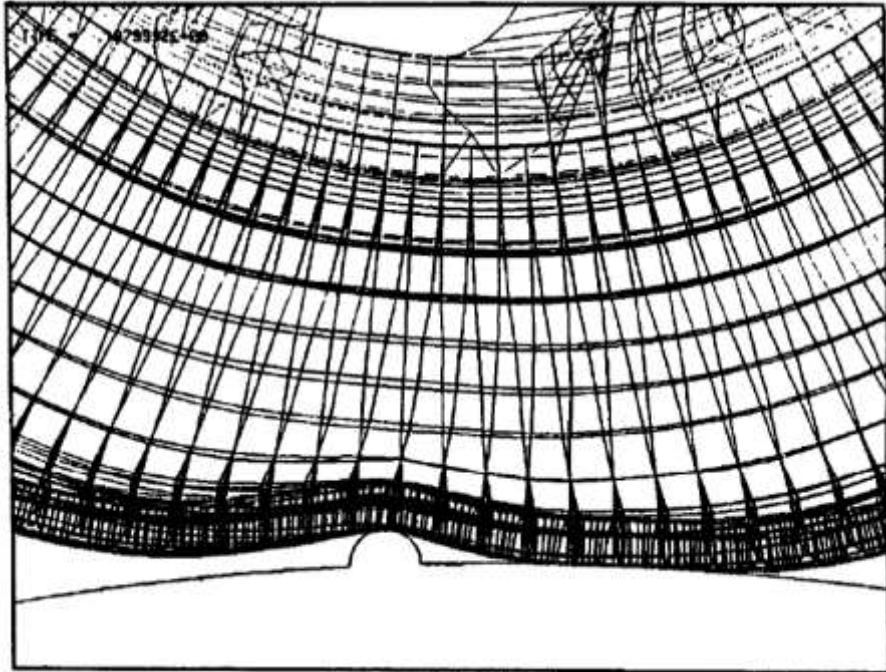


Figure 1-14 The Three-Dimension Full FEA Tire Model [16]

1.4.7 Advanced Optimization Techniques

In order to validate certain FEA models, various techniques and procedures are often borrowed from the realm of computer sciences. Optimization is the process of making something as whole or as perfect, as designed by a user, and has been adopted into numerous engineering fields. Since the tire model for this research would be fine-tuned for use within a virtual environment, at some point it may be necessary to make it as perfect as possible for tire-road interaction property prediction. With this foresight, a collection as to the relevant optimization strategies, algorithms, and procedures was attempted and provided in the proceeding sections.

1.4.8 Evolutionary Algorithms (EA)

Genetic algorithms are a family of computational models inspired by evolution [18], and was initially developed by J. Holland in the 1970's to understand the adaptive processes of natural systems [19]. By studying the process of evolution, this algorithm type has developed into a process composed of reproduction and mutation in order to promote diversity among possible solutions. The algorithm begins by creating a pseudo-random, quasi-random, sequential or parallel random population. That population then experiences a stochastic mutation, which probabilistically alters some of the population to promote diversity in the search. The population is then evaluated via a fitness function, and replaces an older generation of the population if it is more fit. The process continues until a given stopping criteria is met. In general, genetic algorithms perform efficiently during the exploitation phase, but are slightly slower during the exploration phase of the search.

1.4.9 Monte Carlo Methods

Many problems in engineering such as in logistics, production, telecommunications, finance, or computational biology (e.g. structure prediction of proteins, molecular docking) are based on simulation to evaluate the quality of solutions [19]. Monte Carlo Methods are commonly used in these situations in which a deterministic algorithm is infeasible to apply. Other applications include when it is too complex to create a closed form benchmark function for the algorithm. This optimization method begins by defining a range of acceptable inputs, and then computing the results from random inputs within that range. The results are then aggregated, and a solution is produced [19]. Due to the stochastic nature of the algorithm, this method is effective for exploring a vast search space. The Monte Carlo Method also resembles a 'guess and test' procedure.

1.4.10 Adaptive Response Surface Methodology (ARSM) Algorithms

For optimization problems involving computationally intense analysis or simulation, approximation models are usually used in an effort to reduce overall computation time [20]. Generic meta-modelling techniques make iterative improvements to the solutions by adjusting the search space of the input parameters. The adaptive response surface method, however, uses quadratic approximation models for the computation-intensive design objective function in a gradually reduced search space [20]. The objective function is approximated by testing samples of solutions from the simulation results to generate a quadratic response surface. The algorithm then approximates where the optimal solutions should lie from this response surface to help in the exploration phase. Additional solved solutions help to better define the response surface and aid in the exploitation phase. The adaptive component refers to the type of parameter-tuning within the algorithm. The parameters are tuned in an online procedure, which takes place during the search and is performed using the memory of the search. Within PAM-OPT, there does exist the option of implementing a non-adaptive or dynamic parameter-tuning method, which randomly changes the parameters without taking into account the search progress. This dynamic method helps to promote diversity in the search but would drastically increase the CPU time and reduce the overall accuracy.

1.4.11 Parameter-Tuning

Unlike mathematical programming, there exist optimization problems in which a clear relationship between the optimization design parameters and the objective function are not known. Some problems exist in such a way that problems cannot be formulated with an unambiguous analytical mathematical notation [19]. In this case, the objective function may be a black box. In a black box optimization problem, there exists an analytically

unknown relationship between the design parameters and the fitness of the system. This black box approach is commonly necessary in virtual simulations, in which there exists such a high level of complexity and non-linearity

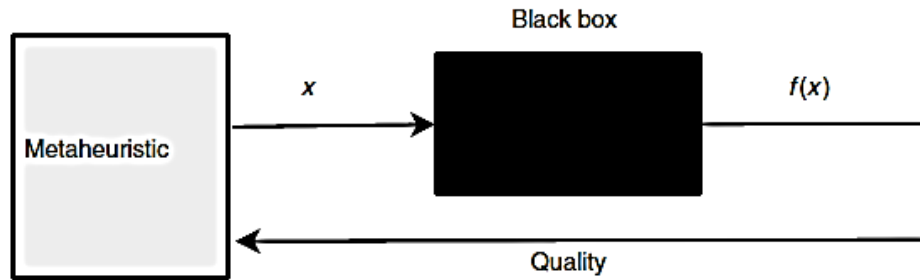


Figure 1-15 A Black Box Optimization Scenario for an Objective Function

Due to the nature of this thesis research, the black box strategy is necessary to be implemented within a parameter-tuning algorithm. Parameter-tuning is the altering of design parameters through multiple simulations in order to make the behaviour of a system match known objectives. The fitness of the system is evaluated by the difference between the simulated behaviour and the predicted behaviour. Multiple algorithms could be used for this overall technique, including EA, ARSM, Monte Carlo Methods, Particle Swarm Optimization (PSO), and many others.

CHAPTER 2: FEA TIRE CONSTRUCTION

The following chapter outlines the construction procedure that was used in order to recreate the wide base tire in a virtual environment. A Michelin XONE XDA 445/50R22.5 was the chosen tire to be virtually recreated. The utilized programs, construction method, difficulties, limitations, available data and overall progression to the full model is all covered in this chapter.

2.1 MODELING PROGRAMS

The software that was used to create the FEA tire model was the Virtual Performance Solution (VPS) series from ESI Group. This software package includes some of their flagship programs, such as PAM-CRASH, PAM-MESH, PAM-VIEWER, and PAM-OPT, all of which were used at some point during this construction process. This popular package is used for virtual crash testing by many commercial vehicle manufacturers due to ability to accurately model complex and highly non-linear systems [6].

Within the Virtual Performance Solution (VPS) series lies PAM-CRASH, which is a fully integrated application for crash test simulations, casting, stamping, and composite forming processes. It also allows for advanced virtual environments to be created in which highly non-linear FEA tire models can exist and replicate complex driving maneuvers.

For the modelling portion, PAM-MESH was primarily used for the modelling of the FEA tire as it allows for increased functionality in FEA modelling. PAM-CRASH was the main application used for the development of the simulations and the virtual environments. PAM-VIEWER is the main component of this software package that allows the simulations to be studied, and was thus used for the analysis of the FEA simulations.

2.2 DIFFICULTIES AND LIMITATIONS

Before the modelling could take place, the overall geometry of the physical tire that was requested to be modelled in an FEA environment was needed. It was determined before the majority of this research took place to attempt to replicate a Michelin XONE XDA 445/50R22.5 wide base tire. Some of the geometry was simple enough to acquire through online brochures and published sources. Other geometry, however, was unavailable at the time so an actual Michelin XONE XDA tire was purchased and cut into sections for analysis. By doing so, measurements of the sidewall thicknesses, undertread and undertread membranes were more evident and could thus be implemented into the FEA model.

With the dimensions known, the next important item to implement was the material properties for all of the components of the tire model. The material properties were made unavailable from the manufacturer, for obvious reasons, so for the initial stages of development the tire model would incorporate the material properties of an older tire model that had available material data accessible. This would allow for initial simulation debugging to take place and the fine tuning of the material properties would be completed at a later stage, outlined in Chapter 4. In reality, the inspiration for all of the work completed in the Chapter 4 was due to the material properties being unavailable and attempting to work around this issue.

2.3 AVAILABLE DATA FOR CONSTRUCTION

As stated earlier in this chapter, the tire geometry, general construction layout, and similar material properties were available to model this tire. In addition, predicted ranges for certain performance characteristics such as the model's total vertical stiffness (k_{tot}), lateral stiffness (k_l), and relaxation length (σ) were also provided for the initial simulation of the tire model. All of the available data, whether donated for research purposes or determined from the physical model, have been collected and shown in Table 2-1.

Table 2-1 Available Data for Michelin XONE XDA Construction

DIMENSION	VALUE
Tire Size	445/50R22.5
Rim Diameter	571.5 mm
Sidewall Width	445 mm
Sidewall Height	223.75 mm
Unloaded Overall Diameter	1019 mm
Loaded Radius	471 mm
Rated Inflation	8.3 bar
Rated Vertical Load	4625 kg
Overall Weight (Excluding Rim)	80.08 kg
Mass of the Tire Belt (m_b)	70.75 kg
Weight of the Rim (m_{rim})	31.17 kg
Total Weight of the Tire (m_{tire})	111.25 kg
Contact Patch Length ($2a$)	200.12 mm
Contact Patch Width (w)	379.32 mm

2.4 PROGRESSION TO CONSTRUCTED FEA MODEL

The majority of the geometry was extracted from the section-cut of the XONE XDA. Along with the simple measurements, the section-cut tread was used to produce a tread pattern negative, shown in [Figure 2-1](#). Without actual technical drawings for this tire, the footprint was used in order to gather the specific geometry of the tread pattern so that it could be closely replicated.

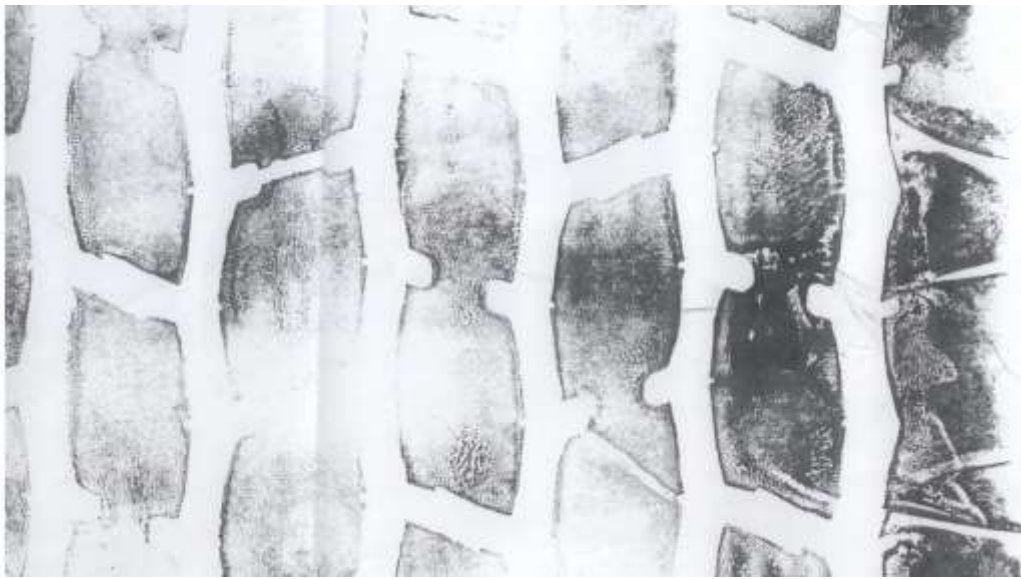


Figure 2-1 Footprint Negative for the Michelin XONE XDA

The tread negative was loosely traced in order to develop what would become the geometry for the tire model. The shapes of the tread patterns were approximated as closely as possible while trying to keep the complexity of the FEA model in mind. If the tire model was constructed with the utmost precision to the real model, it would create a tire model that was too complex to simulate in a feasible amount of time. With the computing power that was available at the time of this research, the element count had to be managed in order to complete research targets by specified dates. Thus, slight generalities were implemented

into the tread pattern. The approximated geometry can be seen in [Figure 2-2](#), in which the footprint negative was used to plan the FEA framework of the tread pattern, groove trough locations, and positioning of all of the nodes that would be required to create this tread model.

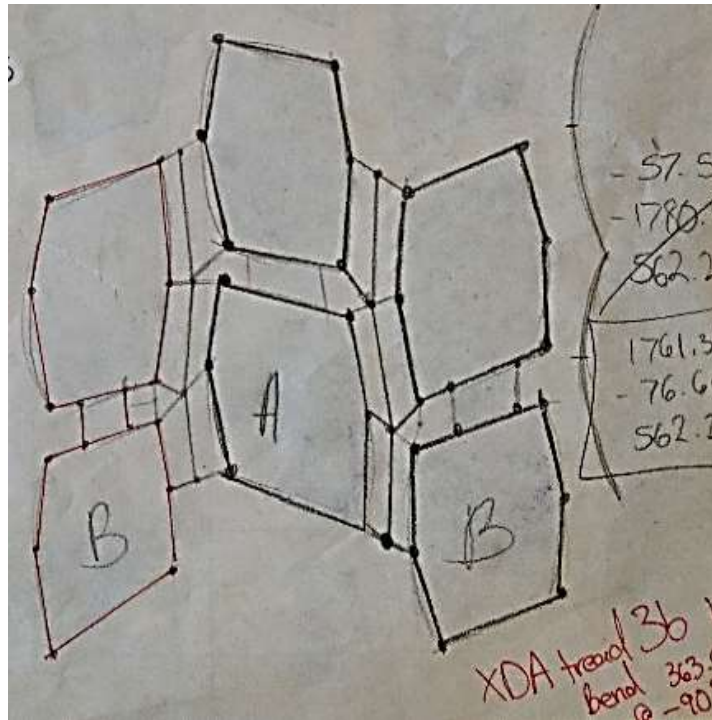


Figure 2-2 Initial Planning of the Tire Tread FEA Framework

From the general tread geometry and FEA framework, the initial modelling stages took place using PAM-MESH. The tread imprint was modelled, extruded, and drafted to a simple repeating section-cut. The progression from 2D to 3D can be seen in [Figure 2-3](#). The length of the tread section that was created was chosen such that it could be revolved evenly to complete the full tire model.

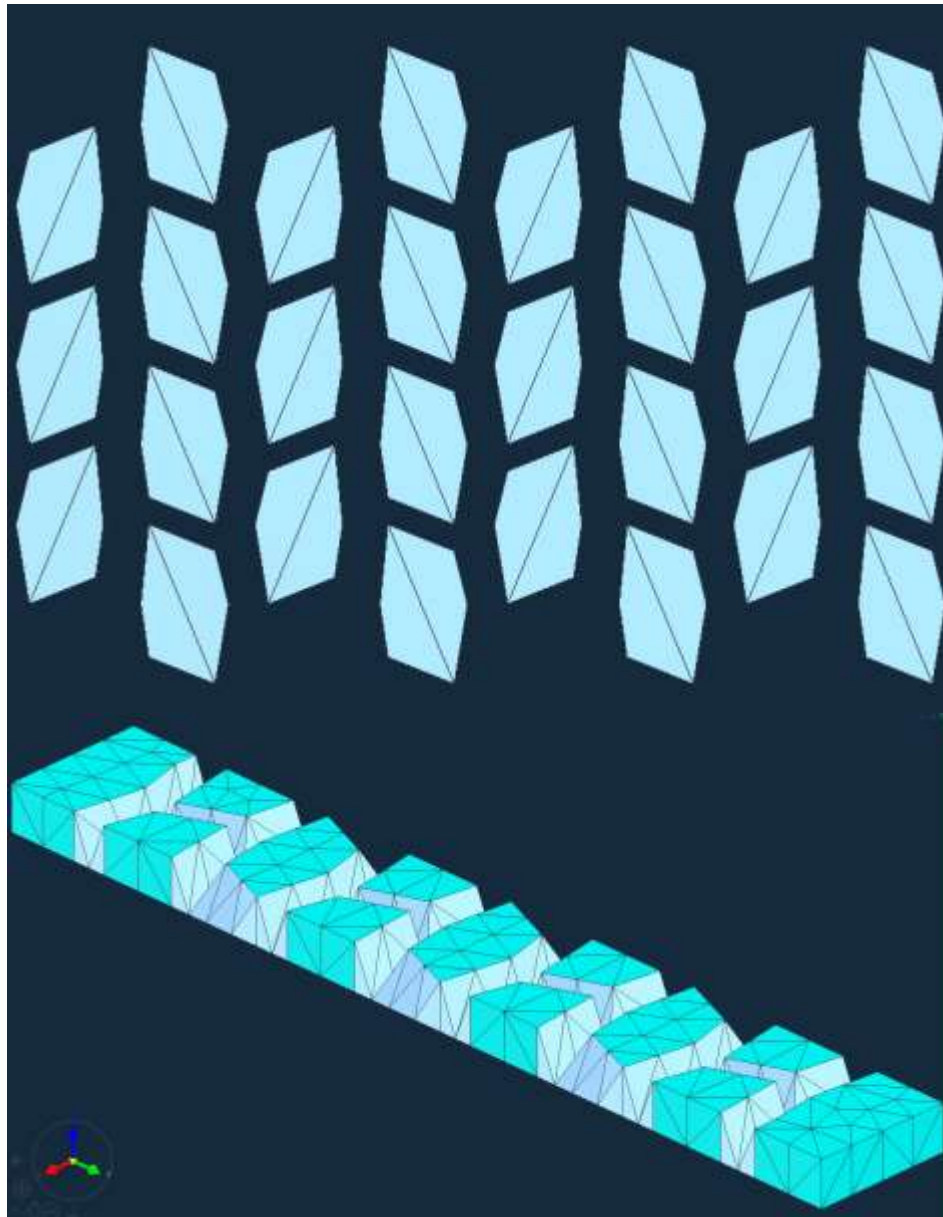


Figure 2-3 2D Construction (Left) and 3D Construction (Right) of the Tire Tread

The tire carcass was modelled in a similar fashion as the tread, as the physical section-cut was measured and then used to closely model the tire in PAM-MESH. Using techniques developed by Chae [10], Slade [1] and Dhillon [6], the tire model sidewall was not modelled using 3D elements.

Due to the complex construction within the tire sidewall, the intricate modelling of the rubber compounds, tire belt and beams are extremely difficult to model properly. However, PAM-MESH from ESI Studios has the ability to implement a layered membrane material which corresponds to a linear elastic membrane material. This material consists of two sets of fibers which are arranged at a user defined angle and are embedded in an isotropic matrix parent film material [6]. The nature of the layered membrane, shown in [Figure 2-4](#), allows for the complex belt plies, radial cords and the rubber matrix to all be modelled harmoniously. This multilayer membrane was also implemented in the undertread layer to again model the belts found within the rubber matrix.

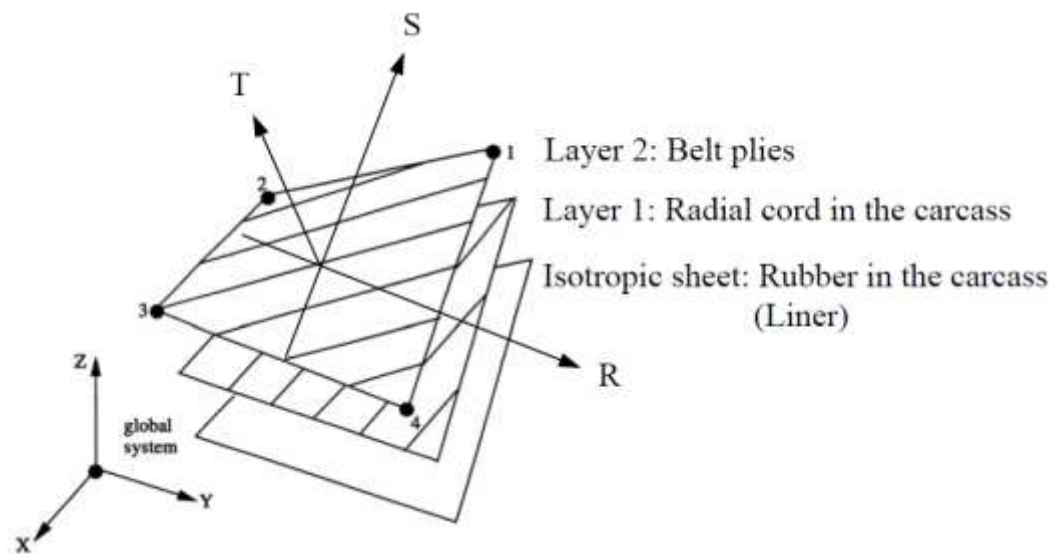


Figure 2-4 Schematic of a Three-Layered Membrane Element [34]

By using the multilayer membranes and various 3D elements, the tire carcass was created. A generic rim was also inserted into the model, which was constructed of a null material and made into a rigid body upon creation. The carcass and rim assembly was then cut to the same length of the tread model and the three separate models were merged into the completed section-cut model, shown in [Figure 2-5](#).

during this initial testing, and some of the simpler model parameters such as total vertical stiffness (k_{tot}) and lateral stiffness (k_l) were calculated to benchmark the initial model and predict material parameter search spaces for speed and robustness. At this point, the XONE XDA V1.0 was deemed acceptable for parameter-tuning optimization procedure. A comparison of the UOIT XONE XDA¹ V1.0 to the physical Michelin XONE XDA can be seen in [Figure 2-6](#).



Figure 2-6 Visual Comparison of the Physical Michelin XONE XDA to the FEA UOIT XONE XDA

¹ The naming of the tire model becomes the UOIT XONE XDA as the material properties of the Michelin XONE XDA are still unknown. It would not be precise to refer to the model as a Michelin XONE XDA tire model since the accuracy to the physical tire is unconfirmed.

CHAPTER 3: COLLECTION OF EXPERIMENTAL DATA

In this chapter, the rolling resistance experiments that were conducted at the Volvo Group North America Greensboro Campus in Greensboro, North Carolina, are explained in detail. Various aspects such as the testing equipment, experiment procedure, expected and collected results are all included. The tire used for these experiments was a Michelin XONE Energy Line-T 445/50R22.5L, which is of the same size but a slightly different tread pattern.

3.1 EXPERIMENT GOALS

In order to properly validate any computer generated model, whether it a pneumatic tire or the entire vehicle, considerable physical data is required. The dynamic characteristics of the tire are just as important as the geometry as the virtual model must perform as close as possible to the physical counterpart. Without a significant amount of accuracy, the model will incorrectly predict various longitudinal and cornering characteristics and can actually hinder the research and development process. Therefore, the goal of this experiment was to capture the dynamic behaviour of the tire in order for it to be incorporated into the advanced optimization parameter-tuning procedure for full tire validation.

It was proposed to capture the tire forces measured at the wheel center from multiple driving events to incorporate as much data as possible into the parameter-tuning script. The events took place at the Greensboro Proving Grounds and included steady state rolling resistance, vertical excitation due to a speed bump, steady state cornering and rolling resistance through a soft soil ditch. The events were also chosen to satisfy current and future

aspects of an ongoing research project. These driving events would then be recreated using FEA software with the FEA tire model as well in order to prove the accuracy of the model.

3.2 EXPERIMENTAL SETUP

For this experiment, a 2012 Volvo VNM-98 6x2 Truck Tractor was equipped with 4 wheel force transducers in order to record the various forces that were exerted on the tires during the driving maneuvers. The transducers were fitted to the front left and front right wheels to capture the forces at the steering axle. On the front axle, the vehicle was fitted with a pair of Bridgestone R283 275/80R22.5H tires inflated to 120 PSI. Two more transducers were fitted on the pusher axle, which acts to support the weight of the trailer and are non-driven wheels. A pair of Michelin XONE Energy Line-T 445/50R22.5L tires were used on the pusher axle, also inflated to 120 PSI. The pusher axle, which included the wide base Michelin tires, was the main axle of interest due to the immediate validation work that would proceed the experiments. The steering axle was also equipped with the measurement devices for future research topics as well as to compare the difference in readings between the steered and dragged axles. The implementation of the wheel force transducers can be seen in [Figure 3-1](#).



Figure 3-1 Wheel Force Transducer (Right) [20] Mounted Onto the Volvo Truck Tractor (Left)

The wheel force transducer that was used was a LW-2T-50K from Michigan Scientific Corporation. It is a 6-axis transducer that measures forces and moments on a mounted vehicle wheel [21]. The transducer incorporates six independent strain gage bridges which measure the difference in strain that is experienced at each strain bridge. These bridges are able to do so by deforming under various force changes and fluctuating its electrical resistance by taking advantage of its characteristics of electrical conductance. The strain bridges are aligned in such a way to isolate for each translational force (longitudinal F_x , lateral F_y , and vertical F_z) as well as each moment (overturning M_x , rolling resistance M_y , and aligning M_z). It is from these measurement devices that the required data would be gathered and implemented into the parameter-tuning optimization algorithms.

3.3 DATA ACQUISITION

The instrumented truck was instructed to drive the oval test track a total of 3 times at varying speed and varying vertical load in order to gather data related to the rolling resistance properties of the instrumented tires. The procedure was repeated at varying speed and load with the speed bump added to the track for the ability to collect the vertical excitement data for possible validation simulations. Lastly, the instrumented truck drove through a drainage ditch that had been filled with loose and dry sand to capture the rolling resistance properties through soft soils for possible soft soil validation as well. The soft soil rolling resistance bobtail experiment can be seen in [Figure 3-2](#).



Figure 3-2 Instrumented Truck Tractor Driving Through Soft Soil Ditch

In order to incorporate most of the requested testing procedures, 4 vertical loads were examined. The bobtail was run first, measuring in at an average force of 1160.95 lbs. The other trailers used measured in at 2819.09 lbs, 8734.51 lbs and 9342.23 lbs. One experiment



Figure 3-3 Volvo Tractor Trailer During Rolling Resistance Experiment

was also run at 2 inflation pressures. Loaded Trailer 2 (8734.51 lbs) ran the course twice, once at the rated pressure of 120 psi and again at 80 psi. A visual of the Volvo Tractor Trailer during one of the experiments can be seen in [Figure 3-3](#).

The wheel force transducers were able to provide a wide variety of information regarding the measured forces on the steering axle tires and the pusher axle tires as well as real-time GPS data. The data was available as specific channels that were captured by the onboard instrumentation controller. All of the available data can be seen in [Table 3-1](#).

Table 3-1 Available Channel Data from Instrumentation

CHANNEL	NAME
1	'GPS@lat.RN_1'
2	'GPS@lon.RN_1'
3	'GPS@altitude.RN_1'
4	'GPS@speed_mph.RN_1'
5	'GPS@heading.RN_1'
6	'Data@LM_X_Force.RN_1'
7	'Data@LM_Y_Force.RN_1'
8	'Data@LM_Z_Force.RN_1'
9	'Data@LM_MX_Moment.RN_1'
10	'Data@LM_MY_Moment.RN_1'
11	'Data@LM_MZ_Moment.RN_1'
12	'Data@LM_Velocity.RN_1'
13	'Data@LM_Position.RN_1'
14	'Data@LM_X_Acceler.RN_1'
15	'Data@LM_Z_Acceler.RN_1'
16	'Data@RM_X_Force.RN_1'
17	'Data@RM_Y_Force.RN_1'
18	'Data@RM_Z_Force.RN_1'
19	'Data@RM_MX_Moment.RN_1'
20	'Data@RM_MY_Moment.RN_1'
21	'Data@RM_MZ_Moment.RN_1'
22	'Data@RM_Velocity.RN_1'
23	'Data@RM_Position.RN_1'
24	'Data@RM_X_Acceler.RN_1'
25	'Data@RM_Z_Acceler.RN_1'
26	'Data@LF_X_Force.RN_1'
27	'Data@LF_Y_Force.RN_1'
28	'Data@LF_Z_Force.RN_1'

29	'Data@LF_MX_Moment.RN_1'
30	'Data@LF_MY_Moment.RN_1'
31	'Data@LF_MZ_Moment.RN_1'
32	'Data@LF_Velocity.RN_1'
33	'Data@LF_Position.RN_1'
34	'Data@LF_X_Acceler.RN_1'
35	'Data@LF_Z_Acceler.RN_1'
36	'Data@RF_X_Force.RN_1'
37	'Data@RF_Y_Force.RN_1'
38	'Data@RF_Z_Force.RN_1'
39	'Data@RF_MX_Moment.RN_1'
40	'Data@RF_MY_Moment.RN_1'
41	'Data@RF_MZ_Moment.RN_1'
42	'Data@RF_Velocity.RN_1'
43	'Data@RF_Position.RN_1'
44	'Data@RF_X_Acceler.RN_1'
45	'Data@RF_Z_Acceler.RN_1'

From the available data, the longitudinal forces (F_x), vertical loads (F_z), rolling radius (r), and rolling resistance moment (M_y) were collected in order to determine the specific tire's rolling resistance coefficients (RRC) where:

$$RRC_1 = \frac{F_x}{F_z} \quad 3-1$$

$$RRC_2 = \left(\frac{M_y}{r} \right) / F_z \quad 3-2$$

Currently, only the steady state rolling resistance data has been extracted from the test data. The vertical excitement data is still to be treated, but the available rigid road and soft soil rolling resistance runs have been isolated. The speed-bump experiment results will be used for future portions of this ongoing research project. An example of the vertical excitation experiment can be seen in [Figure 3-4](#).



Figure 3-4 Volvo Truck Tractor (Without Trailer) Experiencing Vertical Excitation

3.4 TEST TRACK RESULTS

There was a noticeable difference between the left and right tires on both the steered and pusher axle. In order to compensate for this, statistical averages were taken on the front and rear axles in order to find a mean rolling resistance between left and right tires.

There were also some discrepancies between experiment speeds, in that there were supposed to be one medium speed (7 mph) and one high speed (15 mph) to be run for all cases. It would appear, however, that some experiments were run at 5 mph, 7 mph, 8 mph, and 15 mph for the various vertical loads. In order to have equal comparison, the most consistent speed of 15 mph was chosen to represent the validation criteria.

A collection of all of the average data taken from the pusher axle which featured the wide base tires can be seen below. The data was collected for each loop of the steady state rolling resistance on both sides of the track (denoted as sides A and B), in case of discrepancy. The average F_x , or AV FX value, is an average between the left tire and right tire for that specific run. The average, listed at the end of the table, is an average of runs 1A to 3B.

Table 3-2 Configuration 1: Bobtail (1160.95 lbs, 120 PSI)

EXP1		1A	1B	2A	2B	3A	3B	AVERAGE
AV FX	LBS	28.43782	31.07555	20.30991	19.80876	19.21582	25.36527	24.03552
AV FZ	LBS	1247.368	1086.699	1209.652	1088.993	1231.036	1101.93	1160.946
AV FX/FZ	RRC	0.020901	0.02619	0.014868	0.016216	0.013865	0.020795	0.018806

Table 3-3 Configuration 2: Trailer 1 (2819.09 lbs, 120 PSI)

EXP2		1A	1B	2A	2B	3A	3B	AVERAGE
AV FX	LBS	42.05559	39.96792	46.042	42.5162	46.41116	43.53525	43.42135
AV FZ	LBS	2759.48	2887.306	2692.099	2890.843	2847.918	2896.895	2829.09
AV FX/FZ	RRC	0.014964	0.013673	0.016538	0.014494	0.016041	0.014835	0.015091

Table 3-4 Configuration 3: Trailer 2 (8734.51 lbs, 120 PSI)

EXP3		1A	1B	2A	2B	3A	3B	AVERAGE
AV FX	LBS	246.3874	215.4485	236.5963	211.4678	246.8591	220.7743	229.5889
AV FZ	LBS	8575.975	8888.903	8637.625	8882.469	8548.116	8873.984	8734.512
AV FX/FZ	RRC	0.028533	0.024296	0.027316	0.023903	0.028762	0.024904	0.026286

Table 3-5 Configuration 4: Trailer 3 (9342.23 lbs, 120 PSI)

EXP4		1A	1B	2A	2B	3A	3B	AVERAGE
AV FX	LBS	153.4325	142.9087	188.412	153.602	175.3554	153.677	161.2312
AV FZ	LBS	9241.221	9462.173	9123.203	9503.096	9219.812	9503.85	9342.226
AV FX/FZ	RRC	0.016521	0.015217	0.020566	0.016292	0.019021	0.01637	0.017331

Table 3-6 Configuration 5: Trailer 2 (8734.51 lbs, 80 PSI)

EXP5		1A	1B	2A	2B	3A	3B	AVERAGE
AV FX	LBS	181.2757	173.9665	202.3035	170.985	196.3818	190.4474	185.8933
AV FZ	LBS	8799.352	8966.615	8600.698	9144.435	8775.073	8901.735	8864.651
AV FX/FZ	RRC	0.020593	0.019411	0.023532	0.018729	0.022374	0.021398	0.021006

The data collected above was then plotted to show the difference in the left and right tires on the pusher axle. As it can be seen in [Figure 3-5](#), the right tire registered a higher rolling resistance coefficient than the left. This is believed to be due to the imbalance in weight distribution during the experiments. For the parameter-tuning optimization script, it was decided to aim the objective function towards matching the average rolling resistance coefficient between the left and right tires.

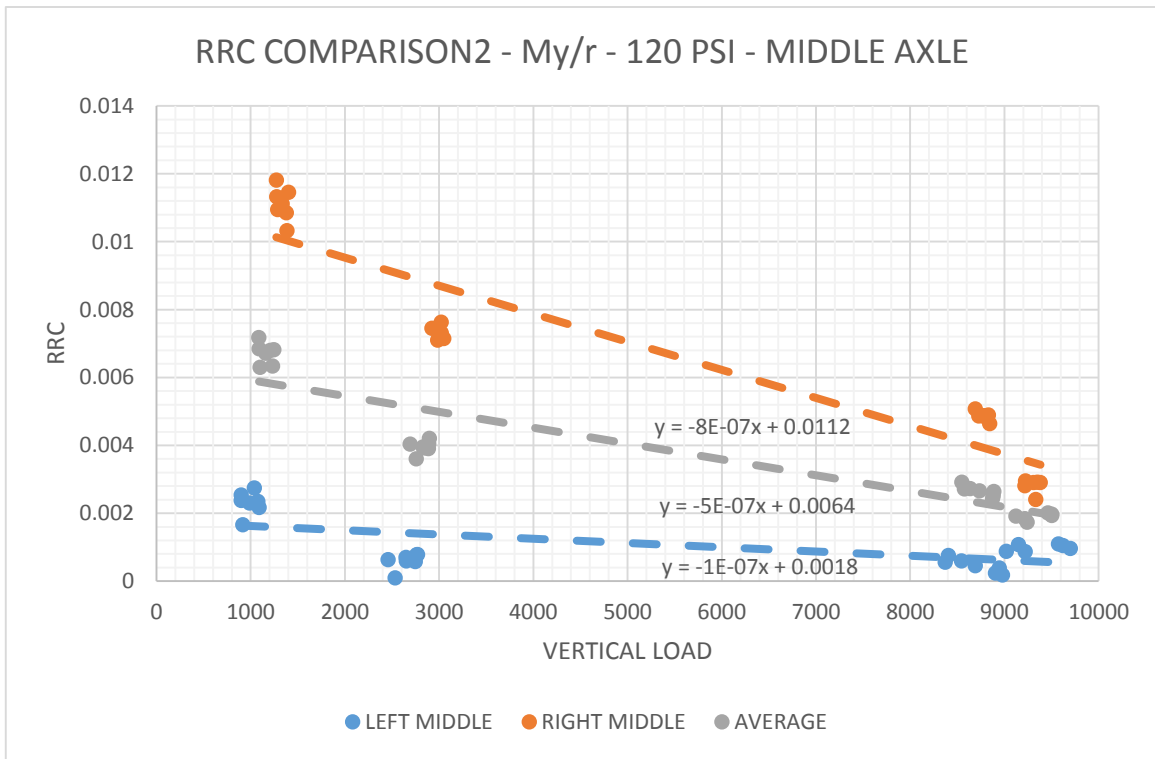


Figure 3-5 Rolling Resistance Results (RRC₁) for Left and Right Tires

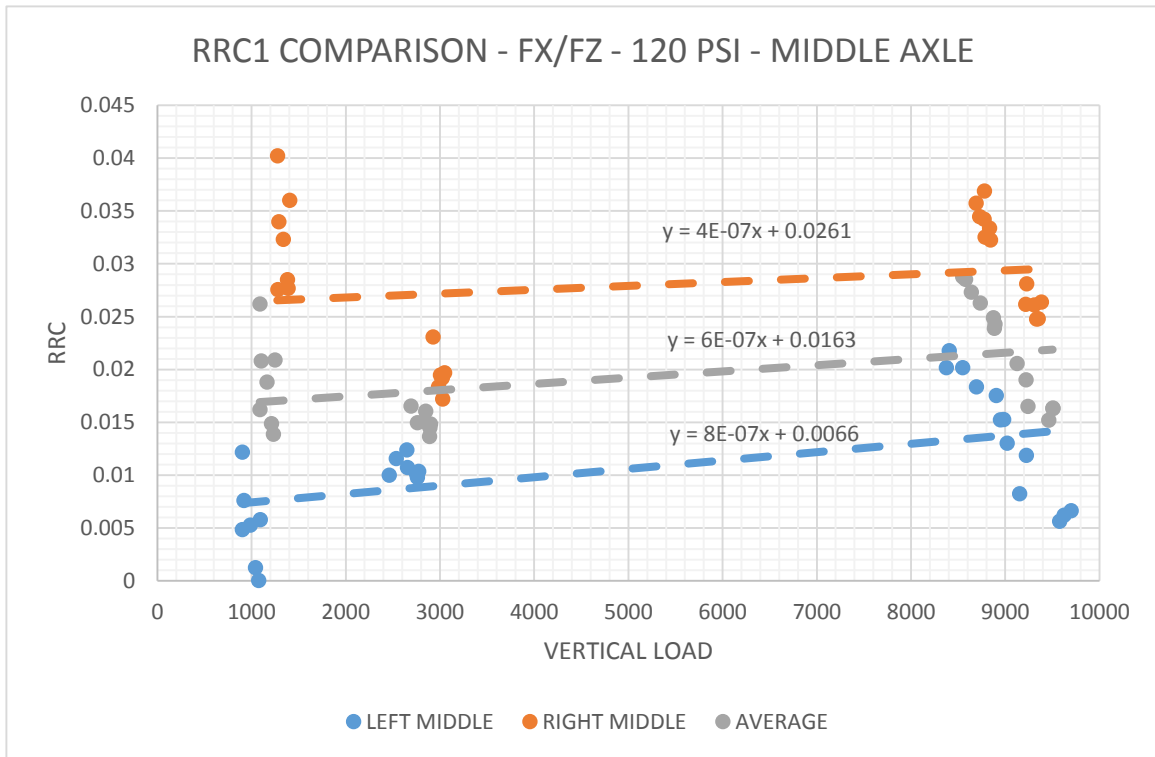


Figure 3-6 Rolling Resistance Results (RRC₂) for Left and Right Tires

3.5 SAND BOX RESULTS

A similar procedure was conducted within the sandbox in that multiple passes were made through the soft soil with varying vertical load but constant speed. In this experiment, only the left side of the vehicle would enter the sandbox. This was done to avoid the vehicle getting stuck within the sand due to the heavy load and low speed combination. All of the data presented is from the left side of the vehicle, from both the steering axle and pusher axle. The abbreviation LM refers to the left tire on the middle axle while LF refers to the left tire on the front axle. The corresponding data from all three runs can be seen below at varying vertical load, varying inflation pressure, and a constant speed of 5 mph.

Table 3-7 Configuration 1: Bobtail (1160.95 lbs, 120 PSI)

SAND1		RUN 1	RUN 2	RUN 3	AVERAGE
LM FX	LBS	515.432373	468.7344666	503.4161987	495.8610128
LM FZ	LBS	1792.898315	1790.104492	1741.919189	1774.973999
LM FX/FZ	RRC	0.287485558	0.261847545	0.289000892	0.279444665
LF FX	LBS	920.6690674	948.5772705	931.4692383	933.5718587
LF FZ	LBS	4874.364258	4860.130371	4922.552734	4885.682454
LF FX/FZ	RRC	0.188879825	0.195175273	0.189224837	0.191093311

Table 3-8 Configuration 2: Trailer 1 (2819.09 lbs, 120 PSI)

SAND2		RUN 1	RUN 2	RUN 3	AVERAGE
LM FX	LBS	710.0192871	710.0192871	830.5427856	750.1937866
LM FZ	LBS	2582.943848	2582.943848	2876.933105	2680.940267
LM FX/FZ	RRC	0.27488762	0.27488762	0.288690336	0.279488525
LF FX	LBS	865.6398926	865.6398926	854.6019287	861.9605713
LF FZ	LBS	5158.943359	5158.943359	5108.637695	5142.174804
LF FX/FZ	RRC	0.167794029	0.167794029	0.16728568	0.167624579

Table 3-9 Configuration 3: Trailer 2 (8734.51 lbs, 120 PSI)

SAND3		RUN 1	RUN 2	RUN 3	AVERAGE
LM FX	LBS	1248.482422	1285.170776	1302.020874	1278.558024
LM FZ	LBS	8561.549805	8906.079102	8650.881836	8706.170248
LM FX/FZ	RRC	0.145824348	0.144302646	0.150507301	0.146878098
LF FX	LBS	902.4622803	889.206604	897.9633179	896.5440674
LF FZ	LBS	5870.071289	5774.270508	5828.740234	5824.360677
LF FX/FZ	RRC	0.153739578	0.153994622	0.154057872	0.153930691

Table 3-10 Configuration 4: Trailer 3 (9342.23 lbs, 120 PSI)

SAND4		RUN 1	RUN 2	RUN 3	AVERAGE
LM FX	LBS	1315.229614	1319.932861	1043.989746	1226.384074
LM FZ	LBS	8026.730957	8678.740234	7846.599121	8184.023437
LM FX/FZ	RRC	0.163856198	0.152088071	0.133049966	0.149664745
LF FX	LBS	982.7498169	881.2505493	1101.876465	988.6256104
LF FZ	LBS	5586.678223	5748.633301	5666.395996	5667.23584
LF FX/FZ	RRC	0.175909508	0.153297402	0.194458076	0.174554995

Table 3-11 Configuration 5: Trailer 2 (8734.51 lbs, 80 PSI)

SAND5		RUN 1	RUN 2	RUN 3	AVERAGE
LM FX	LBS	1024.674072	866.4907837	924.3238525	938.4962361
LM FZ	LBS	8646.768555	8168.985352	8118.435059	8311.396322
LM FX/FZ	RRC	0.118503701	0.106070797	0.11385493	0.112809809
LF FX	LBS	951.3912354	801.9143677	801.6296387	851.6450806
LF FZ	LBS	5782.307129	5788.584473	5553.842285	5708.244629
LF FX/FZ	RRC	0.164534884	0.138533759	0.144337847	0.149135497

It can be seen in [Figure 3-7](#) that the steered and pusher axle in the soft soil will experience very similar variation in the RRC with respect to vertical load. Although the range of loads experienced from the various trailer changes obviously do not exhibit the same amount of force on all axles, the slope of the trend line for both axles appears remarkably close. This is interesting as two different types of tires are used on these axles, and yet the change in resistance appears to be the same.

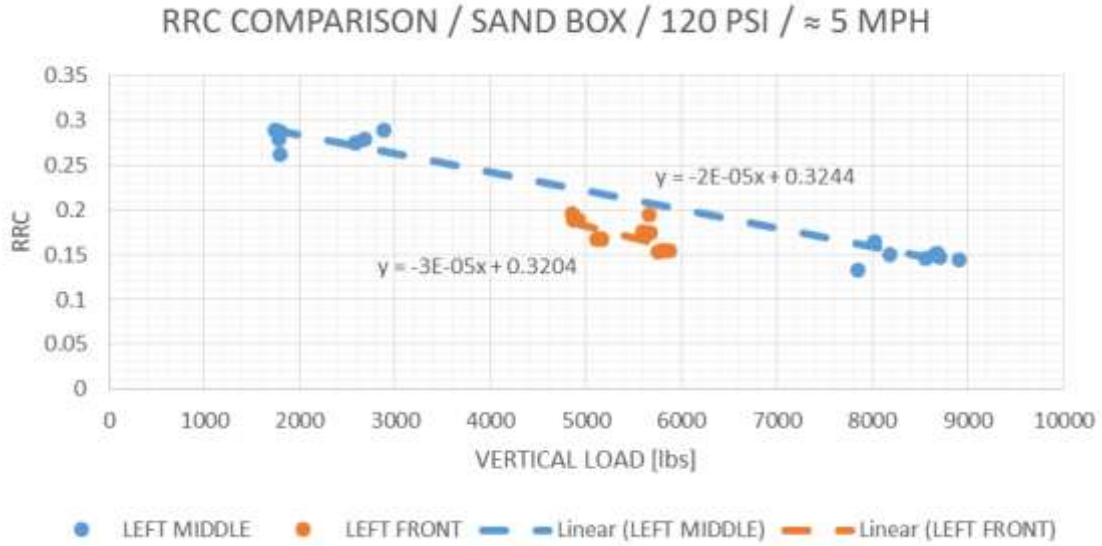


Figure 3-7 Rolling Resistance Results from Sandbox Experiments for Front and Pusher Axle

3.6 CONCLUSION FROM EXPERIMENTS

The experiments that were conducted at the Greensboro Proving Grounds provided the relevant information necessary for the FEA parameter-tuning optimization process. The physical experiments would be recreated in a virtual environment and the predicted results would be tuned to match the measured results from these tests. The average values between the left and the right tires on the pusher axle would be taken for the validation to negate the discrepancy between them. Future portions of this ongoing research project would utilize the soft soil data as well as the vertical excitation results.

CHAPTER 4: TIRE VALIDATION AND PARAMETER-TUNING OPTIMIZATION METHODOLOGY

This chapter focuses on the tuning of the material properties within the UOIT XONE XDA. Due to the lack of provided material data, and thus the material property approximations that resulted, it would not be possible to validate the tire model as it existed. Luckily, the physical tire had been used to capture various static and dynamic characteristics relating to vertical stiffness, lateral stiffness and rolling resistance coefficients. Using the known behaviour of the physical tire as individual objectives, it was decided to alter the unknown material properties until the known behaviour was properly replicated in the virtual environment. This led way to the parameter-tuning optimization approach. Each known experiment would be simulated and the difference between the simulated behaviour and the known behaviour would be recorded as percentage of error. All of the simulations would be coupled together, such that any material changes would be applied to all of the tire models simultaneously and the fitness of the tire model would be evaluated for all simulations. This would reduce the possibility of the optimization algorithm for unfairly optimizing one simulation more than another, and thus weight all of the simulations the same. While the process is fairly straightforward in theory, the procedure from algorithm concept to parameter tuned tire model was complex.

4.1 AVAILABLE DATA FOR PARAMETER-TUNING

Volvo Group North America donated specific performance information regarding the physical Michelin XONE XDA for validation purposes. This data included footprint sizing, total static vertical stiffness (k_{sv}), cornering stiffness (k_f), and lateral stiffness (k_l). In

addition, the data that was collected in Chapter 3 concerning the rolling resistance of the wide base tire was also available for the optimization process. While other data was collected at the Volvo Proving Grounds, only the steady state rolling resistance experiments on the rigid road were used as dynamic simulations in this process.

Table 4-1 Available Data for Parameter-Tuning Optimization

PARAMETER	SYMBOL
Total Static Vertical Stiffness	k_{sv}
Cornering Stiffness	k_f
Lateral Stiffness	k_l
RRC @ 8700 lbs	RRC1
RRC @ 9300 lbs	RRC2

4.2 SELECTION OF OPTIMIZATION ALGORITHM

Before the optimization procedure could be determined, a main algorithm had to be chosen. Every algorithm has its own distinct procedure and thus is more suitable for certain applications. Built into the PAM-OPT program are the following developed algorithms:

- Gradient
- ARSM
- Iterative Random
- Genetic
- Monte Carlo
- Discrete
- Stochastic

Due to the vast amount of available algorithms, a small experiment was designed to test three of the most suitable algorithms prior to scaling it up to the large optimization problem.

A simple FEA soil block was created in order to tune its material properties with the objective of matching compression displacement values. The reason this simulation was created was to replicate a pressure-sinkage experiment, which is commonly used to characterize soil samples. In reality, a soil specimen is placed within a large container such that the area is large enough that the container does not influence the soil in any way. A circular plate of known size is placed on top of the soil and a known pressure is applied to the top. This pressure plate is driven downward into the soil until a steady state condition is met. A visual of this FEA model simulation can be seen in [Figure 4-1](#). This is a procedure that was defined by Bekker in 1956 and was originally used to aid in off-road vehicle development. The pressure plate was made to be the same size as the contact area of the tire and the pressure was equal to the vertical load measured on the tire [22]. It is from this work that he was able to propose the following to predict the deflection in soils:

$$p = \left(\frac{k_c}{b} + k_\phi \right) z^n = k_{eq} z^n \quad 4-1$$

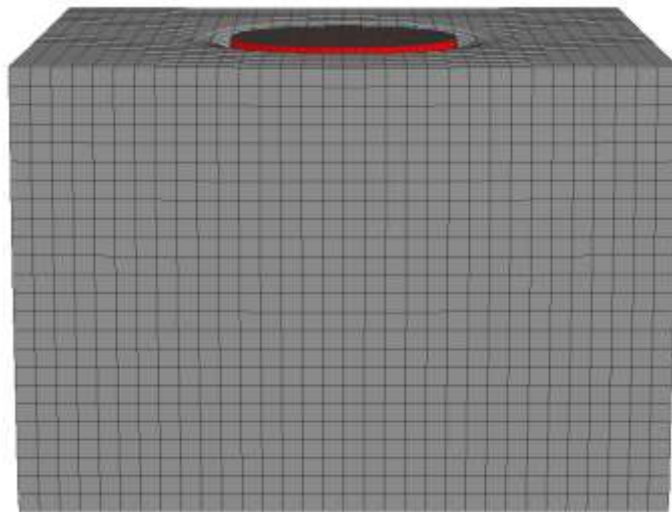


Figure 4-1 Visual From the Pressure-Sinkage Simulation

In Equation 4-1, p is the pressure, b is the radius of a circular plate or the smaller dimension of a rectangular plate, n , k_c and k_ϕ are pressure–sinkage parameters for the Bekker equation, $k_{eq} = k_c/b + k_\phi$, and z is sinkage.

Using this relationship, it was determined to model a Clayey Soil from Thailand due to the abundance of empirical data found in publications coupled with a relatively calm behaviour. By calm behaviour, that is its less than sporadic characteristics concerning pressure-sinkage relationships. For the calibration of the soil model, the following values were used within Table 4-2.

Table 4-2 Bekker Equation Parameters

PARAMETER	SELECTED VALUES
Applied Pressure	100 kPa
Plate Radius	0.15 m
K_c	16.03 kN/mn+1
K_ϕ	1262.53 kN/mn+2
n	0.7
Resultant Sinkage	23.7896 mm

With the simulation constructed, three of the most promising algorithms were chosen to compete in optimizing this soil model to match the predicted deflection of the pressure plate. For simulations that require large solving times, it is shown that algorithms that suit black box optimization are preferred [19]. For this purpose, the adaptive response surface methodology (ARSM) algorithm and the Monte Carlo algorithm were chosen for this analysis. In addition, the Genetic Algorithm (GA) was chosen to be the third competitor as

it is a widely used and general-purpose algorithm that had the possibility to outperform the ARSM and Monte Carlo.

For the purpose of parameter-tuning, two of the soil material parameters would be altered to achieve the desired soil deflection. It was decided that the soil density (ρ) and the Modulus of Elasticity (E) would be altered iteratively using the competing algorithms until a minimum deflection was found. The same search ranges were implemented across the algorithms to keep the search process the same. The algorithms would need to be evaluated and for this a few measurement criteria were recorded for each algorithm. The percentage error between the measured and simulated deflection and the number of function calls (NFC) to reach convergence were compared for each competing algorithm. It is from this small-scale optimization procedure that the following results were calculated:

Table 4-3 Results from the Pressure-Sinkage Algorithm Competition

ALGORITHM	ERROR (%)	CONVERGENCE (NFC)
Adaptive Response Surface Methodology (ARSM)	0.18%	24
Genetic Algorithm (GA)	0.66%	37
Monte Carlo	0.62%	< 50

The progression of the algorithms is also quite interesting to note. The way in which the solutions are generated effects the overall convergence and stopping criteria as well for each algorithm. Shown in [Figure 4-2](#) is how each of the algorithms conducted their search to find the minimum deflection error. It is worthwhile to note that the GA and ARSM were the only two algorithms to show a progression towards an optimum combination of

materials. The Monte Carlo algorithm can be characterized as a guess-and-test algorithm [19] and did not follow the same solution techniques to approach an optimum combination of materials. The algorithm that found the best solution, with a reasonable simulation time and exhibited ‘learning’ of the relationship between design parameters and the displacement was the Adaptive Response Surface Methodology (ARSM) algorithm. It is for these reasons that it was deemed the most suitable choice for the large-scale parameter-tuning algorithm.

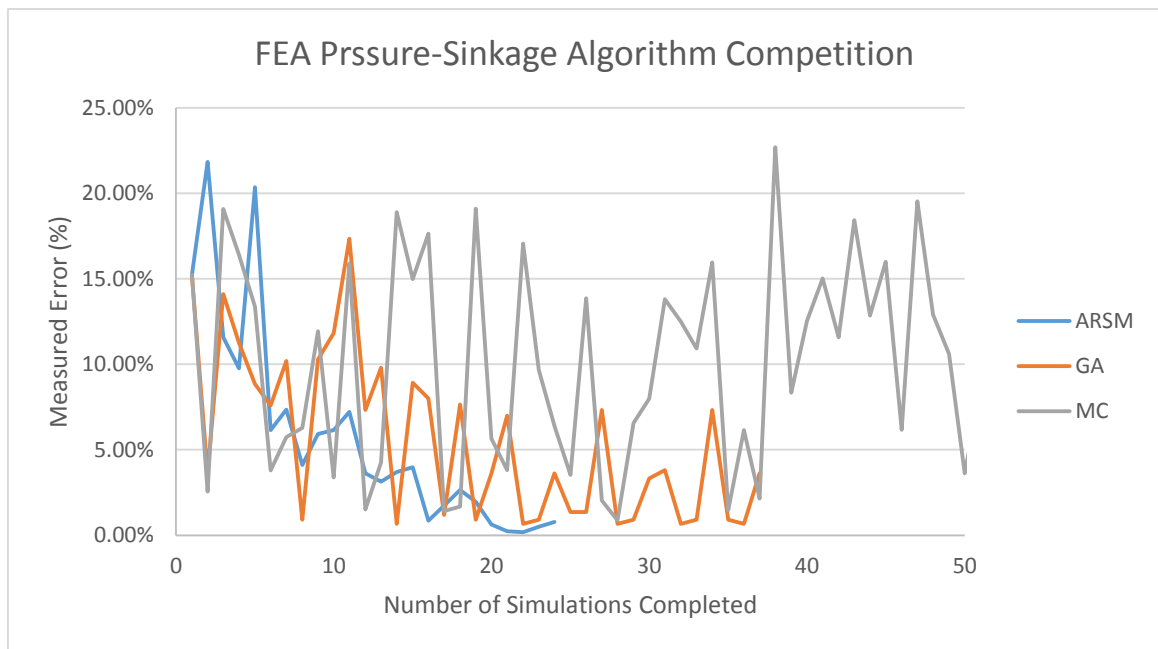


Figure 4-2 Progression of Competing Algorithms

4.3 COMBINED EXPERIMENTS PARAMETER-TUNING PROCEDURE

The procedure that was used in the previous chapter was then scaled up to handle a much more complex optimization procedure. It was determined that the full parameter-tuning optimization script should incorporate as much of the physical data that was acquired in order to make it as valid as possible. This data would include both static and dynamic

simulations in order to prove the tire model was acceptable for all scenarios. To do so, a vertical stiffness simulation, a lateral stiffness simulation, and two rolling resistance simulations were created to implement this parameter-tuning optimization script. All four simulations would be run in series with the same material properties within the tire models. The simulations would then be evaluated on their measurement criteria, and a new set of material properties would be applied to all models. The general procedure would continue until the error between the simulated behaviour and the measured behaviour was minimized. The Adaptive Response Surface Methodology (ARSM) would be used to learn the landscape of the optimization problem and iteratively minimize the error across all simulations.

The total static vertical stiffness (k_{sv}) of the tire model describes the ratio of applied vertical force to the measured vertical deflection it induces on a rigid road. The physical model was found to have a total vertical stiffness of 1280 kN/m when inflated to 120 PSI. This experiment was recreated in using PAM-CRASH in order to recreate the scenario. In order to simplify the model, a ramped vertical force of 50 kN was applied to the tire and thus predict a deflection of 39.0625 mm. The optimization script would record the percentage error between the simulated deflection and the measured deflection and attempt to minimize the difference.

The lateral stiffness (k_l) of the tire model describes the ratio of applied lateral force to the measured lateral deflection it induces. Similar to the above simulation, the tire model would be inflated to 120 PSI and then experience a rated load of 4625 kg applied vertically. The tire model then experiences a lateral force which causes it to deflect. From the physical measurements, it was found that the lateral stiffness of the Michelin XONE XDA was

450.4639 kN/m. In the simulation, a known applied load of 5 kN was used and thus should result in a lateral deflection of 11.0997 mm. Again, the optimization script would record the percentage error between the simulated deflection and the measured deflection and attempt to minimize the difference. A screenshot from both of the static simulations (total vertical stiffness (k_{tot}) and lateral stiffness (k_l) can be seen in [Figure 4-3](#).

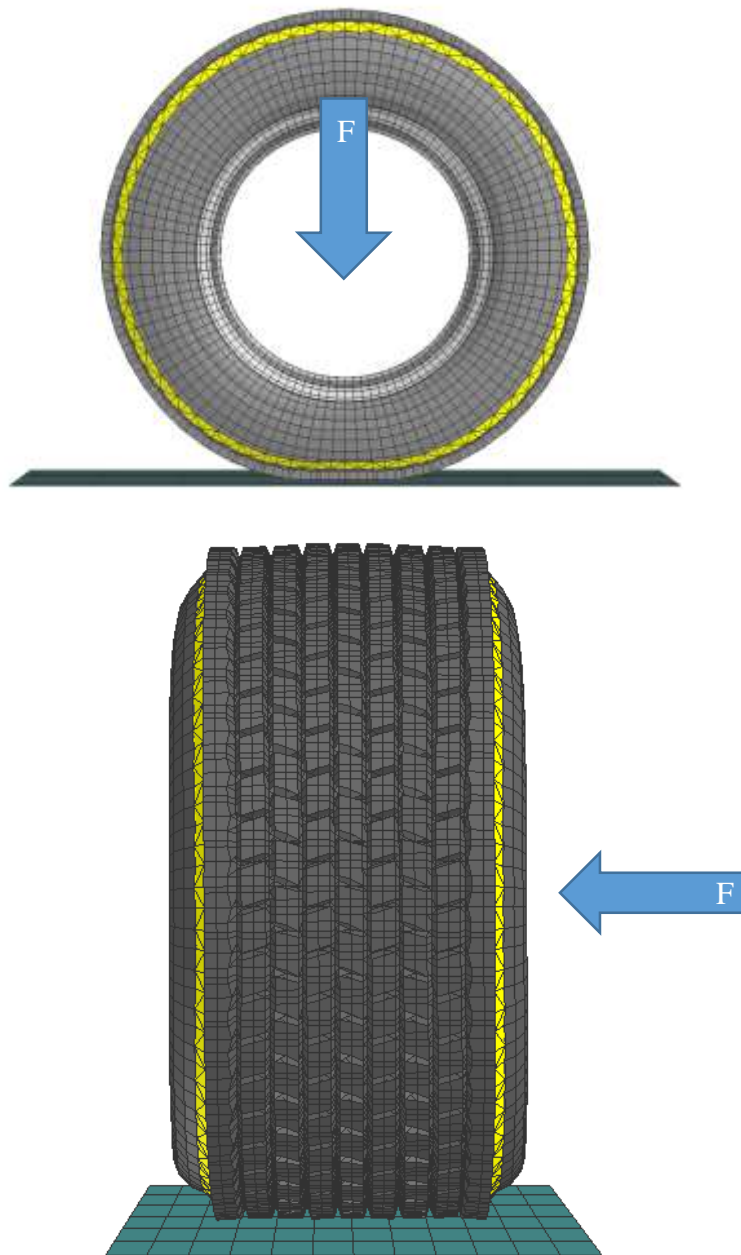


Figure 4-3 Visual of the Total Static Vertical Stiffness and Lateral Stiffness Simulations

The dynamic rolling resistance simulations were created in an effort to use the data acquired from the experimental tests completed at the Greensboro Proving Grounds to tune the material parameters. The average rolling resistance trend, recorded in [Figure 3-5](#), was used to predict the RRC at two vertical loads. The simulations were designed to drag the tire model along a rigid road and record the longitudinal force (F_x). This way, there would be no longitudinal force contributed from the driving torque and would isolate for the rolling resistance force. It was found that the rolling resistance for a vertical load of 8700 lbs (38.7 kN) should be 1529.39 N and the rolling resistance for a vertical load of 9300 lbs (41.4 kN) should be 1701.11 N. The optimization script would record the percent error between the simulated longitudinal forces and the measured forces and attempt to minimize the difference as well. A visual of this simulation can be seen in [Figure 4-4](#).

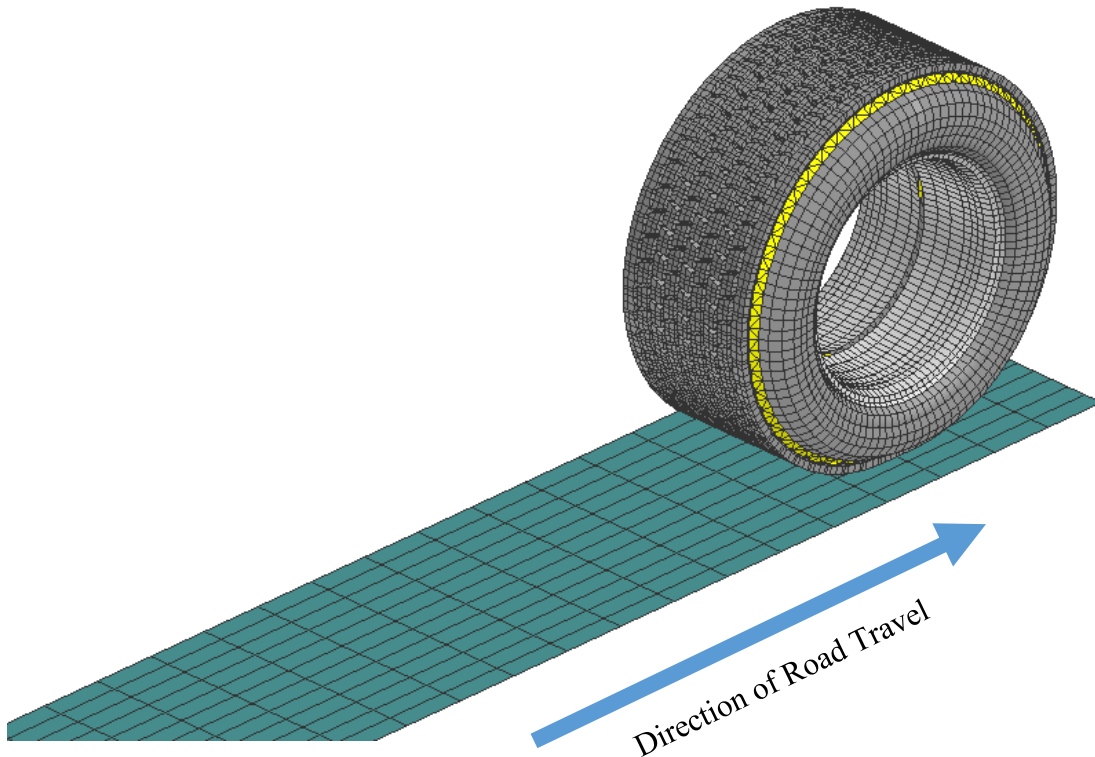


Figure 4-4 Visual for the Determination of Rolling Resistance Force of the Tire Model

The combined procedure for the parameter-tuning script is shown in [Figure 4-5](#). In these four simulations, a total of 15 parts had their material properties edited in order to match the predicted behaviour of the tire model. In these parts, the modulus of elasticity (E) was changed iteratively within all of the sidewall parts and the undertread membrane as well. All 15 parts would have the properties changed within all tire models for every iteration that was conducted. The percent error for all simulations were added together to find the total error for that iteration. It was the total error that was to be minimized and thus became the optimization objective function. It is from this process that a solution was eventually found.

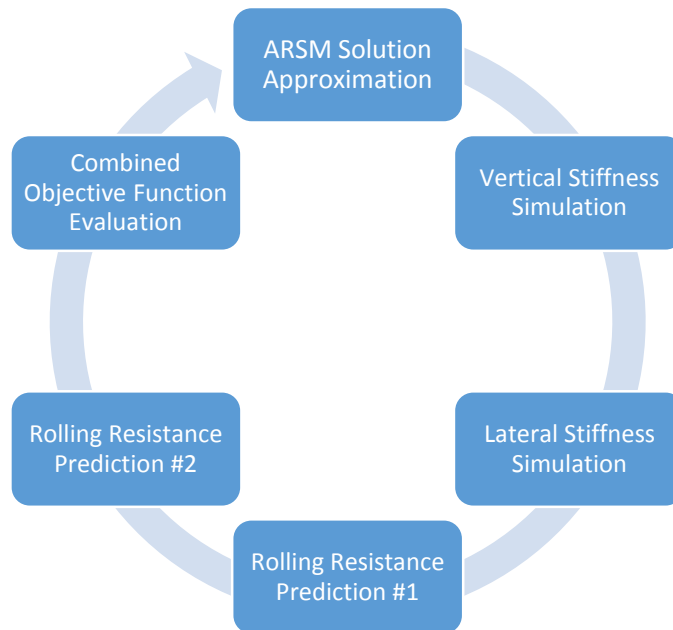


Figure 4-5 ARSM Parameter-Tuning Procedure

4.4 RESULTS OF PARAMETER-TUNING OPTIMIZATION

The parameter-tuning optimization script ran for a total of 45 iterations in which the vertical stiffness, lateral stiffness, and both rolling resistance simulations were evaluated. Material

properties were edited within the sidewall and undertread membrane until a minimum total error was achieved. The progression of the combined parameter-tuning procedure can be seen in [Figure 4-6](#).

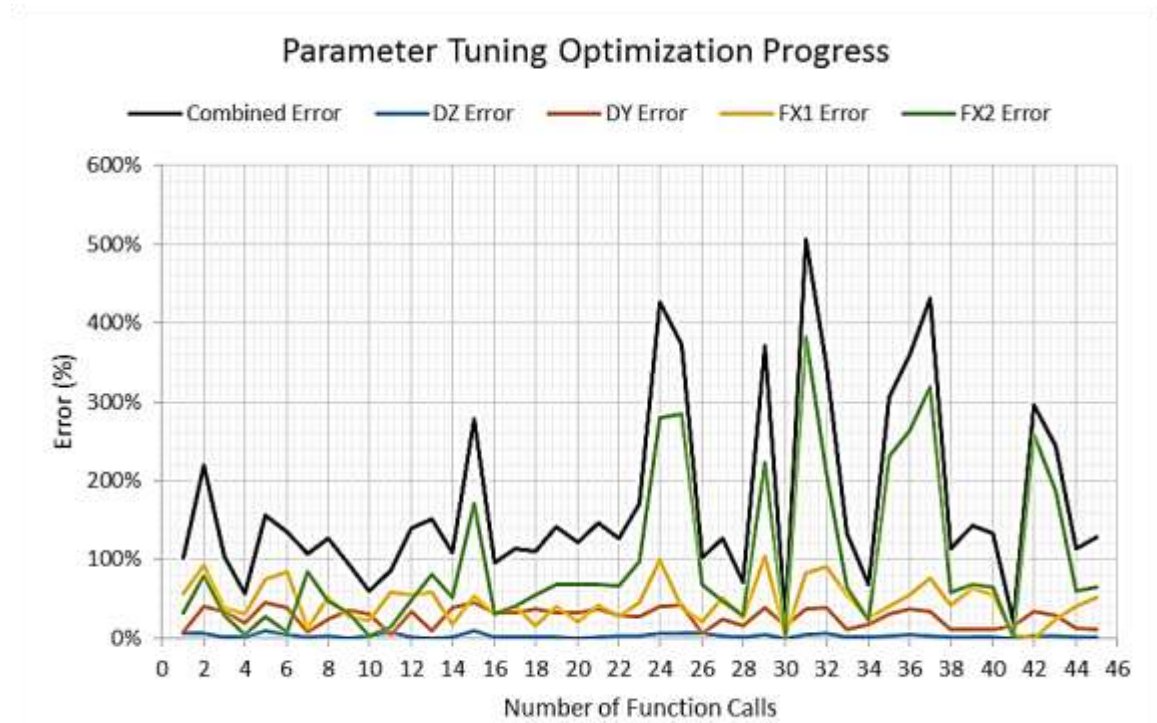


Figure 4-6 Results from Combined Parameter-Tuning Algorithm

It can be shown that the rolling resistance simulations proved to be the most sensitive to the change in material properties. For slight changes in the design parameters, the error could increase to as high as 381.78% in one simulation, shown at iteration 31. Regardless, through the progression of the algorithm, the optimization script eventually came to a minimum total error at iteration 41, summarized in [Table 4-4](#).

Table 4-4 Optimum Results from ARSM Algorithm

PARAMETER	SYMBOL	MEASURED	SIMULATED	ERROR
Vertical Deflection	DZ	39.06 mm	39.23 mm	0.42%
Lateral Deflection	DY	11.10 mm	9.41 mm	15.22%
Rolling Resistance 1	FX1	1529.39 N	1466 N	4.14%
Rolling Resistance 2	FX2	1701.11 N	1737.35 N	1.78%

Based on the results of the optimization process, it was found that the total error was able to be reduced to a minimum value of 21.56%. The highest source of error was from the lateral stiffness simulation, which showed error of 15.22%. In reality, the deflection of the tire model in this simulation was inaccurate by 1.69 mm, which is relatively small. The difference in deflection could simply be attributed to the physical measurement that was taken of the tire and not necessarily be the result of a poor simulation. Regardless, these error values were deemed acceptable and the corresponding material properties were implemented into the validated UOIT XONE XDA tire model.

CHAPTER 5: POPULATION OF THE IN-PLANE RIGID RING TIRE MODEL PARAMETERS

This chapter will outline the procedure that was taken to properly populate the analytical rigid ring model. The rigid ring models were constructed to prove the further use of the FEA tire model that was constructed and validated. The FEA model could be used in various simulations to isolate for the in-plane rigid ring parameters that could then be used in conjunction with the full FEA model for quick and robust research. There are many parameters to isolate for, and thus there exist multiple virtual experiments to conduct in order to calculate the in-plane and out-of-plane rigid ring parameters. It was desired to construct multiple rigid ring models as well. The models were constructed with varying vertical loads and inflation pressures in order to understand the effect these parameters have on the overall performance of the FEA tire model. The FEA tire model was simulated with vertical loads of 2312.5 kg, the rated load of 4625 kg, and 6937.5 kg. This was done to gather trends related to vertical loads of 50%, 100%, and 125% of the rated loads for this physical tire. The models were also simulated with varying inflation pressure, in which pressures of 70 PSI, the rated inflation pressure of 120 PSI, and 150 PSI were used. This was again done to gather trends related to the different internal pressures of the physical tire.

5.1 DESIRED IN-PLANE RIGID RING PARAMETERS

In order to populate the in-plane rigid ring model, it was deemed necessary to isolate for the following parameters contained in [Table 5-1](#). Through a series of carefully created

virtual experiments, the in-plane parameters were calculated in order to populate the analytical rigid ring model.

Table 5-1 Required In-Plane Rigid Ring Parameters

PARAMETER	SYMBOL
Contact Patch Width	w
Contact Patch Length	a
Total Static Vertical Stiffness	k_{sv}
Total Dynamic Vertical Stiffness	k_{dv}
Total Vertical Damping Constant	C_{tot}
Rotational Stiffness	$k_{b\theta}$
Rotational Damping Constant	$C_{b\theta}$
Longitudinal Tread Stiffness	k_{cx}
Longitudinal Tire Stiffness	k_k

5.2 STATIC FOOTPRINT LENGTH AND WIDTH (a , w)

One of the easiest aspects of the tire model to validate should be the footprint that it will exert on the road surface under specific load and inflation pressure conditions. This measurement is necessary as the tire vertical deflection can be within an acceptable range, however the shape and overall area that it will be expected to exert can still differ. In order to calculate the contact patch dimensions, the physical tire is commonly inflated to its rated

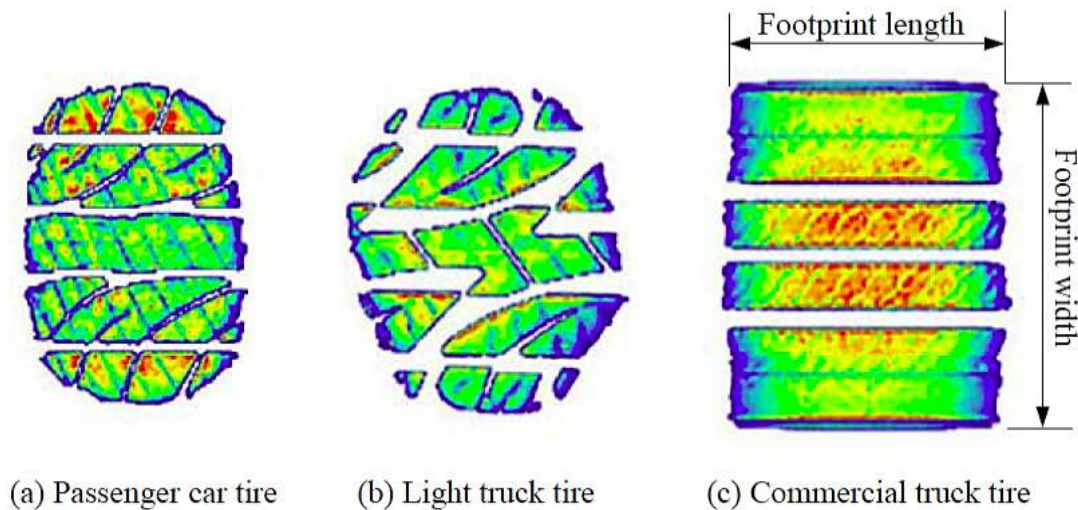


Figure 5-1 Typical Footprint Shapes of Various Types of Pneumatic Tires [9]

inflation pressure and loaded, either physically on the vehicle of choice or artificially in a laboratory setting. From this neutral position, it is either loaded against carbon paper, against pressure sensitive paper, or more accurately over a glass window and photographed from below [10]. The static contact footprint can vary drastically depending on the type of tire and for what specific application it has been developed for. The shape in which the contact patch takes can dramatically affect the performance of the tire. Various contact patch dimensions are shown in [Figure 5-1](#).

Information was provided as to the footprint length and width of the Michelin XONE XDA 445/50R22.5 tire. These values were calculated at the tire’s rated load of 4625 kg and rated inflation pressure of 120 psi. At these specific conditions, the physical tire displayed the measurements shown in [Table 5-2](#).

Table 5-2 Measurements of the Michelin XONE XDA Under Rated Load and Inflation Pressure

PARAMETER	SYMBOL	VALUE	UNITS
Contact Patch Width	w	379.32	mm
Contact Patch Length	a	200.12	mm

This experiment was replicated in the virtual environment in order to verify the FEA tire model under similar conditions. For the virtual experiment, the tire model is inflated and allowed to settle on a rigid road before being loaded to the specified vertical load. The contact patch is then measured. A compressed XONE XDA viewed from the bottom under rated vertical load and inflation pressure can be seen in [Figure 5-2](#). All specified vertical loads and inflation pressures were also simulated in order to gather the measurements of the contact patch change in width and length, which can be seen in

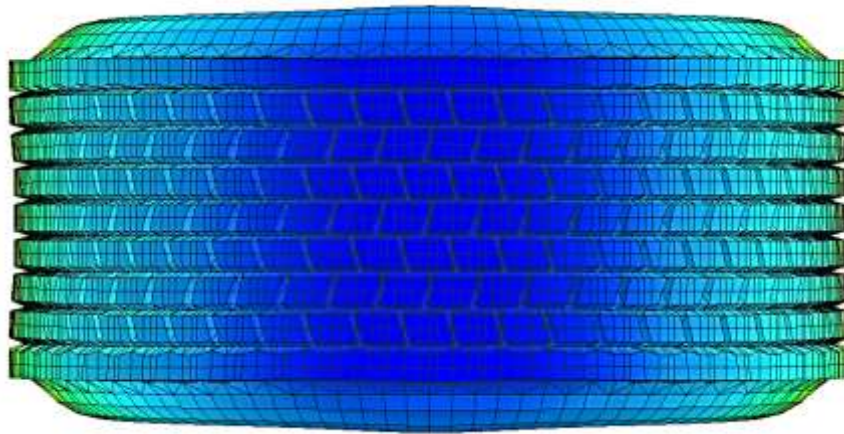


Figure 5-2 Footprint Dimensions Recorded at a Vertical Load of 4625 kg and Inflation Pressure of 120 PSI

Table 5-3.

Table 5-3 Results from Static Footprint Simulations

PARAMETER	LOAD [KG]	70 PSI	120 PSI	150 PSI	UNITS
Contact Patch Width (w)	2312.5	392.75	399.14	401.79	mm
	4625	393.56	399.19	401.80	
	6937.5	393.99	399.63	402.40	
Contact Patch Length (a)	2312.5	244.27	172.90	150.77	mm
	4625	272.66	198.75	186.14	
	6937.5	369.11	280.46	258.90	

As it can be seen from

Table 5-3, the simulation results show good correspondence to the measurements taken from the physical tire. In addition, the contact patch grows with increased vertical load and decreased inflation pressure, which was expected.

5.3 TOTAL STATIC VERTICAL STIFFNESS (K_{sv})

The in-plane total static vertical stiffness is a desired parameter as it describes the amount the tire model will deflect from a known applied vertical force. In order to isolate for this parameter a simulation is designed in which the tire model is quickly inflated to the required inflation pressure and lowered onto a rigid road. A force is then applied to the center of gravity (COG) of the rigid rim in a ramped fashion from 0 to 60000 N. As the force steadily increases, the tire model should depress accordingly. A visual of the experiment can be seen in [Figure 5-3](#).

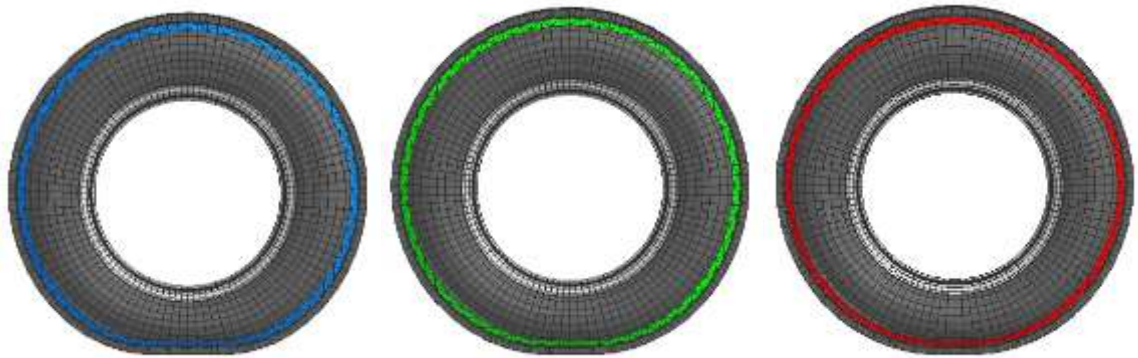


Figure 5-3 Visual from the Total Vertical Stiffness Simulation, Shown Fully Depressed from a Load of 60 kN.

These rigid ring simulations were all designed to run three tires simultaneously. This was done to reduce the computational intensity as well as the overall storage space required. The three tires feature varying inflation pressures and, for reference, the blue, green and red tire shoulders represent the lowest, rated and highest inflation pressures respectively. For all of the featured virtual experiments, the models are rapidly inflated to the specified inflation pressures and then lowered into their starting positions. Depending on the required simulation, this starting position can change, however all tire models are given sufficient time to dissipate the energy from inflation before beginning the simulation.

After the tire models fully deflect from the slow and ramped vertical load, a plot is then made of the z-displacement from the rim COG against the known applied load. The total static vertical stiffness (k_{sv}) can then be found as the slope of the load vs. deflection curve. The deflection results from the 4625 kg case at all required inflation pressures can be seen in [Figure 5-4](#).

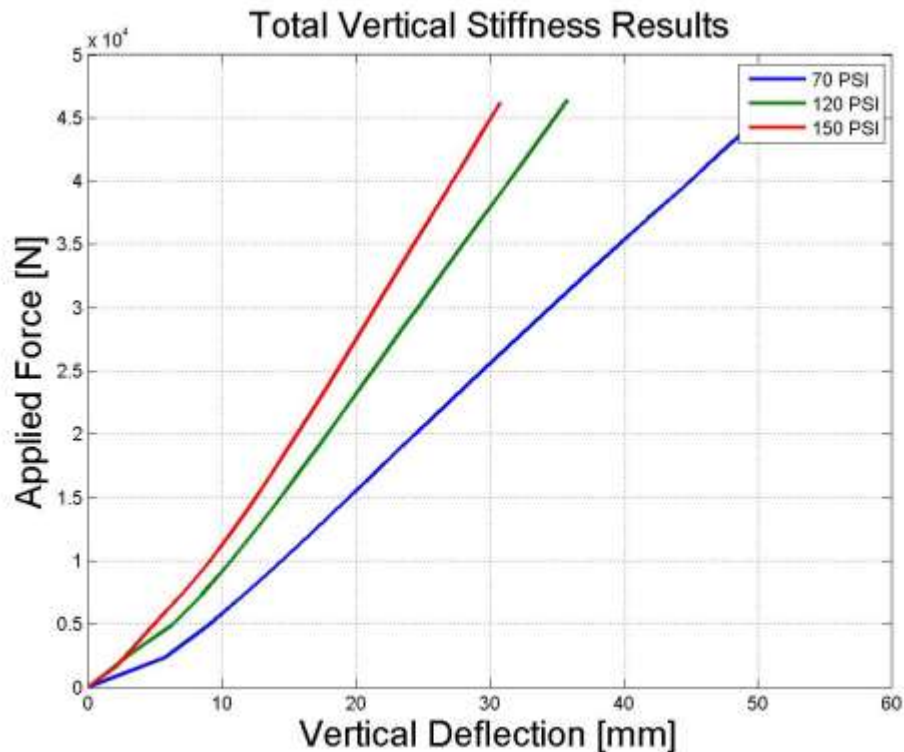


Figure 5-4 Results from the Total Vertical Stiffness (k_{sv}) Simulation

It can be shown that the underinflated tire model experienced the highest deflection from the applied load. This trend was expected, as with increased inflation pressure the tire model should be more rigid and thus have an increase in vertical stiffness. The total static vertical stiffness is found as the ratio of deflection to applied load, or as outlined in [Equation 5-1](#). The results are shown in [Table 5-4](#)

$$k_{sv} = \frac{\text{Applied Vertical Load}}{\text{Measured Deflection}} \tag{5-1}$$

Table 5-4 Calculated Parameters for the Total Static Vertical Stiffness (k_{sv})

PARAMETER	70 PSI	120 PSI	150 PSI	UNITS
Total Static Vertical Stiffness (k_{sv})	952.3	1362.8	1558.8	N/mm

5.4 TOTAL DYNAMIC VERTICAL STIFFNESS (k_{dv})

The total dynamic vertical stiffness (k_{dv}) of the tire model is composed of two parts, the dynamic sidewall stiffness and the dynamic residual or tread stiffness. This in-plane rigid ring parameter describes the vertical stiffness of the tire model during operation, not just under static loading cases. In order to isolate for the total dynamic stiffness of the tire model, a dynamic simulation is conducted in which the tire model rotates on a rigid drum and eventually encounters a rounded cleat. The objective of this cleat is to excite the tire model in a purely vertical orientation. In order to achieve this, the tire model begins the simulation by being lowered onto a 2.5m diameter rigid drum and being allowed to settle. From the starting position, the rigid rim's COG is then locked in the z-axis so that it will not be able to bounce from the cleat excitation. The drum then begins to rotate and simulates a longitudinal velocity of 50 km/h. When the tire model encounters the 20cm diameter cleat, the energy is transferred into the tire sidewall and tread components and causes significant deflection. This experiment is commonly referred to as a 'drum-cleat' test and is commonly used to understand how the force of cleat excitation causes deflection in the tire components. A visual from this virtual experiment can be seen in [Figure 5-5](#).

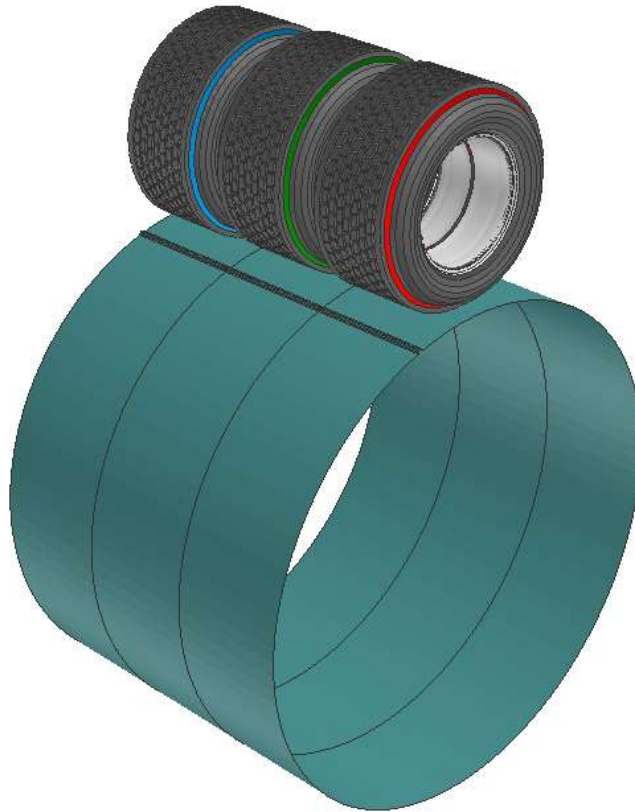


Figure 5-5 Visual from the Total Dynamic Vertical Stiffness (k_{dv}) Simulation

Unfortunately, the procedure from the simulation results to the calculated total dynamic vertical stiffness solution is not as simple to determine as previous parameters. The force the cleat will exert on the tire model is registered as a vertical section force, which causes the tire model to resonate vertically as well as horizontally. The internal stiffness and damping properties of the tire model have the ability to shift the undamped natural frequency (ω) at which these modes of vibration occur [1]. Thus, if the undamped natural frequency of the vibration (ω) can be isolated for, the tire model's total dynamic vertical stiffness (k_{dv}) can be calculated. The natural frequency is then the important characteristic for this particular experiment.

In order to obtain the natural frequency of the tire model (ω), the section force recordings from the drum-cleat experiment are transposed from the time domain to the frequency domain by passing the recorded data through a Fast Fourier Transformation (FFT) algorithm. This produces a relationship between the measured section forces with respect to the in-plane first mode of natural frequency (f). The first mode of frequency will correspond to the largest recorded vertical section force, and this relationship can be observed in [Figure 5-6](#). The data that is presented is recorded from the rated load simulation, in which a vertical load of 4625 kg is simulated.

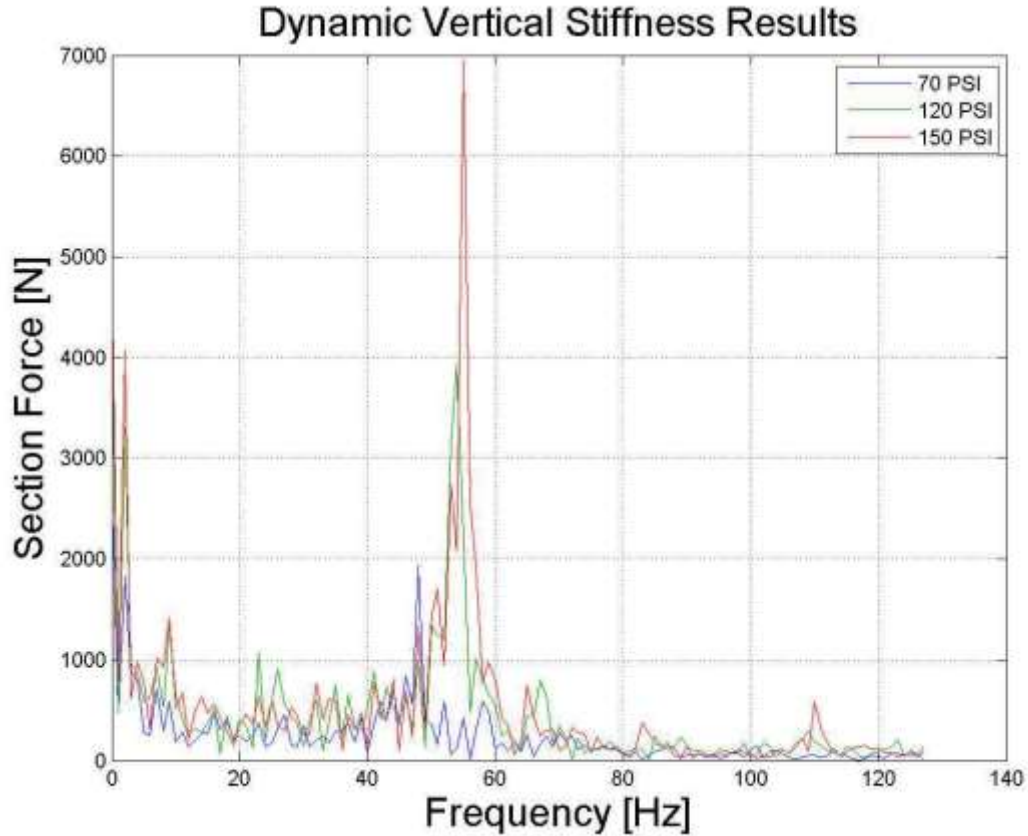


Figure 5-6 Results from the Total Dynamic Vertical Stiffness (k_{dv}) Simulation

As stated earlier, the frequency which results in the largest spike of the vertical section force reveals the tire model's first mode frequency of in-plane vibration (f). By using the following mathematical procedure (Equations 5-2 to 5-5), as outlined by Chae *et al.* in 2006, the first mode frequency of in-plane vibration can be used to find the total dynamic vertical stiffness (k_{dv}) by solving for the undamped natural frequency (ω) first.

$$\omega = \sqrt{k_{dv}/m_b} \quad 5-2$$

$$\omega = 2 \times \pi \times f \quad 5-3$$

$$\therefore 2\pi f = \sqrt{k_{dv}/m_b} \quad 5-4$$

$$k_{dv} = (2\pi f)^2 \times m_b \quad 5-5$$

Where m_b is the mass of the tire belt (80.08 kg)

By using the above relationships, the results from the 2312.5 kg, 4626 kg, and 6937.5 kg simulations can be utilized to solve for the total dynamic vertical stiffness (k_{dv}), as shown in Table 5-5.

Table 5-5 Calculated Parameters for the Total Dynamic Vertical Stiffness

PARAMETER	LOAD [KG]	70 PSI	120 PSI	150 PSI	UNITS
First Mode Frequency of In-Plane Vibration (f)	2312.5	47	53	55	Hz
	4625.0	48	54	55	
	6937.5	48	54	55	
Undamped Natural Frequency (ω)	2312.5	295.31	333.01	345.58	rad/s
	4625.0	301.59	339.29	345.58	
	6937.5	301.59	339.29	345.58	
Total Dynamic Vertical Stiffness (k_{dv})	2312.5	6170.4	7846.3	8449.7	N/mm
	4625.0	6435.7	8145.2	8449.7	
	6937.5	6435.7	8145.2	8449.7	

Due to the lack of increased resolution from the FFT, it can be seen in Table 5-5 that the first mode frequency (f) is repeated across some vertical loads. It is from this lack of resolution that results in similar total dynamic vertical stiffness (k_{dv}) calculations. For improved results, the resolution of the FFT should be increased to show more variation in the calculated results.

5.5 TOTAL VERTICAL DAMPING CONSTANT (C_{tot})

The total vertical damping constant (C_{tot}) is a parameter which describes the tire model's ability to dissipate energy from an excited system. This in-plane rigid ring parameter is isolated by performing a 'drop test', which is a relatively simple procedure. The tire, or tire model in this case, is held roughly 20 mm above a rigid road and rapidly inflated to the desired inflation pressure. The required vertical load is also applied while in this neutral position and all energy is allowed to dissipate from the model from the initialization. The tire model is then released and constrained to only move in the z-axis. This ensures it is a linear and single degree of freedom system of vibration. Due to the vertical load applied to the rigid rim's COG, as well as the acceleration due to gravity, the tire model will travel towards the rigid road, make contact, and rebound upward. This bouncing continues until the energy is damped out of the excited system. A visual from this virtual experiment at the rated load of 4625 kg can be seen in [Figure 5-7](#), in which the tire models have all reached their lowest amplitude after the initial release.

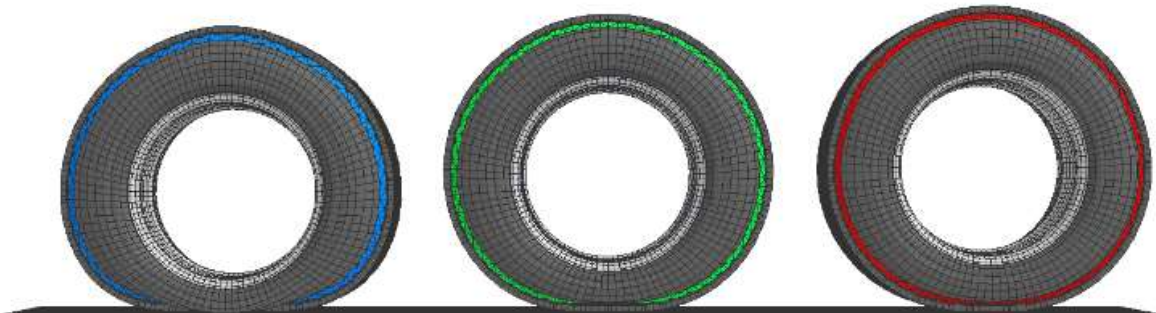


Figure 5-7 Visual of the Total Vertical Damping Constant (C_{tot}) Simulation

For this experiment, the COG of the rigid rim is recorded in order to capture the variation in rebound amplitudes. As energy is damped out of the excited system, the amplitudes

should decay with time. The decay should follow a trend of free-damped vibration in a single degree of freedom underdamped mechanical system. The virtual experiment, in which a vertical load of 4625 kg is applied, has a visual shown in [Figure 5-8](#).

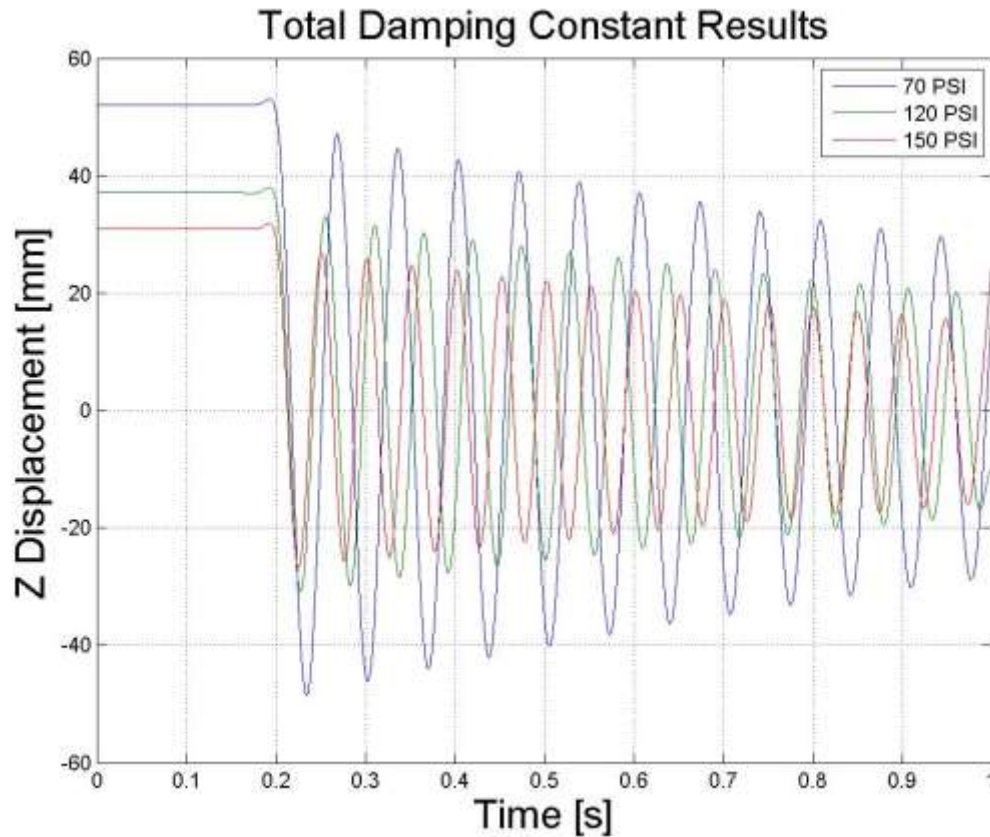


Figure 5-8 Results from the Total Vertical Damping Constant (C_{tot}) Simulation

Using this data from above, certain principles of mechanical vibration can be applied to isolate for the total vertical damping constant of the system. By using the difference in the initial amplitude (y_1) and the successive amplitude (y_2), the logarithmic decrement (δ) can be calculated by using [Equation 5-6](#). In addition, [Equations 5-7 to 5-8](#) are used to finally isolate for the total vertical damping constant (C_{tot}) of the tire models.

$$\delta = \ln \frac{y_1}{y_2} \quad 5-6$$

$$\xi_{tot} = \frac{\delta}{\sqrt{4\pi^2 - \delta^2}} \quad 5-7$$

$$C_{tot} = 2\xi_{tot}\sqrt{m_{tot}k_{tot}} \quad 5-8$$

The total mass of the tire model including the rim (m_{tot}) was 111.253 kg

Using the amplitude differences for all of the simulations, at vertical loads of 2312.5 kg, 4625 kg, and 6937.5 kg, the procedure outlined above was able to populate the parameters found in [Table 5-6](#).

Table 5-6 Calculated Parameters for the Total Vertical Damping Constant (C_{tot})

PARAMETER	LOAD [KG]	70 PSI	120 PSI	150 PSI	UNITS
Total Vertical	2312.5	0.086	0.079	0.056	kN-s/m
Damping Constant	4625.0	0.083	0.075	0.070	
(C_{tot})	6937.5	0.089	0.080	0.064	

The results shown in [Table 5-6](#) show less than ideal values for the total vertical damping constant. Although the expected trends with respect to inflation pressure are evident, the expected trends with respect to the change in vertical load did not appear. At this time, it is believed that the mass of the rigid rim in these simulations is influencing the damping properties negatively, and that its inertia is simply skewing the displacement data. Further work is required to properly isolate for the total damping constant and to achieve ideal trends.

5.6 ROTATIONAL STIFFNESS AND DAMPING CONSTANT OF THE SIDEWALL ($k_{b\theta}$, $C_{b\theta}$)

The in-plane rotational stiffness of the sidewall will describe how the tire model is able to resist rotation from a known force applied to the sidewall. In order to isolate for the stiffness of the sidewall, a static and isolated virtual experiment is conducted. The simulation consists of rapidly inflating the tire while the rigid rim is locked in all axis while suspended in space. At no time is the tire model interacting with a rigid road in this case. An arbitrary load of 15 kN is applied to the tread and under-tread layer, which is made a rigid body in order to negate the rotational interaction from any other component of the tire model other than the sidewall. When the ramped load is applied to the rigid tread, tire model sidewall will rotate while the rim remains in its neutral position. The force is held constant until steady state rotation is reached, and its steady state rotational displacement (Θ_{ss}) is recorded. The rotational stiffness of the sidewall ($k_{b\theta}$) is then found using [Equation 5-9](#). A visual from this virtual experiment can be seen in [Figure 5-9](#).

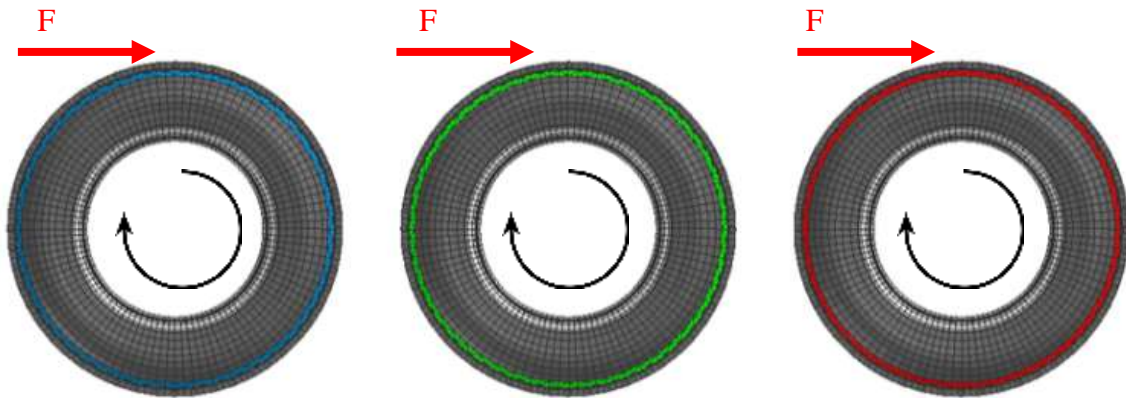


Figure 5-9 Visual of the Rotational Stiffness and Damping Constant of the Sidewall Simulation ($k_{b\theta}$, $C_{b\theta}$)

$$k_{b\theta} = \frac{\text{Applied Force} \times \text{Distance to Rim COG}}{\theta_{ss}}$$

5-9

Upon reaching steady state, the ramped load is released. The removal of this force causes the sidewall to rotate back towards its neutral position, after which it will oscillate back and forth until the energy of the system is dissipated. The rotational displacement of the tire model is recorded in order to capture the amplitudes of each successive rotation to eventually isolate for the in-plane rotational damping constant ($C_{b\theta}$). A recording of the rotational displacement of the tire models, which in this case do not depend on the vehicle vertical load, can be found in [Figure 5-10](#).

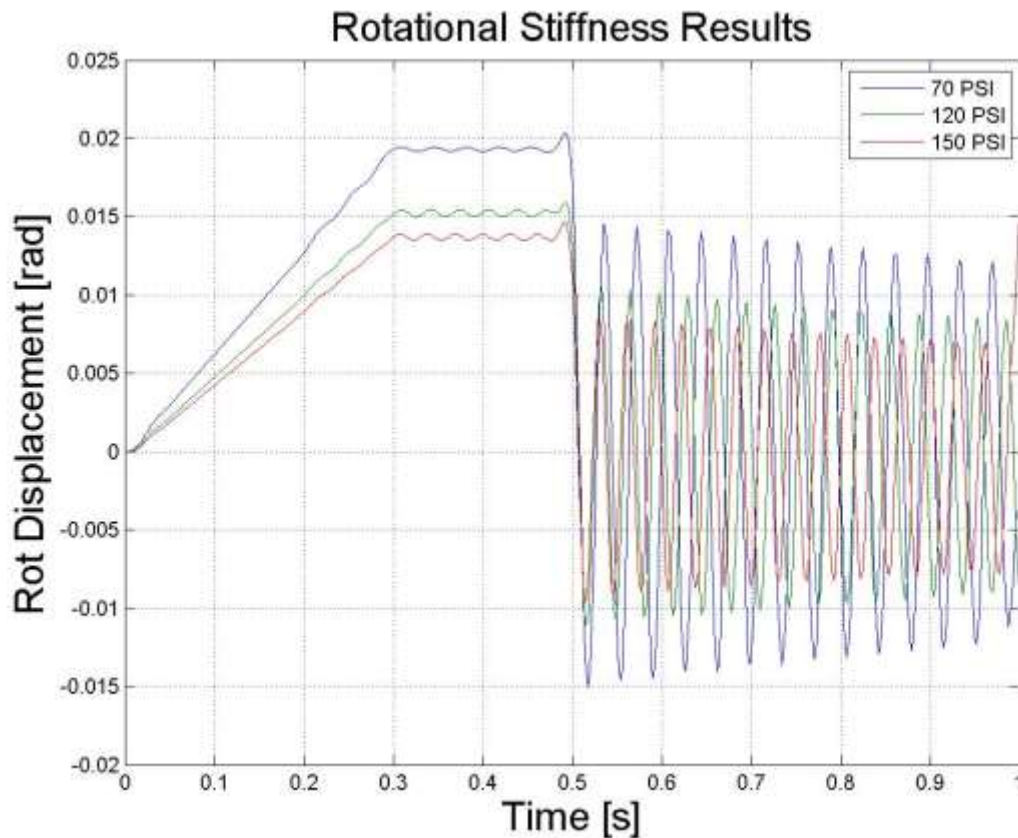


Figure 5-10 Results from the Rotational Stiffness and Damping ($k_{b\theta}$, $C_{b\theta}$) Simulation

By analyzing the data captured during this virtual experiment, it can be seen that the energy of the system is dampened out with each successive oscillation. The first two amplitudes of rotation (Θ_1 and Θ_2) are recorded in addition to the times between these amplitudes (t_1 and t_2). Similar to previous rigid ring parameter calculations, the logarithmic decrement (δ) and sidewall damping ratio (ξ) can be calculated. Taking into account the time between amplitudes, the undamped (ω_{nr}) and damped (ω_{dr}) periods of vibration can be found to allow the critical damping constant (C_c) to also be calculated. Lastly, the critical damping constant (C_c) can be used to solve for the rotational damping constant of the sidewall ($C_{b\theta}$). This procedure is outlined in Equations 5-10 to 5-16.

$$\delta = \ln\left(\frac{\theta_1}{\theta_2}\right) \quad 5-10$$

$$\xi = \frac{\delta}{\sqrt{4\pi^2 - \delta^2}} \quad 5-11$$

$$\tau_d = t_2 - t_1 \quad 5-12$$

$$\omega_{nr} = \frac{2\pi}{\tau_d \sqrt{1 - \xi_{bz}^2}} \quad 5-13$$

$$\omega_{dr} = \frac{2\pi}{\tau_d} \quad 5-14$$

$$C_c = 2 \times I_{by} \times \omega_{nr} \quad 5-15$$

Where I_{by} is the moment of inertia of the tire belt, 17.4026 kg-m²

$$C_{b\theta} = \xi \times C_c \quad 5-16$$

Using the procedures outlined above, the angular displacement data for all desired inflation pressures can be processed and used to solve for the rotational stiffness and damping constant of the sidewall ($k_{b\theta}$, $C_{b\theta}$) and is shown in Table 5-7.

Table 5-7 Calculated Parameters for the Rotational Stiffness and Damping Constant ($k_{b\theta}$, $C_{b\theta}$)

PARAMETER	70 PSI	120 PSI	150 PSI	UNITS
Rotational Stiffness of the Sidewall ($k_{b\theta}$)	404.44	514.88	574.12	kN-m/rad
Rotational Damping Constant of the Sidewall ($C_{b\theta}$)	0.005	0.019	0.033	kN-m-s/rad

5.7 LONGITUDINAL TREAD AND TIRE STIFFNESS (k_{cx} , k_k)

One of the most important parameters, the longitudinal tread and tire stiffness, will characterize how the tire model is able to generate longitudinal forces from a stationary position. The amount of recorded slip between the tire tread and the road surface will determine the amount of longitudinal force that can be generated. In order to isolate for these tire model properties, a virtual experiment is conducted in which the tire model undergoes a period a rapid acceleration from a stationary and neutral position on a rigid road. In this simulation, the rigid road is in fact a rigid drum that is 3.4 m in diameter and rotates from the longitudinal force developed from the tire model. The tire model (vertically loaded) drives the drum and the difference in angular velocities is used to calculate the slip percentage of the accelerating tire model. There is an initial lag in the angular velocity due to the inertia of the drum, which results in the slip between the tire and drum. A visual for this virtual experiment can be seen in [Figure 5-11](#), in which the wireframe tire model begins in a neutral position (Left) and then experiences the initial rapid acceleration (Right). There is noticeable deformation within the tread and sidewall, in which the initial tire slippage is attributed to.

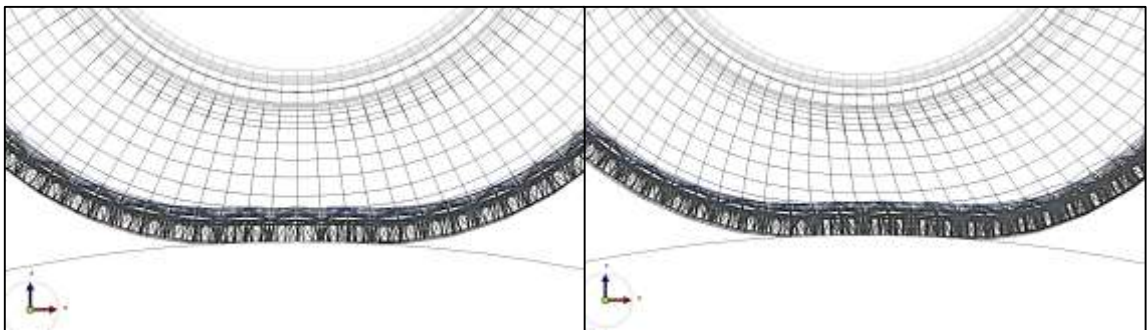


Figure 5-11 Visual of the Longitudinal Tread and Tire Stiffness (k_{cx} , k_k) Simulation

From the simulation, the rotational velocities of the tire model and drum are recorded to capture the delay in the drum model to match the driving angular velocity of the tire model. A plot of the developed longitudinal force (F_x) and the corresponding slip percentage is created, and the slope of the linear portion of this plot (0-10% slip) will reveal the longitudinal tire stiffness (k_k). The data from the 4625 kg case is shown in [Figure 5-12](#).

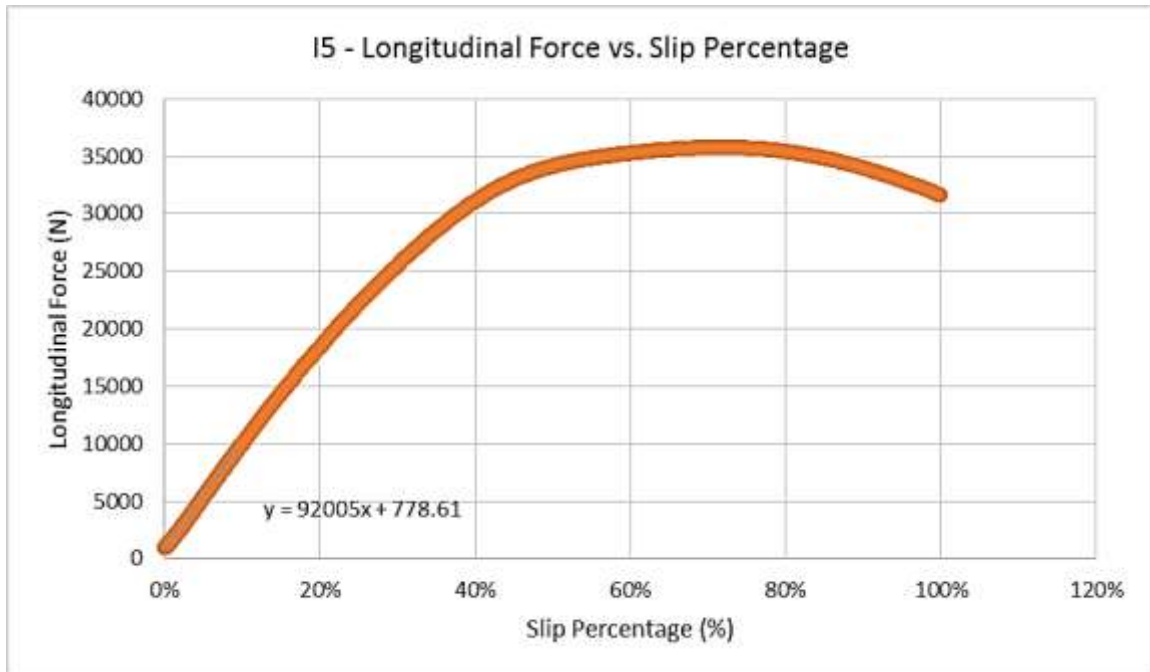


Figure 5-12 Results from the Longitudinal Tire and Tread Stiffness (k_k , k_{cx}) Simulation

By analyzing the data from this virtual experiment, the longitudinal tire stiffness (k_k) can be determined as the slope of the linear portion of the plot. In addition to this, the longitudinal tread stiffness (k_{cx}) can also be determined as the ratio of longitudinal tire stiffness (k_k) to half of the static contact patch length (a), as defined by work conducted by Zegelaar and Pacejka in 1997 [15].

$$k_{cx} = \frac{k_k}{a}$$

5-17

The half contact patch length (a) from

Table 5-3 as well as the data recorded from this virtual experiment were used to calculate the longitudinal tire and tread stiffness (k_k , k_{cx}), shown in Table 5-8.

Table 5-8 Calculated Parameters for the Longitudinal Tire and Tread Stiffness (k_k , k_{cx})

PARAMETER	LOAD [KG]	70 PSI	120 PSI	150 PSI	UNITS
Longitudinal Tire Stiffness (k_k)	2312.5	92.69	90.18	85.18	kN/slip
	4625.0	92.26	92.01	90.26	
	6937.5	94.71	91.45	90.22	
Longitudinal Tread Stiffness (k_{cx})	2312.5	758.90	1135.71	1129.88	kN/m
	4625.0	676.70	925.85	969.79	
	6937.5	513.20	652.16	696.98	

CHAPTER 6: POPULATION OF THE OUT-OF-PLANE RIGID RING MODEL PARAMETERS

This chapter will outline the procedure that was taken to properly calculate the out-of-plane rigid ring parameters. Similar to the previous chapter, specific virtual experiments are designed to isolate for the desired characteristics of the tire model. Again, the specified vertical loads of 2312.5 kg, the rated load of 4625 kg, and 6937.5 kg are used to understand the effect of vertical load on the out-of-plane rigid ring parameters. In addition to the vertical load, the inflation pressure is also varied within the tire model to understand its effect on the parameters.

6.1 DESIRED OUT-OF-PLANE RIGID RING PARAMETERS

In order to populate the out-of-plane rigid ring model, it was deemed necessary to isolate for the following parameters contained in Table 6-1. Through a series of carefully created virtual experiments, the in-plane parameters were calculated in order to populate the analytical rigid ring model.

Table 6-1 Required Out-of-Plane Rigid Ring Parameters

PARAMETER	SYMBOL
Sidewall Translational Stiffness	k_{by}
Sidewall Translational Damping Constant	C_{by}
Sidewall Rotational Stiffness	k_{by}
Sidewall Rotational Damping Constant	C_{by}
Lateral Stiffness	k_l
Lateral Damping Constant	C_l
Cornering Stiffness	k_f
Self-Aligning Torque Stiffness	k_m
Relaxation Length	σ

6.2 TRANSLATIONAL STIFFNESS AND DAMPING CONSTANT OF THE SIDEWALL (k_{by} , C_{by})

The first out-of-plane parameters to be calculated is the translational stiffness and damping constant (k_{by} and C_{by}). These parameters correspond to the tire model's ability to resist deflection and dissipate energy laterally as the forces are applied from the side of the tire, or out-of-plane. In order to isolate these parameters, a simple virtual experiment is conducted in which the tire model has loads applied to the top and bottom of a rigid tread and undertread to induce deflection in the sidewall. The tire is suspended in space for this simulation and does not interact with a road surface in any way. The tire model begins suspended, in which its rigid rim is locked from both translation and rotation. Next, the loads are applied to the top and bottom of the rigid tread and undertread with a magnitude of 2 kN each, chosen arbitrarily. The loads are held constant until a steady state deflection is induced. Its steady state deflection (y_{ss}) is recorded, and then the forces are released. As expected, the tire model will oscillate out-of-plane until it is able to dampen out the energy of the excited system. A visual from this experiment can be seen in [Figure 6-1](#).

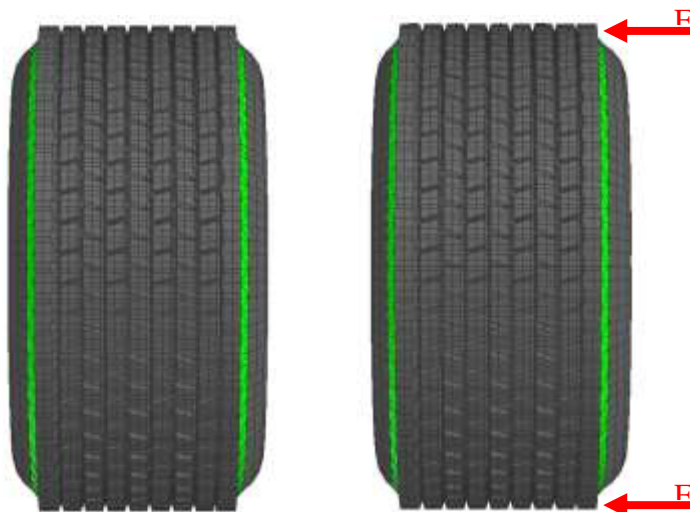


Figure 6-1 Visual for the Translational Stiffness and Damping Constant of the Sidewall (k_{by} , C_{by})

The out-of-plane translational stiffness (k_{by}) can be calculated as the ratio of the total applied force to the measured steady state deflection (y_{ss}), as described in [Equation 6-1](#).

$$k_{by} = \frac{\text{Total Applied Force}}{y_{ss}} \quad 6-1$$

Upon reaching a steady displacement condition, the forces are released in order to induce oscillation and observe the damping properties of the system as the energy is dissipated. The virtual experiment was conducted with the specified inflation pressures, and the recording of the displacement with respect to simulation time can be seen in [Figure 6-2](#).

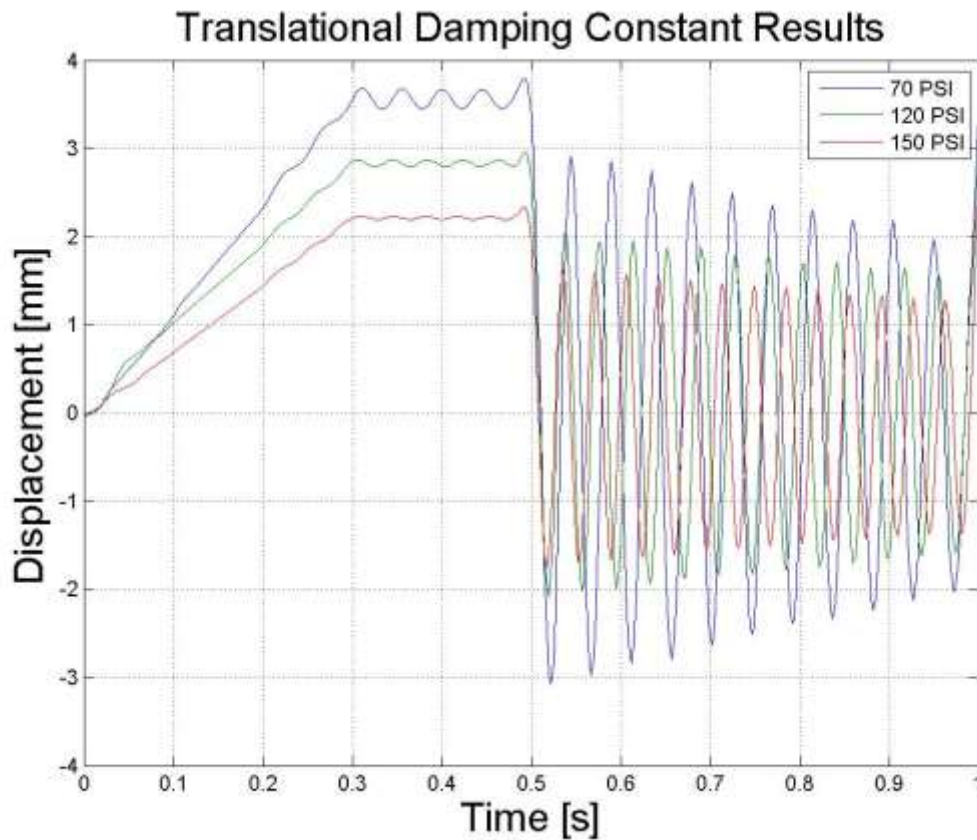


Figure 6-2 Results from the Translational Stiffness and Damping (k_{by} , C_{by}) Simulation

As with previous rigid ring parameters, the data replicates a free-damped vibration system. The energy will decay much like an underdamped mechanical system and the damping constant can be determined by analyzing the difference in oscillation amplitudes as time progresses. The amplitude for the initial rebound (y_1) and its successive amplitude (y_2) are recorded as well as their recorded times (t_1 and t_2 respectively). This initial data is used along with Equations 6-5 to 6-8 to determine the logarithmic decrement (δ), damping ratio (ξ), undamped (ω_n) and damped (ω_d) natural frequencies, and critical damping constant (C_c) to finally solve for the translational damping constant (C_{by}).

$$\delta = \ln\left(\frac{y_1}{y_2}\right) \quad \mathbf{6-2}$$

$$\xi = \frac{\delta}{\sqrt{4\pi^2 - \delta^2}} \quad \mathbf{6-3}$$

$$\tau_d = t_2 - t_1 \quad \mathbf{6-4}$$

$$\omega_n = \frac{2\pi}{\tau_d \sqrt{1 - \xi^2}} \quad \mathbf{6-5}$$

$$\omega_d = \frac{2\pi}{\tau_d} \quad \mathbf{6-6}$$

$$C_c = 2 \times m_b \times \omega_n \quad \mathbf{6-7}$$

Where m_b is the mass of the tire belt, 70.7544 kg

$$C_{by} = \xi \times C_c \quad \mathbf{6-8}$$

Using the procedure outlined above, the translational displacement data for all desired inflation pressures can be processed appropriately. The results can then be used to solve

for the translational stiffness and damping constant of the sidewall (k_{by} , C_{by}), and is shown in Table 6-2.

Table 6-2 Calculated Parameters of the Translational Stiffness and Damping Constant of the Sidewall (k_{by} , C_{by})

PARAMETER	70 PSI	120 PSI	150 PSI	UNITS
Translational Stiffness of the Sidewall (k_{by})	1119.1	1409.7	1803.6	kN/m
Translational Damping Constant of the Sidewall (C_{by})	0.054	0.162	0.198	kN-s/m

6.3 ROTATIONAL STIFFNESS AND DAMPING CONSTANT OF THE SIDEWALL (k_{by} , C_{by})

The next series of out-of-plane parameters to be calculated includes the rotational stiffness and damping constant of the sidewall (k_{by} , C_{by}). These parameters are found in an effort to describe how the tire model will react to out-of-plane rotational deflection rotational excitation. In order to isolate for these parameters, a virtual experiment is conducted which induces rotation in the sidewall while the tire model is suspended freely in space. The tire model's rigid rim is restricted to all forms of translation and rotation, which negates any interaction from a road surface. Two forces of equal magnitude but opposite direction act on nodes which are located on the top and bottom of the tire model's tread. Due to the opposing nature of the applied forces, the tire model will rotate. The forces are then held until steady state rotational displacement occurs. In order to only induce rotation in the sidewall, the tire model tread and undertread are simulated as rigid bodies. The forces used in this simulation were arbitrarily chosen to each be 5 kN and are released after the steady

state displacement (γ_{ss}) occurs. The model will then oscillate back and forth, due to the induced excitement in the system, until the energy is eventually dissipated from the tire model's rotational damping properties. A simulation visual from this virtual experiment can be seen in [Figure 6-3](#), in which an inflation pressure of 120 PSI was used.

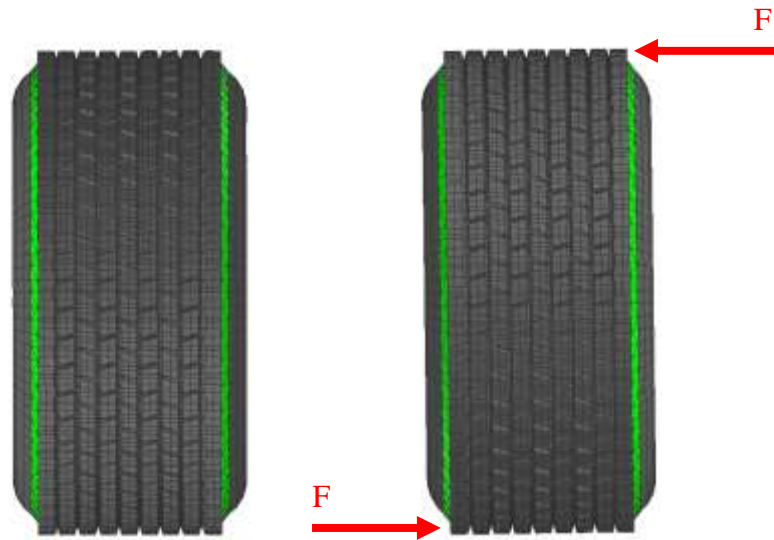


Figure 6-3 Visual of the Rotational Stiffness and Damping Constant of the Sidewall ($k_{b\gamma}$, $C_{b\gamma}$) Simulation

In order to determine the stiffness and damping constants, the angular displacement of the tire tread is recorded from the virtual experiments. The out-of-plane rotational stiffness ($k_{b\gamma}$) can be calculated as the ratio of the total applied moment to the measured steady state deflection (γ_{ss}), as described in [Equation 6-9](#). The displacements with respect to time for all desired inflation pressures can be seen in [Figure 6-4](#).

$$k_{b\gamma} = \frac{\text{Applied Moment At Tire Center}}{\gamma_{ss}} \quad \mathbf{6-9}$$

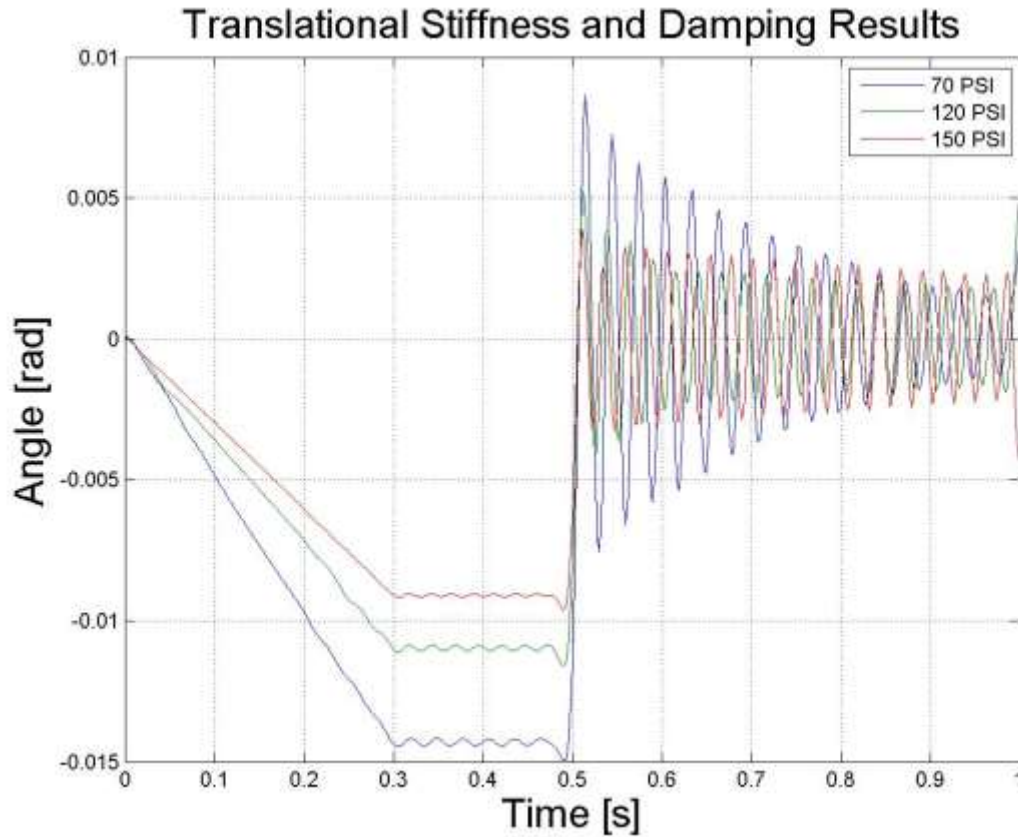


Figure 6-4 Results from the Rotational Stiffness and Damping (k_{by} , C_{by}) Simulation

The simulation results show the initial angular displacement from the steady state load application, and the displacement (y_{ss}) is recorded. When the loads are released, the oscillation of the tire model occurs and each amplitude of oscillation is also recorded. The initial and successive amplitudes (y_1 and y_2) are primarily used along with their recorded times (t_1 and t_2) from these virtual experiments in order to eventually solve for the rotational stiffness and damping constant of the sidewall (k_{by} , C_{by}). These values are used in Equations 6-10 to 6-16 to find the logarithmic decrement (δ), damping ratio (ξ), undamped (ω_n) and damped (ω_d) natural frequencies, and critical damping constant (C_c) to finally solve for the rotational damping constant (C_{by}).

$$\delta = \ln\left(\frac{Y_1}{Y_2}\right) \quad \mathbf{6-10}$$

$$\xi = \frac{\delta}{\sqrt{4\pi^2 - \delta^2}} \quad \mathbf{6-11}$$

$$\tau_d = t_2 - t_1 \quad \mathbf{6-12}$$

$$\omega_n = \frac{2\pi}{\tau_d \sqrt{1 - \xi^2}} \quad \mathbf{6-13}$$

$$\omega_d = \frac{2\pi}{\tau_d} \quad \mathbf{6-14}$$

$$C_c = 2 \times I_{bx} \times \omega_n \quad \mathbf{6-15}$$

Where I_{bx} is the moment of inertia of the tire belt, 10.491kg-m²

$$C_{by} = \xi \times C_c \quad \mathbf{6-16}$$

Using the procedure outlined above, the angular displacement data for the desired inflation pressures can be processed appropriately. The results can then be used to solve for the rotational stiffness and damping constant (k_{by} , C_{by}), which is summarized in [Table 6-3](#).

Table 6-3 Calculated Parameters for the Rotational Stiffness and Damping Constant of the Sidewall (k_{by} , C_{by})

PARAMETER	70 PSI	120 PSI	150 PSI	UNITS
Rotational Stiffness of the Sidewall (k_{by})	353.11	461.22	558.35	kN-m/rad
Rotational Damping Constant of the Sidewall (C_{by})	0.128	0.236	0.419	kN-m-s/rad

6.4 LATERAL TIRE STIFFNESS AND DAMPING CONSTANT (k_l , C_l)

The lateral tire stiffness and damping constant (k_l , C_l) are out-of-plane rigid ring parameters that describe the tire model's reaction to externally applied lateral forces when loaded on a rigid road. The virtual experiment begins with the tire model being rapidly inflated, lowered onto a rigid road and allowing time to settle. As with other rigid ring parameters, the lateral tire stiffness (k_l) is then found by applying a lateral load of 5 kN, chosen arbitrarily, to the tire rigid rim's COG to cause lateral deflection. This force is held constant until the steady state lateral deflection of the tire model is achieved. At this point, the force is released and the tire model will oscillate back and forth until the energy of the system is dissipated, revealing the lateral tire damping constant (C_l). Since the vertical load applied to the tire model is again necessary, the virtual experiments are conducted at vertical loads of 2312.5 kg, the rated load of 4625 kg, and 6937.5 kg. A visual from this virtual experiment can be seen in [Figure 6-5](#), in which a vertical load of 4625 kg and inflation pressure of 120 PSI was used.



Figure 6-5 Visual of the Lateral Tire Stiffness and Damping (k_l , C_l) Simulation

From this simulation, there is only the lateral displacement of the tire with respect to time that is required to be recorded to eventually find the stiffness and damping constants. When the load is held long enough to reach a steady state displacement condition, the final displacement (y_{ss}) of the tire model is recorded. The force will then be released to excite the system, and the amplitudes of the first and successive oscillations (y_1 and y_2), along with the times in which they occur (t_1 and t_2), are also recorded. It is from this simulation data that these required rigid ring parameters will be calculated. A plot of the lateral displacement with respect to time can be seen in [Figure 6-6](#).

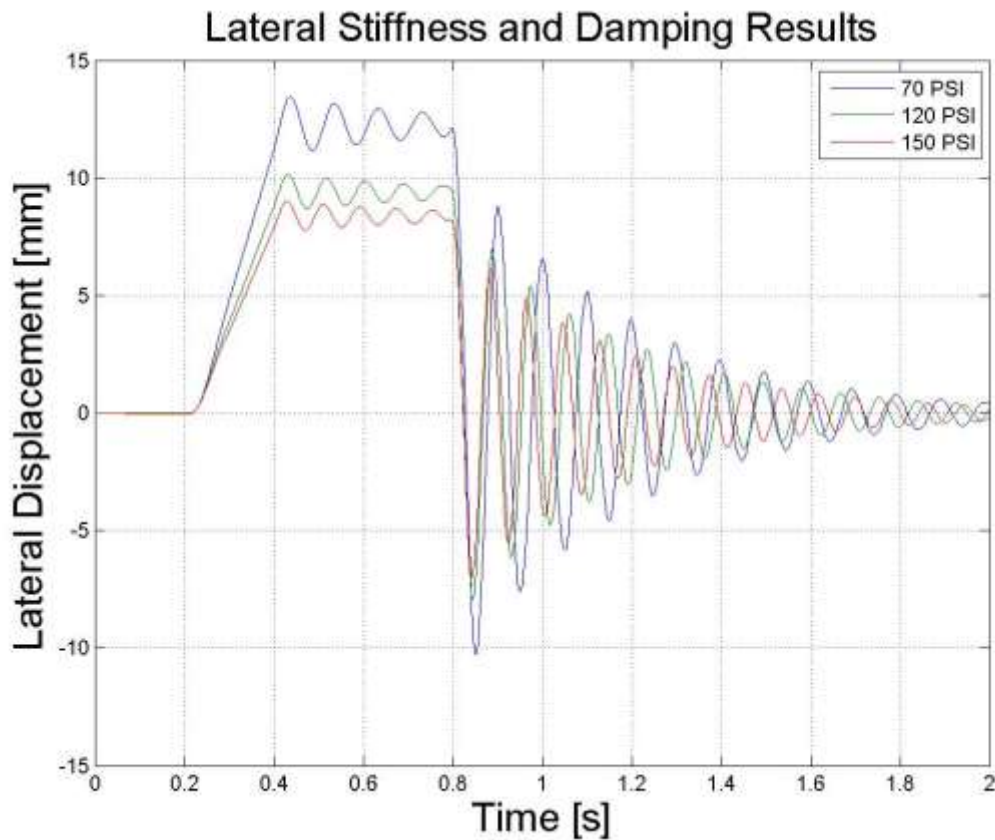


Figure 6-6 Results from the Lateral Tire Stiffness and Damping Constant (k_t , C_t) Simulation

The lateral tire stiffness is then found as the ratio of the applied force at the rim COG to the induced steady state lateral displacement, as outlined in [Equation 6-17](#). In addition, the

behavior of this system allows it be analyzed as a free-damped vibration system. Therefore, the previous damping procedures are used in order to determine the lateral stiffness and damping constant (k_l and C_l).

$$k_l = \frac{\text{Lateral Force}}{y_{ss}} \quad \mathbf{6-17}$$

$$\delta = \ln\left(\frac{y_1}{y_2}\right) \quad \mathbf{6-18}$$

$$\xi = \frac{\delta}{\sqrt{4\pi^2 - \delta^2}} \quad \mathbf{6-19}$$

$$\tau_d = t_2 - t_1 \quad \mathbf{6-20}$$

$$\omega_n = \frac{2\pi}{\tau_d \sqrt{1 - \xi^2}} \quad \mathbf{6-21}$$

$$\omega_d = \frac{2\pi}{\tau_d} \quad \mathbf{6-22}$$

$$C_c = 2 \times m_{\text{wheel}} \times \omega_n \quad \mathbf{6-23}$$

Where m_{wheel} is the mass of tire and rim, 111.253 kg

$$C_l = \xi \times C_c \quad \mathbf{6-24}$$

Using the procedure outlined above, the lateral displacement data for the desired vertical loads and inflation pressures can be processed appropriately. The results can then be used to solve for the lateral tire stiffness and damping constant (k_l and C_l), which is summarized in Table 6-4.

Table 6-4 Calculated Parameters for the Lateral Tire Stiffness and Damping Constant (k_i , C_i)

PARAMETER	LOAD [KG]	70 PSI	120 PSI	150 PSI	UNITS
Lateral Tire Stiffness (k_i)	2312.5	619.28	797.51	887.4	kN/m
	4625.0	608.23	777.63	882.39	
	6937.5	598.15	774.24	863.72	
Lateral Tire Damping Constant (C_i)	2312.5	0.637	0.655	0.657	kN-s/m
	4625.0	0.581	0.592	0.636	
	6937.5	0.568	0.571	0.574	

6.5 CORNERING STIFFNESS (k_f)

The cornering stiffness (k_f) is one of the most useful rigid ring parameters to calculate as it describes how much lateral force can be developed at the contact patch from an induced slip angle (α). The cornering stiffness (k_f) of the tire model can be used for the prediction of steering characteristics and better understand how the tire will behave in either high speed or slip angle maneuvers. In order to calculate the cornering stiffness (k_f) for the tire, multiple controlled steering simulations were necessary. In these simulations, the tire model would be rapidly inflated and lowered onto a rigid road. Upon dissipating the initial energy of the system and settling, the tire model would then be dragged along a rigid road to simulate steady state rolling on a truck tractor pusher axle, which does not drive those wheels. Each simulation would induce a larger set slip angle (α) on the tire in order to understand how the slip angle effects the amount of lateral force that can be developed. In this case, individual simulations were conducted at controlled slip angles of 0, 1, 2, 3, 4, 6, 8, 10, 12, and 20 degrees. Due to the amount of variation that was required, 90 different tire models were created with varying vertical load and inflation pressure and simulated in

order to eventually solve for the necessary parameters. A visual from one such simulation can be seen in [Figure 6-7](#), shown at a vertical load of 4625 kg and an induced slip angle (α) of 10 degrees.

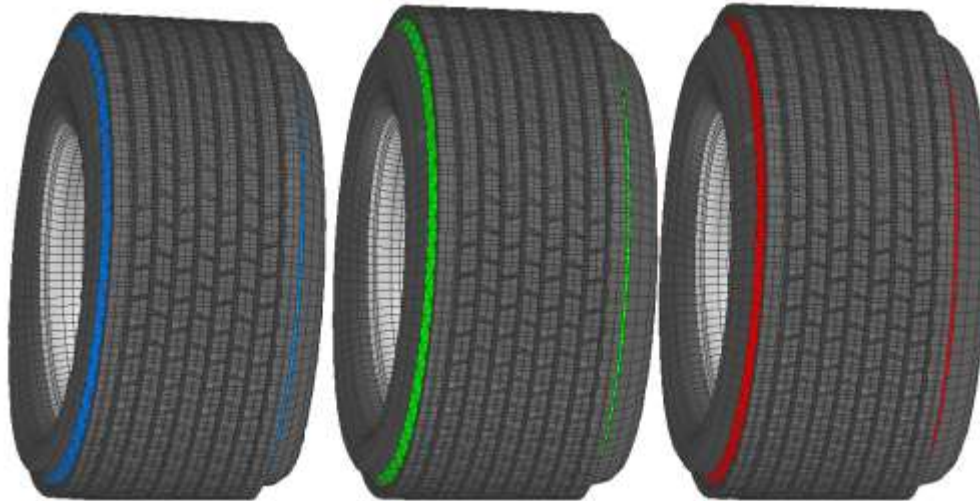


Figure 6-7 Visual of a Cornering Stiffness (k_f) Simulation, Shown at an Induced Slip Angle of 10 Degrees

The cornering stiffness (k_f) can be found as a ratio of the measured lateral force from the simulation to the measured slip angle (α). The lateral force is measured not by the global axis, but by the true lateral force with respect to the tire's axis system. In order to calculate the lateral force, the global longitudinal force (F_x) and the global lateral force (F_y) are recorded during the simulation. Due to the initial excitement of the system, the forces fluctuate during the first moments of the simulation. When steady state forces are observed. The force component is analyzed using [Equation 6-25](#).

$$\text{Lateral Force} = (F_y * \cos \alpha) - (F_x * \sin \alpha) \quad \mathbf{6-25}$$

For each simulation in which a different slip angle was induced, the lateral force was calculated. It is from this data that a plot of the recorded lateral force to the induced slip angle (α) can be made. The cornering stiffness is defined as the slope of this plot during the linear range of lateral force generation, which usually falls between 0-10 degrees of induced slip angle. The plot of the recorded lateral force to slip angle for the rated load case of 4625 kg can be seen in [Figure 6-8](#).

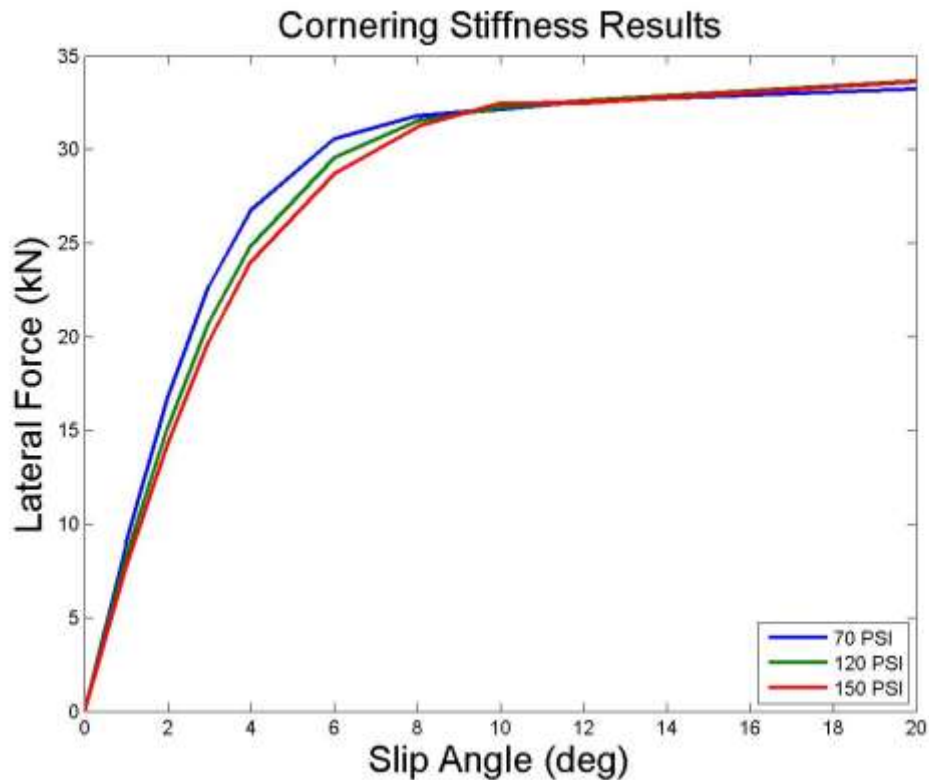


Figure 6-8 Results from the Cornering Stiffness (k_f) Simulation

Using the procedure outlined above, the measured values for F_x and F_y for the desired vertical loads and inflation pressures can be processed appropriately. The results can then be used to solve for the cornering stiffness (k_f), which is summarized in [Table 6-5](#).

Table 6-5 Calculated Parameters for Cornering Stiffness (k_f)

PARAMETER	LOAD [KG]	70 PSI	120 PSI	150 PSI	UNITS
Cornering Stiffness (k_f)	2312.5	256.44	228.46	218.56	kN/rad
	4625.0	435.41	397.12	377.99	
	6937.5	491.89	462.58	441.99	

6.6 RELAXATION LENGTH (σ)

The maximum cornering force that a tire can develop is one of its key characteristics. As described above, however, the steady state cornering force that is generated does not occur instantaneously. There is a delay in the generation of cornering force due to various dynamic resistive forces within the viscoelastic rubber properties. The relaxation length (σ) of a tire defines the length in which the tire must travel in order for the tire to overcome the initial resistive forces and reach its steady state cornering force values. It is found, quite simply, as the ratio of cornering force (k_f) to lateral tire stiffness (k_l). Since both of these parameters have already been calculated, no additional virtual experiments or data analysis is necessary to calculate the relaxation length (σ). Therefore, by using Equation 6-26, Table 6-6 can be populated accordingly.

$$\sigma = \frac{k_f}{k_l} \qquad \mathbf{6-26}$$

Table 6-6 Calculated Parameters for the Relaxation Length (σ)

PARAMETER	LOAD [KG]	70 PSI	120 PSI	150 PSI	UNITS
Relaxation Length (σ)	2312.5	0.414	0.287	0.246	m
	4625.0	0.716	0.511	0.428	
	6937.5	0.822	0.598	0.512	

6.7 SELF-ALIGNING TORQUE STIFFNESS (k_m)

The last out-of-plane rigid ring parameter to calculate is the self-aligning torque stiffness (k_m). As defined by the SAE axis system (described in Chapter 1), this parameter defines the magnitude of the moment that is developed along the z-axis during steady state cornering maneuvers. This moment attempts to realign the tire model with its intended heading while it is experiencing the induced slip angle from the cornering maneuver. Again, the data from the cornering stiffness (k_f) simulations can be recycled for the purpose of determining the self-aligning torque stiffness (k_m). The lateral forces are not used in this case but the measured section moment in the z-axis is the data that is extracted from the cornering simulations. The section moment is pulled from every simulation, and the data is plotted with respect to the slip angle that was induced. A plot of this extracted data can be seen in [Figure 6-9](#).

For the analysis, the self-aligning torque stiffness (k_m) is found as the slope of the self-aligning moment vs. slip angle plot, when the data is within the initial linear range (0-3 degrees). Using this procedure, the self-aligning moment data for the desired vertical loads

and inflation pressures can be processed appropriately. The results can then be used to solve for the self-aligning torque stiffness (k_m), which is summarized in

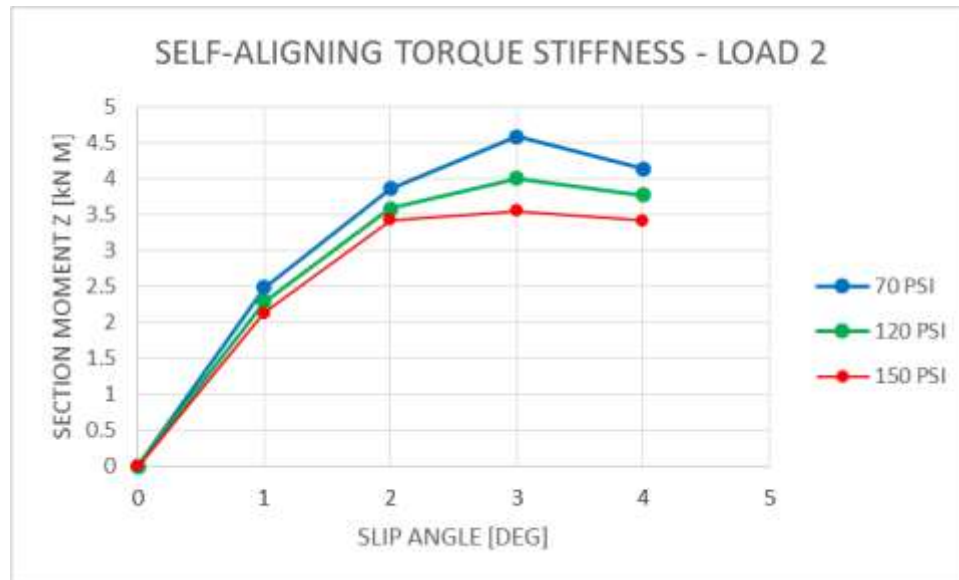


Figure 6-9 Results from the Self-Aligning Torque Stiffness (k_m) Calculations

Table 6-7.

Table 6-7 Calculated Parameters for the Self-Aligning Torque Stiffness (k_m)

PARAMETER	LOAD [KG]	70 PSI	120 PSI	150 PSI	UNITS
Self-Aligning Torque Stiffness (k_m)	2312.5	1.269397	0.948873	0.74511	kN-m/rad
	4625.0	2.1156	1.958083	1.852527	
	6937.5	2.61269	2.413287	2.145327	

CHAPTER 7: CONCLUSIONS AND FUTURE WORK

7.1 GENERAL CONCLUSIONS

An educated approach was taken to the modelling, validation, and use of an FEA tire model based on a Michelin XONE XDA 445/50R22.5. Experimental measurements were taken at the Volvo Group North America Greensboro Campus in Greensboro, North Carolina in which the Greensboro Proving Grounds were used to capture rolling resistance data for various dynamic scenarios. Wheel force transducers were implemented on wide base tires located on a pusher axle and recorded all forces and moments that the wide base tire encountered. The experimental data, along with acquired physical parameters, were then used to construct a wide base FEA tire model using new and innovative techniques. Material properties were unavailable for the modelling process, and thus a new technique was used in order to calculate the appropriate material properties to mimic the behaviour of the physical tire under various conditions. Parameter-tuning optimization was implemented to iteratively solve for the appropriate combination of material properties to match the behaviour during static and dynamic simulations. An analysis of the available optimization algorithms built into PAM-OPT was conducted on a simple pressure-sinkage FEA soil model in order to choose a suitable parameter-tuning algorithm. The optimization process was scaled up to incorporate many simulations which would replicate the scenarios the physical tire endured in order to match the behaviour of the tire. Through the use of an Adaptive Response Surface Method (ARSM) optimization algorithm, the newly constructed wide base FEA truck tire model underwent a parameter-tuning procedure of its materials until the behaviour of the virtual model closely matched the behaviour of the

physical tire. The optimized tire model achieved a minimum of 1.78% error in the amount of rolling resistance force measured during steady-state driving conditions between the physical and simulated experiments. In addition, the static vertical deflection of the virtual tire model was able to be minimized to only 0.42% error in comparison to the physical tire. The FEA tire model was then used in multiple simulations in order to populate an analytical in-plane and out-of-plane rigid ring model. These simulations were specifically designed to isolate for various parameters of the tire model which enable the characterization of this FEA tire model and can now be compared to similar models for design consideration. In addition to the characterization, the analytical rigid ring model can also be used for the quick prediction of tire-ground interactions prior to the implementation of the more complex FEA tire model during various tire research and design projects.

From the rigid ring model results, various trends can be observed. It can be shown, in general, that an increase in the inflation pressure within the FEA tire model resulted in an increase in various stiffness parameters including the total static vertical stiffness (k_{sv}), total dynamic vertical stiffness (k_{dv}), translational stiffness (k_{by}), and lateral tire stiffness (k_l).

In addition, it is found that most translational damping constants recorded a decrease in the damping constant with respect to increasing inflation pressure. In contrast, the rotational damping constants recorded an increase in the damping constant with respect to increasing inflation pressure. In general, the translational damping constants showed difficulty in producing ideal trends with respect to increasing inflation pressure and vertical load. There was also noticeable difference in predicted to calculated trends for some rotational parameters of the tire model, and thus further investigation into some of these discrepancies should be conducted.

Overall, the process yielded useful and meaningful data that has the ability to be implemented on similar projects in the future. This step-by-step approach to the construction, validation, and simulation of a wide base FEA tire model was described in a way to allow for this procedure to be used in upcoming tire-ground interaction research projects.

7.2 CONSIDERATIONS FOR FUTURE WORK

The procedure that has been outlined for the construction, validation and simulation of a FEA wide base tire model incorporated many engineering disciplines. Portions of automotive engineering, computer science, civil engineering, and mechanical engineering have all been implemented over the course of this research project. It is from this complexity of the project that there remains areas for improvement in different tasks.

For the experimental data gathered at the Greensboro Proving Grounds, the rolling resistance data that was recorded from the multiple wheel force transducers were mounted on similar, but not exactly the same pneumatic tires that were to be modelled. Although they are from the same manufacturer and are of the same product line, there are differences in the tread design. It is from these slight differences that make rise to a fundamental inaccuracy in the data that was implanted in the parameter-tuning optimization algorithm. Although the difference may be negligible, an area of improvement would be to capture the experimental data for these scenarios from the exact tire that is to be modelled.

Black box optimization was at the core of the parameter-tuning process used for the validation of this tire model. Where black box systems behave differently than traditional optimization problems is that there may not be a deterministic solution landscape available.

In these systems, where there is a highly complex and non-linear relationship between the many design parameters and the objectives, it becomes difficult to determine if a true global minimum in error has been reached. Due to time considerations, the full-scale combined parameter-tuning optimization algorithm was only able to complete 45 iterations before it ended. With the equipment available in the Vehicle Dynamics and Crash Simulation Laboratory, the average static simulation would require six hours to solve. The dynamic rolling resistance simulations required at least twice that amount, averaging at 13 hours each. In the optimization process, two static and two dynamic simulations were completed in each iteration of the algorithm for a total of 38 hours/iteration. Therefore, the 45 iterations it was able to complete took approximately 72 days. For systems which are of a high level of complexity, it would be recommended to increase the number of completed iterations in order to exhaust the specified search space and avoid premature convergence. Thus, for future work considerations, the algorithm should be allowed to run definitively before accepting the results and validating the FEA tire model.

In order to populate the in-plane and out-of-plane rigid ring model, a high number of individual simulations were needed to be conducted to examine the difference in inflation pressure and vertical load on the results. It can be noted that some of the results and trends were more ideal than others, specifically regarding certain damping properties within the tire sidewall. For future considerations, the modelling complexity in the sidewall may need to be increased from the multilayer 2D membranes to a combined 3D element and multilayer membrane sidewall. It is from this combination of modelling techniques that a 3D solid structure of the sidewall could be externally wrapped in the 2D membranes to better replicate the interaction between the sidewall rubber matrix and the tire carcass steel

plies. This difference in modelling procedure is believed to be a potential culprit for the less than ideal trends observed in some of the damping trends with respect to increasing inflation pressure or vertical load.

REFERENCES

- [1] J. L. Slade, "Development of a New Off-Road Rigid Ring Model For Truck Tires Using Finite Element Analysis Techniques," The Pennsylvania State University, State College, 2009.
- [2] A. J. C. Schmeitz, *A Semi-Empirical Three-Dimensional Model of the Pneumatic Tyre Rolling Over Arbitrarily Uneven Road Surfaces*, Delft University of Technology, 2004.
- [3] A. Reid, M. El-Gindy, F. Oijer, I. Johansson and D. Philipps, "Prediction of Tire Ground Interaction Using FEA Truck Tire Models," *4th Annual Tyre Colloquium*, April 2015.
- [4] North American Council for Freight Efficiency, "Executive Report - Wide Base Tires," North American Council for Freight Efficiency, 2010.
- [5] J. Y. Wong, *Theory of Gound Vehicles*, New Jersey: John Wiley & Sons, 2008.
- [6] R. S. Dhillon, "Development of a Truck Tire-Terrian Finite Element Analysis Model," University of Ontario Institute of Technology, Oshawa, 2013.
- [7] H. Heisler, *Advanced Vehicle Technology*, Oxford: Butterworth-Heinemann Ltd, 2002.

- [8] "Top 10 Reasons to Convert to an X ONE," Michelin North America Inc., 2014. [Online]. Available: http://www.michelintruck.com/en_CA/tires-and-retreads/x-one-tires/top-10-reasons-to-convert/. [Accessed 1 March 2015].
- [9] D. Marsh, "Michelin: Wide Base X ONE Tire," *Concrete Products*, vol. 117, no. 5, p. 29, May 2014.
- [10] S. Chae, "Nonlinear Finite Element Modeling and Analysis of a Truck Tire," The Pennsylvania State University, 2006.
- [11] Michelin, *The Tyre, Grip*, Clermont-Ferrand: Ed. Société de Technologie Michelin, 2001.
- [12] K. M. Captain, A. B. Boghani and D. N. Wormley, "Analytical Tire Models for Vehicle Dynamic Simulation," *Vehicle System Dynamics: International Journal of Vehicle Mechanics and Mobility*, vol. 8, pp. 1-32, 1979.
- [13] M. Loo, "A Model Analysis of Tire Behaviour Under Vertical Loading and Straight-Line Free Rolling," *Tire Science and Technology*, vol. 13, pp. 67-90, 1985.
- [14] Y. Chang, M. El-Gindy and A. Streit, "Literature Survey of Transient Dynamic Response Tyre Models," *International Journal of Vehicle Design*, vol. 10, pp. 354-386, 2004.
- [15] P. W. A. Zegelaar and H. B. Pacejka, "Dynamic Tyre Responses to Brake Torque Variations," *Vehicle System Dynamics: International Journal of Vehicle Mechanics and Mobility*, vol. 27, pp. 65-79, 1997.

- [16] T. B. Rhyne, R. Gall and L. Y. Chang, "Influence of Rim Run-Out on the Nonuniformity of Tire-Wheel Assemblies," *Tire Science and Technology*, vol. 22, no. 2, pp. 99-120, 1994.
- [17] B. G. Kao and M. Muthukrishnan, "Tire Transient Analysis With an Explicit Finite Element Program," *Tire Science and Technology*, vol. 25, no. 4, pp. 230-244, 1997.
- [18] D. Whitley, "A Genetic Algorithm Tutorial," *Statistics and Computing*, vol. 4, pp. 65-85, 1994.
- [19] E.-G. Talbi, *Metaheuristics: From Design to Implementation*, Hoboken, New Jersey: John Wiley & Sons, Inc, 2009.
- [20] G. Wang, Z. Dong and P. Aitchison, "Adaptive Response Surface Method - A Global Optimization Scheme for Approximation-based Design Problems," *Engineering Optimization*, vol. 33, no. 6, pp. 707-734, 2001.
- [21] Michigan Scientific Corporation, "Michigan Scientific Corporation Wheel Load Measurement System," Michigan Scientific Corporation, Milford, MI, 2013.
- [22] M. Bekker, "Theory of Land Locomotion," *The University of Michigan Press*, 1956.
- [23] R. N. Yong, E. A. Fattah and P. Brunsinsuk, "Analysis and Prediction of Tyre-Soil Interaction Performance Using Finite Elements," *Journal of Terramechanics*, vol. 15, no. 1, pp. 43-63, 1978.

- [24] A. Reid, M. El-Gindy, D. Philipps, F. Oijer and I. Johansson, "Development of a Modified Off-Road Rigid Ring Tire Model for Heavy Trucks," *SAE*, p. 12, 2013.
- [25] A. Reid, M. El-Gindy, D. Philipps, F. Oijer and I. Johansson, "Development of a Modified Off-Road Rigid Ring Model for Heavy Trucks," *SAE World Congress & Exhibition*, no. 2014-01-0878, 2014.
- [26] S. S. Rao, *Mechanical Vibrations Fith Edition*, New Jersey: Pearson Eduction, Inc., 2011.
- [27] S. Chae, M. El-Gindy, M. Trivedi, I. Johansson and F. Öijer, "In-Plane and Out-of-Plane Dynamic Response Predictions of a Truck Tire," *ASME International Mechanical Engineering Congress and Exposition*, pp. 1-16, 2005.
- [28] S. Chae, M. El-Gindy, J. Allen, M. Trivedi, I. Johansson and F. Öijer, "Dynamic Response Predictions of Quarter-Vehicle Models using a FEA and Rigid Ring Truck Tire Models," *ASME International Mechanical Engineering Congress and Exposition*, pp. 99-107, 2006.
- [29] W. Brixius, "Traction Prediction Equations for Bias Ply Tires," *ASAE Paper No. 87-1662*, 1987.
- [30] R. Ali, R. Dhillon, M. El-Gindy, F. Öijer, I. Johansson and M. Trivedi, "Soil Modelling Using FEA and SPH Techniques for a Tire-Soil Interaction," *ASME*, p. 10, 2011.

- [31] R. Ali, R. Dhillon, M. El-Gindy, F. Öijer, I. Johansson and M. Trivedi, "Prediction of Tire Ground Interaction Using FEA Truck Tire Models," *ASME*, p. 9, 2012.
- [32] R. Ali, R. Dhillon, M. El-Gindy, F. Öijer, I. Johanson and T. Mukesh, "Development of Truck Tire-Soil Interaction Model using FEA and SPH," *SAE*, p. 8, 2012.
- [33] Tekscan, 2006.
- [34] ESI Group, *Explicit Solver Notes Manual*, Paris, France: ESI Group, 2012.
- [35] Bridgestone, "Basic Structure - Radial Tires," 1 March 2015. [Online]. Available: http://www.bridgestone.com/products/speciality_tires/aircraft/products/basicstructure/radial.html.
- [36] J. Allen, M. El-Gindy, S. Chae, F. Öijer, M. Trivedi and I. Johansson, *Dynamic Response Predictions of Quarter-Vehicle Models Using FEA and Rigid Ring Truck Tire Models [PowerPoint Slides]*, Presented at the 2006 ASME International Mechanical Engineering Congress and Exposition, 2006.